

Coordination of protein synthesis and degradation in mammalian cells

Présentée le 21 février 2023

Faculté des sciences de la vie
Unité du Prof. Suter
Programme doctoral en approches moléculaires du vivant

pour l'obtention du grade de Docteur ès Sciences

par

Shoujie SUN

Acceptée sur proposition du jury

Prof. V. Simanis, président du jury
Prof. D. M. Suter, directeur de thèse
Prof. S. Pelet, rapporteur
Prof. G. Neurohr, rapporteur
Prof. A. Oates, rapporteur

Acknowledgements

I owe gratitude to many people for the completion of this thesis and the years passing in between, for these years have been years of wonders, as the way that life and myself were transformed could only be described as enigmatic.

First of all, my gratitude to David Suter is beyond the bounds of any formality, as his support and understanding during both regular and difficult times are invaluable. The discovery I made during my PhD is owing to his positivity and encouragement. I could not thank my friend and colleague Benjamin Martin enough, as his knowledge, effort, and companionship are inseparable from this thesis. I was very fortunate to receive companionship from another friend and colleague, Elias Friman. I regretted that our time together had not been longer. So too with Cédric Deluz. I thank Silja Placzek for the years we spent together and Joanna Dembska for her friendship. I greatly appreciate the time I spend with my colleagues Almut Eisele, Armelle Tollenaere, Ludovica Vanzan, Romane Mizeret, Sim Sakong, and Stella Krämer. I feel sorry to have to rank members of Suter lab in a particular order in my acknowledgements; in fact, it is not my intention, as I owe gratitude to each person. Many people give me their generous help. Olivier Burri and Romain Guiet have given their unreserved service to segment and track my cells; so too did Éric Paquet for the initial modelling; Fabien Kuttler for his time spent on holographic imaging.

The understanding from my parents has always been important to me. The last time I went back to China was 5 years ago, and it has been 3 years since we met in person. I would not say it is easy what they endured. I have been lucky to be offered friendships with such kind people. Joe Weber, I miss our time together. Clemence, there are still many things I want to share with you. Pengcheng Yao, and Peter Qin, I know you will not forget me.

The time has come to thank Claudia Lozano. You are the wonder of my life. All I need to do is to follow you, and our wonders will continue...

Contributions

This thesis contains works from Benjamin Martin (EPFL, UPSUTER), who performed all the calculations for the superstatistical Bayesian inference, passive adaption model, and the mOrange2 maturation rate. He wrote the text of chapters 4.10 and 4.18. He generated Fig. 2c, e, f, g, Fig. 6, Fig. 7e, f, Fig. 8d, e, f, g, h, Fig. 12a, b, c, d, e, f, Fig. S1, Fig. S2f, Fig. S5, Fig. S6e, Fig. S7a, b, Fig. S12, which were modified and included here as they are indispensable for the interpretation and the conclusion of the thesis.

Abstract

The cellular protein levels are determined by protein synthesis and turnover rates. Two processes are involved in the proteome's turnover in proliferating cells: protein degradation and dilution. In theory, maintaining the cellular proteome concentration, which is imperative to proper cellular function, requires the coordination between protein synthesis and turnover. Although the relationship between protein synthesis, degradation, and dilution has been studied in bacteria and yeasts, little is known about how mammalian cells can balance these rates to uphold proteostasis. The peculiarity of the mammalian cells is that the dilution rate, the main counterpart to protein synthesis in bacteria or yeasts, can be highly restrictive in many cases, giving greater necessity to the coordination between synthesis and degradation. Despite evidence to support the existence of such coordination, there is little information about the mechanism behind such cooperation. Previous studies that attempted to disentangle the relationship between protein synthesis and degradation relied on using high concentrations of inhibitors that irreversibly disrupt the equilibrium proteostasis.

The thesis addressed these questions by creating reversible static or dynamic proteostasis states where the protein synthesis rate was manipulated. Meanwhile, the dynamics in protein synthesis, degradation and dilution were quantified with high temporal resolution. The tool that enables the measurements is the tandem fluorescent timer (tFT, or Timer) reporter, engineered to measure both ubiquitin-dependent and ubiquitin-independent degradation rates by the proteasome. Complementary to the tFT measurements was a superstatistical Bayesian inference algorithm employed to calculate timer evolving the synthesis and degradation rates from the live cell time-lapse microscopy.

We discovered that the change in protein synthesis was counterbalanced by the change in both protein degradation and dilution, which buffered the protein concentration but could not completely compensate. Such counteracting of degradation towards synthesis was also observed in non-dividing cells. The recapitulation of protein degradation adaption dynamics revealed a delay in the action of degradation machinery in a time range of several hours. We discussed the effect of change in degradation and dilution on proteome stoichiometry. The transcriptome and *in vitro* assays further concluded that neither the differential expression nor proteasome content could fully explain the change in the degradation adaption. Finally, we proposed a passive adaption model to explain the degradation adaption to synthesis, which matched the observation from our Timer reporter.

Keywords

Proteostasis, protein synthesis, protein degradation, protein dilution, protein turnover, cell proliferation, mouse embryonic fibroblasts, proteasome, tandem fluorescent timer, SNAP tag, cycloheximide, passive adaption, superstatistical modelling, Bayesian inference.

Résumé

In cellulo, les niveaux de protéines sont déterminés par les taux de synthèse et de décroissance (decay) des protéines. Dans les cellules en prolifération, deux processus sont impliqués dans la décroissance des niveaux protéiques: la dégradation et la dilution des protéines. En théorie, le maintien de la concentration du protéome cellulaire, qui est impératif pour le bon fonctionnement cellulaire, nécessite la coordination entre la synthèse et la décroissance des protéines. Bien que la relation entre synthèse, dégradation et dilution des protéines ait été étudiée chez les bactéries et les levures, peu de choses sur la façon dont les cellules de mammifères corégulent ces taux, dans un souci de maintien de la protéostasie, sont aujourd'hui connues. La particularité des cellules de mammifères réside en ce que la modulation du taux de dilution, le principal facteur contrebalançant la synthèse des protéines chez les bactéries ou les levures, peut se présenter, en elle seule, comme limitante dans de nombreux cas, rendant nécessaire la coordination entre la synthèse et la dégradation per se. Malgré les preuves de l'existence d'une telle coordination, il existe peu d'informations sur les mécanismes sous-tendant cette coopération. Les précédentes études, ayant tenté de démêler la relation entre synthèse et dégradation des protéines, reposaient sur l'utilisation de concentrations élevées d'inhibiteurs perturbant de manière irréversible la protéostasie.

Cette thèse aborde ces questions en créant des états de protéostasie statique ou dynamique réversibles où le taux de synthèse des protéines a été manipulé. Les dynamiques de synthèse, dégradation et dilution des protéines ont été quantifiées avec une haute résolution temporelle. L'outil qui permet ces mesures est le rapporteur de protéines fluorescentes en tandem (tFT ou Timer), conçu pour mesurer les taux de dégradation par le protéasome, qu'ils soient dépendants ou indépendants de l'ubiquitine. En complément des mesures du tFT, un algorithme d'inférence bayésienne superstatistique a été utilisé pour calculer l'évolution des taux de synthèse et de dégradation du Timer à partir de mesures effectuées par microscopie time-lapse des cellules vivantes.

Nous mettons en évidence que l'altération de la synthèse des protéines était contrebalancée par la modification de la dégradation des protéines et de leur dilution, qui tamponne les variations de concentration des protéines mais ne peut les compenser complètement. Ce contrepois de la dégradation envers la synthèse a également été observé dans des cellules ne se divisant plus. La récapitulation de la dynamique d'adaptation de la dégradation des protéines a révélé un délai, de l'ordre de plusieurs heures, dans l'action de la machinerie de dégradation. Nous avons discuté de l'effet de la modification de la dégradation et de la dilution sur la stœchiométrie du protéome. Un séquençage d'ARN ainsi que des expériences in vitro ont permis de conclure que ni l'expression différentielle ni le contenu cellulaire en protéasome ne pouvaient expliquer entièrement l'adaptation observée de la

dégradation. Enfin, nous avons proposé un modèle d'adaptation passive pour expliquer l'adaptation de la dégradation à la synthèse.

Mots clés

Protéostasie, synthèse des protéines, dégradation des protéines, dilution des protéines, renouvellement des protéines, prolifération cellulaire, fibroblastes embryonnaires de souris, protéasome, horloge moléculaire de protéines fluorescentes en tandem, SNAP-tag, cycloheximide, adaptation passive, biologie des systèmes, modélisation, inférence bayésienne.

Table of Contents

1. BACKGROUND	10
1.1. PROTEINS ARE ACTIVELY TURNED OVER IN MAMMALIAN CELLS	10
1.2. THE COORDINATION BETWEEN PROTEIN SYNTHESIS AND DEGRADATION	12
1.2.1. <i>Protein synthesis and growth</i>	12
1.2.2. <i>Protein degradation</i>	13
1.2.3. <i>Dilution and proteostasis</i>	16
1.2.4. <i>Coordination of synthesis and degradation</i>	17
1.2.5. <i>How do cells deal with imbalances in protein synthesis and degradation?</i>	19
1.3. METHODS TO QUANTIFY PROTEOSTASIS	21
1.4. THE OBJECTIVE OF THE THESIS	23
2. RESULTS	25
2.1. TIMER AS A METHOD TO MONITOR GLOBAL PROTEOSTASIS DYNAMICS	25
2.2. VALIDATE A SUPERSTATISTICAL BAYESIAN INFERENCE ALGORITHM TO INFER PROTEIN SYNTHESIS AND TURNOVER RATES FROM TIMER TRACES	29
2.3. DOWNREGULATION OF PROTEIN DEGRADATION FOLLOWING THE TREATMENT OF TRANSLATION ELONGATION INHIBITOR CYCLOHEXIMIDE	30
2.4. DOWNREGULATION OF PROTEIN DEGRADATION FOLLOWING THE TREATMENT OF AN INHIBITOR OF TRANSCRIPTION FACTOR MYC	33
2.5. THE SAME FOLD CHANGES IN DEGRADATION AND DILUTION RATES TO PRESERVE THE RELATIVE PROTEOME COMPOSITION DURING THE CHX TREATMENTS	36
2.6. PROTEIN TURNOVER DYNAMICALLY ADAPTS TO THE CHANGE OF PROTEIN SYNTHESIS FOLLOWING CHX ADDITION AND CHX RELEASE	37
2.7. DYNAMICS OF SYNTHESIS, DEGRADATION, AND DILUTION RATES DURING CHX ADDITION OR RELEASE	40
2.8. VALIDATION OF MODELLED DEGRADATION RATE BY SNAP PULSE-CHASE LABELLING	42
2.9. PROTEIN DEGRADATION ADAPTION TO PROTEIN SYNTHESIS IN NON-DIVIDING CELLS	44
2.10. PROTEIN DEGRADATION DYNAMICALLY ADAPTS TO THE CHANGE OF PROTEIN SYNTHESIS FOLLOWING MYC1 ADDITION AND MYC1 RELEASE	45
2.11. TRANSCRIPTION REGULATION DURING CHX RELEASE	47
2.12. PROTEASOME CONTENT AND PEPTIDASE ACTIVITY DURING CHX RELEASE	51
2.13. STEADY-STATE PROTEIN LEVELS COULD BE PREDICTED USING A PASSIVE ADAPTION MODEL	53
3. DISCUSSION	57
3.1. GLOBAL PROTEIN DEGRADATION RATE IS COORDINATED WITH PROTEIN SYNTHESIS	57
3.2. MEASURE DYNAMICS OF PROTEIN SYNTHESIS AND TURNOVER RATES	60
4. MATERIAL AND METHOD	61
4.1. CELL CULTURE	61
4.2. LIVE-IMAGING OF TIMER AFTER PROLONGED TREATMENTS WITH INHIBITORS	61
4.3. USE THE SNAP TAG TO MEASURE THE DEGRADATION RATE	61
4.4. MEASURE PROTEIN SYNTHESIS RATES BY L-HOMOPROPARGYLGLYCINE LABELLING	62
4.5. MEASURE PROTEIN SYNTHESIS RATES BY O-PROPARGYL-PUROMYCIN LABELLING	62
4.6. MEASURE TOTAL NUCLEAR PROTEIN CONCENTRATION BY N-HYDROXYSUCCINIMIDE	63
4.7. IMAGE PRE-PROCESSING	64
4.8. CELL SEGMENTATION AND TRACKING	64
4.9. CALCULATE S , K , AND K_{DEG} FROM SNAP PULSE-CHASE LABELLING	64
4.10. CALCULATE K_{DIL} FROM TIME-LAPSE MOVIES	65
4.11. ESTIMATE THE MORANGE2 MATURATION RATE	66
4.12. RNA EXTRACTION, LIBRARY PREPARATION AND SEQUENCING	66
4.13. RNA-SEQ DATA PROCESSING	67
4.14. TRANSCRIPTOME ANALYSIS	67
4.15. NATIVE PROTEIN EXTRACTION	67
4.16. PROTEASOME NATIVE GEL AND WESTERN BLOT	68
4.17. <i>IN VITRO</i> PROTEASOMAL CHYMOTRYPSIN PEPTIDASE ACTIVITY ASSAY	68
4.18. MODELLING AND INFERENCE OF TIMER	69
4.18.1. <i>Inference algorithm — Timer trajectories</i>	69
4.18.2. <i>Inference algorithm — SNAP and cell number trajectories</i>	70

4.18.3. Passive adaption model.....	71
4.18.4. Modelling of "no adaption", "perfect adaption", "volume-mediated adaption" and " K_{dil} -mediated adaption" models.....	75
4.18.4.1. "No adaption" model.....	75
4.18.4.2. "Perfect adaption" model.....	75
4.18.4.3. "Volume-mediated adaption" model.....	76
4.18.4.4. " K_{dil} -mediated adaption" model.....	76
4.18.4.5. Change in proteome content in the passive adaption model: absolute abundance, relative abundance, and concentration.....	77
5. SUPPLEMENTARY TABLES.....	79
6. SUPPLEMENTARY FIGURES.....	84
7. REFERENCE.....	97
8. CURRICULUM VITAE.....	109

Figures

FIGURE 1 THE PROTEOME DYNAMIC IS A FUNCTION OF PROTEIN SYNTHESIS DEGRADATION AND DILUTION.	11
FIGURE 2 TIMER AS A TOOL TO MEASURE DYNAMICS OF SYNTHESIS AND DEGRADATION.	27
FIGURE 3 PROTEIN DEGRADATION ADAPTION TO PROLONGED CHX TREATMENTS.	32
FIGURE 4 PROTEIN DEGRADATION ADAPTION TO PROLONGED MYC1 TREATMENT.	34
FIGURE 5 DYNAMICS OF SYNTHESIS AND DEGRADATION DURING CHX AND CHX RELEASE TREATMENT. ...	38
FIGURE 6 CALCULATION OF PROTEIN SYNTHESIS AND DEGRADATION DYNAMICS FOR CHX CONDITIONS. ..	41
FIGURE 7 VALIDATION OF DEGRADATION DYNAMICS DURING CHX RELEASE.	42
FIGURE 8 DYNAMICS OF SYNTHESIS AND DEGRADATION DURING MYC1 AND MYC1 RELEASE TREATMENT.	46
FIGURE 9 TRANSCRIPTIONAL REGULATION OF PROTEOSTASIS DURING THE CHX RELEASE.	48
FIGURE 10 DYNAMICS OF PATHWAYS DURING THE CHX RELEASE.	49
FIGURE 11 MEASURE THE PROTEASOME CONCENTRATION, AMOUNT PER CELL, AND ACTIVITY <i>IN VITRO</i>. ...	52
FIGURE 12 THE CHANGE OF THE STEADY-STATE DEGRADATION RATE COULD BE EXPLAINED BY THE "PASSIVE ADAPTION" MODEL.	55

Supplementary Figures

FIGURE S1 CALCULATION OF TIMER CONSTANTS AND VALIDATION OF TIMER MODELLING.	84
FIGURE S2 VALIDATION OF CALCULATIONS FOR PROTEIN DEGRADATION ADAPTION TO CHX AND MYC1 TREATMENT.	85
FIGURE S3 CORRELATIONS BETWEEN ALL THE CALCULATIONS FROM CHX AND MYC1 STEADY-STATES. ..	87
FIGURE S4 PRE-PROCESSING OF TIMER TRACES FOR MODELLING.	88
FIGURE S5 RETRODICTION OF TIMER TRACES FROM MODELLED S AND K FOR CHX ADDITION AND RELEASE.	89
FIGURE S6 VALIDATION OF DEGRADATION DYNAMICS DURING CHX RELEASE.	89
FIGURE S7 DYNAMICS OF SYNTHESIS AND DEGRADATION DURING MYC1 AND MYC1 RELEASE TREATMENT.	90
FIGURE S8 CLUSTERING GENES BASED ON THEIR DYNAMICS DURING CHX RELEASE.	92
FIGURE S9 DYNAMICS OF CELLULAR PATHWAYS DURING CHX RELEASE.	93
FIGURE S10 TRANSCRIPTION DYNAMICS FOR SELECTED PATHWAYS DURING CHX RELEASE.	94
FIGURE S11 OVER-REPRESENTATION ESSAY FOR CLUSTERED GENES.	95
FIGURE S12 THE CALCULATION OF THE PROTEOSTASIS RELATIONS IN THE PASSIVE ADAPTION MODEL. ...	96

Tables

TABLE 1. MEASUREMENTS FROM STEADY STATES INDUCED BY 48 h CHX TREATMENT	79
TABLE 2. MEASUREMENTS FROM STEADY STATES INDUCED BY 48 h MYC1 TREATMENT	81
TABLE 3. SNAP MEASUREMENTS FROM THE SHORT-LIVED TIMER	83
TABLE 4. SNAP MEASUREMENTS FROM THE LONG-LIVED TIMER	83

Equations

Eq. 1	17
Eq. 2	25
Eq. 3	25
Eq. 4	26
Eq. 5	31
Eq. 6	36
Eq. 7	39
Eq. 8	53
Eq. 9	53
Eq. 10.....	53
Eq. 11.....	64
Eq. 12.....	65
Eq. 13.....	65
Eq. 14.....	65
Eq. 15.....	66
Eq. 16.....	69
Eq. 17.....	70
Eq. 18.....	70
Eq. 19.....	71
Eq. 20.....	71
Eq. 21.....	72
Eq. 22.....	72
Eq. 23.....	72
Eq. 24.....	72
Eq. 25.....	72
Eq. 26.....	72
Eq. 27.....	73
Eq. 28.....	73
Eq. 29.....	73
Eq. 30.....	74
Eq. 31.....	74
Eq. 32.....	74
Eq. 33.....	74
Eq. 34.....	74
Eq.35	75
Eq. 36.....	75
Eq. 37.....	75
Eq. 38.....	75
Eq. 39.....	76
Eq. 40.....	76
Eq. 41.....	76
Eq. 42.....	76
Eq. 43.....	77
Eq. 44.....	77
Eq. 45.....	77
Eq. 46.....	77
Eq. 47.....	77
Eq. 48.....	78
Eq. 49.....	78

1. Background

1.1. Proteins are actively turned over in mammalian cells

Cells are the simplest and oldest form of life, and the quintessence of the logic behind all living organisms: to proliferate, through anabolic processes that transform the environmental substance into building blocks of itself while maintaining the robust minimalist form through division. Cellular proteins are the primary building blocks and the principal biochemical function carriers of the cell. Synthesised from 20 simple amino acids in a linear form, the programmable sequence and length of proteins give rise to the nearly infinite possibility of higher-order structures that can be evolutionarily selected for different tasks, ranging from catalysing reactions of small molecules to complex machinery that synthesise and degrade other proteins, to support internal cell structure physically, and so forth. In mammalian cells, there are roughly 3×10^9 proteins in a single cell (measured in NIH 3T3 fibroblasts), occupying 15-35% of cell volume (Milo, 2013) and made of more than half of cell dry mass (Mellblom and Enerbäck, 1979). It makes protein synthesis the most significant energy consumer among all cellular processes, accounting for more than half of the total energy consumed in growing microorganisms and at least 20% in human cells (Rolfe and Brown, 1997). Since protein synthesis is so energy-consuming, there is significant evolution pressure for cells to minimise the energy cost of proteome maintenance (Brown, 1991; Org/Qrb et al., 2020), and as a result, protein concentration becomes the limiting factor of the cell theoretical maximum metabolism rate (Brown, 1991).

Rather contradictory to such an energy minimisation strategy, most cellular proteins are constantly degraded (Rock et al., 1994). The rate of active protein degradation is far from negligible. To put into perspective, near the whole proteome is degraded in young mice's liver every 24h, whereas in adult mice, that decreases to half of the proteome every 24h (Waterlow et al., 1978). The fact that protein degradation is so energy unfavourable for living organisms affirms its necessity for normal cell function. Beyond the apparent benefits that protein degradation brings, such as clearance of damaged and misfolded proteins or recycling amino acids when the environmental resource is scarce (Wheatley, 1984), there are fewer discussed points that I would like to highlight.

1. In multicellular organisms, the division rate of the cells has to be tightly controlled to maintain the number and proportion of different cell populations, which means that the ability of cells using dilution rate to control protein level is limited. Protein degradation hence plays a more prominent role in keeping cellular protein at an optimal range. When cells stop dividing, protein degradation is the sole process that counters protein synthesis.

- Since proteome composition determines most cell functions, when the need arises for changing cellular function and propriety, for example, during differentiation, it can only be achieved by turnover of cellular proteome through degradation and dilution.

The active degradation of cellular proteins means that protein concentration is now determined by the synthesis rate, degradation rate and dilution rate (for dividing cells) altogether. This posed an unavoidable problem: if specific global protein concentration is to be maintained, coordination between protein synthesis, degradation and dilution rates has to be present (Fig. 1).

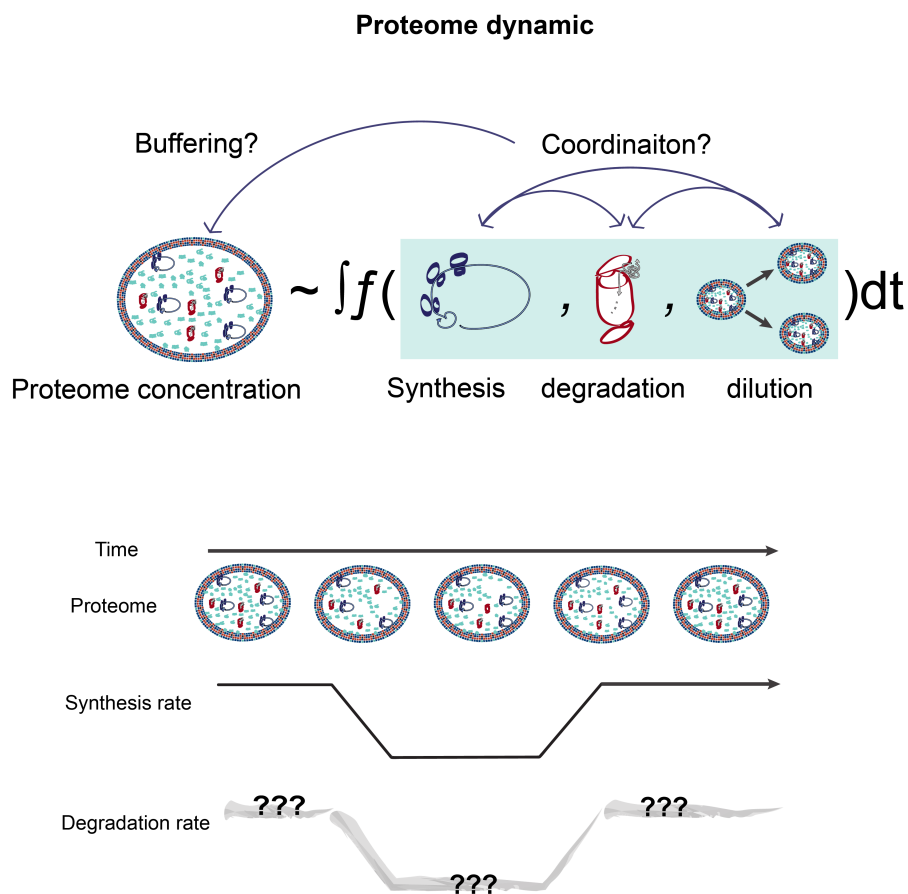


Figure 1 | The proteome dynamic is a function of protein synthesis degradation and dilution.

Coordination between protein synthesis degradation and dilution, all of which can change over time, is necessary to maintain the proteome concentration.

1.2. The coordination between protein synthesis and degradation

1.2.1. Protein synthesis and growth

For synthesising macro-biomolecules such as RNAs and proteins, constraints are not only the abundance of substrates such as ribonucleotides, amino acids, ATP, GTP etc. but also the availability of molecular machines required to catalyse these reactions. All proteins are synthesised by a sophisticated protein-RNA complex called ribosomes, whose job is to translate information coded by mRNAs into polypeptides which are then matured into proteins. Despite each mRNA being translated at its own rate, a globe protein synthesis rate can be defined as the sum of synthesis rates for all individual proteins, the unit of which is the amount of protein synthesised per unit of time or the protein concentration synthesised per unit of time.

Protein synthesis needs to be tightly regulated, especially in multicellular organisms whose constitution is only possible because of the precise spatial and temporal control of biomass accumulation. As such, protein synthesis serves as a point of integration of information relayed by various signalling pathways, metabolic states, as well as concentrations of micro and macromolecules. These mechanisms are often intertwined and complicated further by the upstream processes, such as transcription and mRNA processing. To dissect pathways controlling protein synthesis is beyond the scope of this thesis.

On the other hand, it is relevant to identify the mechanisms that set the limit to the global synthesis rate. When cells maintain the same division rate throughout generations, protein accumulation has to be exponential, as the accumulation of the cell number, so that each generation of daughter cells is equal in their protein content. Since the ribosome synthesises all the proteins, it self-replicates, which forms the basis of such exponential accumulation of total protein. Following this logic, the higher percentage of the proteome is ribosomes (ribosomal content), the higher the synthesis rate cells can achieve. Paradoxically, it is obvious that the proteome containing only ribosomes would not be viable. Consequently, the ribosome subsistence has to compete for resources with other cellular processes, which sets the ceiling of the ribosomal content and the production rate of proteins. In bacteria and yeast, it is well established that the protein synthesis rate is governed by ribosomal concentration, which increases linearly with growth rate (rate of accumulation of biomass) (Calabrese et al., 2022; Kafri et al., 2016; Metzl-Raz et al., 2017; Scott et al., 2010; Scott and Hwa, 2011). Although such ‘growth law’ is less established in mammalian cells, we expect that the same constraint applies to some mammalian cell lines where proliferation is exponential.

The protein synthesis rate is also limited by how much it can increase in a fixed period. This is because a sudden increase in protein production will burden auxiliary processes such as protein folding

machinery and mechanisms dealing with accumulating reactive oxygen species (ROS), a by-product of redox protein folding. The cellular burden-sensing mechanisms form a feedback loop that limits the temporal change in protein synthesis. The pathways involved will be discussed in the following chapters.

The synthesis rate of individual protein species depends on many factors. Since different mRNA species compete in the same ribosome pool, mRNA abundance will determine the frequency of its interaction with ribosomes, which limits the translation rates in healthy proliferating cells (Shah et al., 2013). When set aside the effect of mRNA concentrations, the other most prominent factor is the mRNA structure at the 5' untranslated region (5' UTR), which determines the translation initiation rate (Dvir et al., 2013; Jackson et al., 2010; Leppek et al., 2017; Shah et al., 2013). In some cases, the synthesis rate of each protein species can be dramatically altered. One such example is when cells are experiencing oxidative stress or protein folding stress, which can trigger the inhibition of synthesis for the majority of proteins that are cap-dependent, but at the same time, permits a sub-group of mRNAs that contain internal ribosome entry site (IRES) to be preferentially translated (Lacerda et al., 2016; Shatsky et al., 2018; Terenin et al., 2016). However, at the macro scale of the whole cell proteome, the relative differences between translation rates of different mRNAs and protein composition are largely maintained for cells in different conditions (Brunner et al., 2022). This is true even comparing stressed with unstressed cells (Gonen et al., 2019; Moro et al., 2021), which can arguably permit global protein synthesis to be monitored by one or a few reporter proteins.

1.2.2. Protein degradation

Protein degradation is carried out by two independent processes: the ubiquitin-proteasome system (UPS) and the autophagy-lysosome pathway. In the autophagy-lysosome pathway, endogenous proteins are degraded in bulk through engulfment by double membrane-bound vesicles called autophagosome (Macroautophagy) or through lysosome directly by invagination of the lysosomal membrane (Microautophagy) (Glick et al., 2010). However, the autophagy-lysosome pathway is less relevant for achieving protein flux equilibrium at a steady state (Rothman, 2010). There are two reasons for this argument. First of all, it has been found that UPS degrades the majority of cellular proteins, a discovery credited to the development of proteasome-specific inhibitors (Rock et al., 1994). In addition, only the UPS can theoretically achieve proteome equilibrium as it follows the law of mass balancing, whereas the autophagy-lysosome degradation is largely indiscriminate and results in all proteins being degraded at the rate of membrane fusion with the lysosome. This means the rate of autophagy-lysosome degradation can only be controlled by feedback mechanisms which by themselves cannot establish balance (Rock et al., 1994). This thesis will mainly focus on UPS. Nevertheless, the autophagy-lysosome pathway can deal with an imbalance in proteostasis by a feedback loop, which could be

important in non-equilibrium states. Evidence suggests they play a vital role in proteome maintenance in quiescent cells (Lee and Goldberg, 2022; Zhang et al., 2017, 2016).

The UPS pathway consists of two steps: first, proteins destined for degradation are covalently conjugated with chains of a small protein named ubiquitin by successive reactions first saw ubiquitin conjugates with ubiquitin-activating enzyme (E1). Then ubiquitin is transferred onto ubiquitin-conjugating enzyme (E2), a reaction catalysed E1. Finally, by yet another middle man called ubiquitin ligase (E3), it brings together E2 and target protein and transfers ubiquitin onto the latter. In the second step, proteins tagged with ubiquitin chains for destruction engage with 26S proteasomes through the ubiquitin receptors of the 19S proteasome regulatory particle (RP). RP unfolds the protein and pumps it into the 20s proteasome core particle (CP), where it is cleaved by the proteolytic centre of CP. There are only 2 E1s in humans, against about 30 E2s and an armada of more than 700 E3 ligase genes encoded by about 5% of the human genes (Li et al., 2008). This hierarchical structure probably reflects the need for both substrate specificity carried out by numerous E3s and global control centralised by several E1s and E2s. Many E3 enzymes form large protein complexes and are themselves regulated both transcriptionally and post-transcriptionally. All these layers of complexity pose a great challenge for decoding protein degradation.

The proteasome regulates almost every aspect of cellular activity, from cell cycle progression, differentiation, and antigen processing, to the activity of signalling pathways. Many proteins are constitutively synthesised only to be degraded rapidly to prevent any accumulation, such as p53, β -catenin, and I κ B to name a few among the endless list. In most cases, the degradation of individual protein species is regulated by the activity of its corresponding E3 ubiquitin ligase rather than the proteasome itself. Thus, the degradation rate or half-life of particular protein species can change dramatically while the overall degradation rate of the cell is barely affected.

Multiple layers control the activity of the proteasome: transcription of proteasome subunits, assembly, intracellular translocation, and modifications of proteasome subunits that affect its ATPase or peptidase activity. It is still largely an ongoing effort to elucidate the cellular mechanisms that regulate the proteasome, but there is no question about their complexity and abundance. Transcriptionally, proteasome expression can be controlled by different groups of transcription factors under diverse conditions, such as NFE2 Like BZIP Transcription Factor 1,2 and 3 (NFE2L1, NFE2L2, and NFE2L3, also known as Nrf1, Nrf2, and Nrf3); signal transducer and activator of transcription 1, 3 (STAT1, 3); nuclear Factor- κ B (NF- κ B), p53, and transforming growth factor- β (TGF- β), etc. (Kamber Kaya and Radhakrishnan, 2021). Some of these pathways will be covered in the following chapters.

One regulatory mechanism that is quite unique to the proteasome is its assembly, which requires specialised chaperone proteins and contains multiple intermediate steps. Assembly of 20S CP is assisted by proteasome assembling chaperones 1,2,3,4 (PAC1, PAC2, PAC3, PAC4) and proteasome maturation protein (POMP). (Coux et al., 2003; Fricke et al., 2007; Murata et al., 2009). In addition, a functional proteasome requires the attachment of co-activator complexes, as the passage leading to the catalytic centre of 20S CP is structurally obscured without a co-activator (Groll et al., 1997; Löwe et al., 1995). Apart from the aforementioned classic 19S RP, which engages with ubiquitinated proteins or proteins containing UBL (ubiquitin-like) / UBA (ubiquitin-associated) domains, three other co-activators have been discovered, namely PA28 $\alpha\beta$, PA28 γ and PA200. Unlike 19S RP, none has been shown to degrade ubiquitinated proteins of the canonical UPS pathway (with a few exceptions) or have ATPase activity, which probably limits their substrates to rather small proteins or peptides (Kors, 2019). Among them, PA28 $\alpha\beta$ and, to a less extent, PA28 γ have been shown to degrade protein damaged by oxidation and PA28 $\alpha\beta$ -20S complex forming is induced during oxidative stress (Pickering and Davies, 2012).

The proteasome is subjected to hundreds of post-transcription modifications (Kikuchi et al., 2010), including phosphorylation, ubiquitination, polyADP-ribosylation, O-glcNAcylation, methylation, acetylation, s-glutathionylation, 4-hydroxy-2-nonenal modification, etc. (Kors, 2019). Although the functions of most of them are still unclear, many phosphorylation events of 19S RP have been elucidated. It has been demonstrated that phosphorylation by DAPK-related apoptosis-inducing kinase 2 (DRK2), protein kinase A (PKA), protein kinase C (PKC), and calcium/calmodulin-dependent protein kinase II (CaMKII) activate proteasome in different contexts (Djakovic et al., 2009; Guo et al., 2015, 2011; Lokireddy et al., 2015; Pathare et al., 2012; Ranek et al., 2014; Sun et al., 2017; VerPlank and Goldberg, 2017; Zhang et al., 2007). Meanwhile, pharmacological screening has revealed p38 as a negative regulator of proteasome activity through phosphorylation of 19S subunit Rpn2 (PSMD1) (Lee et al., 2010; Leestemaker et al., 2017).

As both protein synthesis and degradation are ATP-driven processes, they could be limited by the cellular energy state. A cross-species comparative study has shown that the protein degradation rate negatively correlates with the animal's life span (Swovick et al., 2021). They further demonstrate that the degradation rate correlates with the production of ATP (Swovick et al., 2021). ATP level can also affect proteasome via its assembly since the binding of ATP to ATPases of 19S RP is a prerequisite for 26S proteasome formation (Kim et al., 2013; Liu et al., 2006).

There is evidence that suggests that protein degradation can also be regulated by altering ubiquitination on a global scale. It has been found that upon heat shock or sodium arsenite-induced oxidative stress, ubiquitination of the global proteome is stimulated (Lee and Goldberg, 2022).

All these aforementioned regulatory mechanisms integrate the UPS pathway into a wider cellular signalling, metabolism, and homeostasis network. Thus, it would be highly challenging, if at all possible, to unravel the contributions of each mechanism to the *a posteriori* protein degradation rates in physiological conditions. Despite the complexity of the possibilities of determinants of degradation rates, degradation of most proteins can be well modelled with a simple first-order reaction, suggesting a single reversible reaction rate can describe the whole chain of events. However, it could also be misleading when identifying the rate-limiting step. In general, it is perceived that ubiquitination is the rate-limiting step for UPS as it is significantly slower compared to the digestion of ubiquitinated protein by the proteasome. However, the proteasome capacity could be easily saturated, due to its unique step-wise and irreversible nature of degrading proteins, thus controlling the overall degradation rate. In fact, it has been well documented that an increase in proteasome activity enhances the degradation rate of global cellular proteins, which is an apparent contradiction if ubiquitination is the sole rate-limiting step (Guo et al., 2015; Lokireddy et al., 2015; VerPlank et al., 2020).

1.2.3. Dilution and proteostasis

Cellular processes other than protein degradation are also involved in the turnover of proteins. Change in growth/division rate can change the dilution rate, and cell size regulation can control protein concentration. Both cell cycle duration and cell size in yeast and mammalian cells are determined by a group of short-lived proteins, whose concentrations are taken by cells as indicators of the protein accumulation rate (or the synthesis rate if the degradation is static). Some of these proteins regulate the G1/S checkpoint, a critical event that marks the commitment of cells to divide.

Cyclin 3 (Cln3) in yeast or its mammalian homologous Cyclin E is a vital cell cycle regulator. Cyclin E - Cdk2 activity promotes the cell cycle progression through the G1/S check point (Dirick and Nasmyth, 1991; Lew et al., 1991; Tyers et al., 1992). It was first thought that cells used Cyclin E to measure the protein synthesis rate (Polymenis and Schmidt, 1997; Wang et al., 2009). However, later studies have shown that Cyclin E concentration is mainly unchanged during G1, which leads to the theory that cell size is controlled by growth-dependent dilution of Whi5, an inhibitor of Cyclin E - Cdk2. It has also been shown that the E2F transcription factor 1 (E2F1), which regulates Cyclin E expression, is used by cells as a synthesis rate sensor (Zielke et al., 2011). Jones et al. (2017) have demonstrated that the transition between G2/M is also cell-size dependent in fission yeasts.

Being directly regulated by protein concentration, the dilution rate has demonstrated the adaptability to proteostasis when its link with protein concentration is temporarily uncoupled. In fission yeasts, when applying osmotic oscillations, the protein concentration increases as the cell volume expansion slows down. When such perturbation is removed, cells experience a period of rapid growth that restores the

protein concentration (Knapp et al., 2019). However, when the opposite happens as cells are overgrown in size, it has also been shown that the protein synthesis will not adapt to the change in dilution, and as a result, the proteome is diluted (Neurohr et al., 2019). Rather curiously, a recent study has shown that the protein degradation rate increases concomitantly with the cell size but not the synthesis (Liu et al., 2021).

Theoretically, dilution and global degradation should compensate for each other. We would expect the inhibition of protein degradation, without the consideration of any stress response, would result in temporal protein accumulation, which accelerates the dilution rate. Excessive protein degradation should cause the opposite effect. On the other hand, changes in the dilution rate should equally affect concentrations of specific proteins, which are used by cells to measure the turnover rate. However, data on how the dilution and degradation coordinate are non-existent.

1.2.4. Coordination of synthesis and degradation

Proliferating cells constantly change in size and total protein amount throughout the cell cycle; therefore, individual cells are never in a steady state, making it challenging to compare different proteostasis states. However, steady states can exist globally once hundreds of thousands of cells from different cell cycle stages are averaged. We will refer to such meta state as the ‘average cell’. When the ‘average cell’ is at a steady state, its volume, degradation rate, synthesis rate, and dilution rate are all constant. The existence of the dilution rate despite the constant volume of the ‘average cell’ is because although the ‘average cell’ does not physically grow, the amount of protein synthesised is always more significant than the amount of protein degraded so that biomass can accumulate over time. The ‘average cell’ model simplifies the planning of experiments, as cell lineage tracking will not be necessary since only the global mean matters. The synthesis rate in cells can be defined as the total protein concentration synthesised per unit of time and is treated as a zero-order reaction. Both the degradation and the dilution can be modelled as first-order reactions, the units of which are time^{-1} . This zero-order/ first-order model always promises the presence of steady states regardless of the numerical combinations of synthesis, degradation and dilution rates, as the degradation and dilution rates exist in a different dimension from the synthesis rate (Eq. 1). For example, from a steady state, if the protein synthesis rate increases while the sum of degradation and dilution rates (which is the total protein turnover rate) remains the same, after a relaxation period of the system, a new steady state will be reached where the protein concentration increases the same fold as the synthesis. This simplified zero-order/ first-order model does contain an assumption that the cellular protein concentration and content should not significantly change so that the self-synthesising and self-destructing of synthesis and degradation machinery can be ignored.

Eq. 1

$$[P] = \frac{s}{k}$$

$$k = K_{deg} + K_{dil}$$

In Eq.1, $[P]$ is the protein concentration. s is the synthesis rate (unit: number of proteins \cdot volume $^{-1}$ \cdot time $^{-1}$), k is the total turnover rate (unit: time $^{-1}$), which is made of the degradation rate K_{deg} and the dilution rate K_{dil} (unit of both: time $^{-1}$).

It has been generally perceived that protein synthesis is the driving force for cellular metabolism, while the role of protein degradation is relatively passive. After all, the essence of life is to accumulate biomass. This assumption is well supported by the observation in bacteria and yeasts where the accumulation of biomass is predominantly dependent on protein synthesis, while the active protein degradation rate remains mostly the same and merely offsets the protein accumulation rate (Calabrese et al., 2022; Kohanim et al., 2018). The protein degradation rate is even relatively higher when the synthesis rate is restricted by nutrients so that amino acids can be recycled within the cells (Calabrese et al., 2022). All these studies are conducted in contexts of few restrictions to the dilution rate, rendering it the principal force to maintain protein concentration and counterbalance protein synthesis. However, there are many contexts, especially in mammalian cells, where the dilution rate is rigidly restricted. Consequently, maintenance of the protein concentration will be more dependent on the buffering effect of the degradation rate. In non-proliferating cells, even temporal fluctuation of protein synthesis may not be sustainable without action from degradation.

Theoretically, between protein synthesis and degradation, the coordination can be achieved by a group of short-lived proteins whose concentrations are both sensitive to changes in protein synthesis and degradation. When taking dilution into account, this strategy may still be sufficient, provided dilution is also regulated by the accumulation of short-lived protein. Indeed, the transcription of the proteasome, for example, is regulated by short-lived transcription factors such as Nrf1, Nrf2, and Nrf3, which forms a feedback mechanism (Steffen et al., 2010), while the dilution rate is controlled by the accumulation of aforementioned short-lived regulators (See Chapter 1.2.3). However, whether short-lived proteins coordinate protein synthesis, degradation, and dilution has never been thoroughly tested.

Shreds of evidence have emerged both supporting and opposing such coordination between protein synthesis and degradation in various cellular contexts. Work from Alber et al. (2018) demonstrates that in mammalian cells, the synthesis and degradation rate of endogenous proteins can be measured by tagging them with a tandem fluorescent timer (tFT or “Timer” for the rest of the thesis) (Alber et al., 2018; Khmelinskii et al., 2012). It was found that in single cells, synthesis and degradation rates for endogenous proteins are correlated, suggesting coordination exists between the two rates. (Alber et al., 2018). A study conducted in the human THP-1 myelomonocytic leukaemia cell line and the mouse

C2C12 cell line concludes that degradation rates are primarily unchanged during differentiation, whereas protein synthesis is the main driving force for change in protein level (Kristensen et al., 2013). However, the low time resolution (degradation rates were calculated from a single chase time point at 24 or 48 h after differentiation) prevents any definitive conclusion from being drawn. A more recent study has shown that activation of MCF10A cells by EGF signalling induces a pulse of protein synthesis, accompanied by a temporal increase in the protein degradation rate for some of the quantified proteins (Golan-Lavi et al., 2017). This is consistent with evidence from *C. elegans* that EGF signalling can activate UPS and enhance the lifespan of the animal (Liu et al., 2011). Using the bleach-chase method, Eden et al. (2011) investigated the change of the degradation and dilution rates in response to drug perturbation and found that in all the drugs tested, change in only dilution could well explain the change in protein total turnover rate (Eden et al., 2011). However, in all but one condition, decreases in cell proliferation are more than 85%, raising the question if such conditions are sustainable and whether actual steady states are reached. Very recently, several studies have discovered a periodic fluctuation of dry mass accumulation in mammalian cells (Ghenim et al., 2021; Miettinen et al., 2022). Ghenim et al. (2021) have identified that the source of this ultradian rhythm is the fluctuation in protein degradation rates (Ghenim et al., 2021).

Despite these examples, the dynamics of interaction between protein synthesis and degradation are poorly understood, even as synthesis and degradation rates of individual proteins have been characterised in detail across different organisms and tissues (Rolfs et al., 2021). In all cases where dynamics of synthesis and degradation are studied, they lack temporal resolution, which is inherent to any traditional pulse-chase methods such as Stable isotope labelling by amino acids in cell culture (SILAC), fluorescence bleach chase, or translation inhibitor cycloheximide (CHX) chase. The starting point of understanding coordination between synthesis and degradation is to explicate the timescale and amplitude where the change in global protein synthesis and degradation could be expected. This will require well-defined and physiologically relevant contexts and accurate measurements of the protein level, synthesis, degradation, and dilution rates with good temporal resolution.

1.2.5. How do cells deal with imbalances in protein synthesis and degradation?

How cells deal with the imbalance in protein synthesis and degradation would yield insights into the mechanism and dynamic interplay between protein synthesis and degradation. Even with a non-physiological level of perturbation, valuable information can be gained about the function and capacity of various pathways. A form of such imbalance manifests itself as proteotoxicity. Proteostasis has been studied extensively in the context of proteotoxicity, where unfolded proteins accumulate inside cells in various scenarios, such as the inhibition of proteasome activity. Proteotoxicity is often related to oxidative stress since hydrogen peroxide is a by-product of redox protein folding. When ER

homeostasis deteriorates as unfolded proteins accumulate in ER, free radicals also accumulate in ER, causing the oxidative stress response. Oxidative stress is often triggered by a sudden increase in protein synthesis, even without clear proteotoxicity.

In response, mammalian cells can activate several mechanisms attempting to resolve such stress. Unfolded stress response (UPR) pathway is triggered upon the accumulation of unfolded proteins in ER that exhaust the ER Hsp 70 chaperon BiP, which binds aliphatic residues of proteins (Flynn et al., 1991). This will lead to the activation of inositol requiring enzyme- α (IRE1 α), protein kinase RNA-like endoplasmic reticulum kinase (PERK), and activating transcription factor 6 (ATF6), as they are normally repressed by BiP (Bertolotti et al., 2000; Bukau et al., 2006; Kopp et al., 2019; Pincus et al., 2010). The reaction of UPR is multitudes. PERK activation leads to the phosphorylation of initiation factor eukaryotic translation initiator factor 2 α (eIF2 α), which inhibits all the cap-dependent protein translation. In the meantime, a massive transcription programme is led by three main transcription factors, ATF4, X-box binding protein 1 (XBP1s) and activating transcription factor 6 (ATF6f) downstream of UPR, which up-regulate genes involved in protein folding, ER-associated degradation (ERAD), autophagy, and protein quality control (Hetz, 2012). In addition, PERK can also stabilise Nrf2 by phosphorylation (Cullinan et al., 2003; Cullinan and Diehl, 2004). Nrf2 is a master regulator of cellular redox homeostasis. It can activate genes regulated by antioxidant response element (ARE) enhancers. In case of chronic stress that is beyond the ability of cells to resolve, apoptosis will be induced through Caspase2 and p53. It has been shown in yeasts that mutation in the UPR activator compromises growth rate, indicating that basal UPS activity is essential for cellular functions (Schmidt et al., 2019).

Another pathway relevant to restoring proteome equilibrium is the proteasome recovery pathway. It has long been known in yeasts that the expression of proteasomal subunits is controlled by Rpn4, an extremely short-lived transcription factor and thus ideal as a proteasome activity sensor. No ortholog of Rpn4 is found in mammalian cells. However, over the past ten years, a pathway that functions similarly has been elucidated. It starts with another very short-lived transcription factor NFE2L1 (Nrf1), which is rather curiously an ER transmembrane protein. It is continuously degraded by proteasome via retro-translocation from ER lumen to the cytosol by valosin-containing protein (VCP or p97). When Nrf1 accumulates as a result of insufficient proteasome activity, it is cleaved from the ER membrane by DNA damage inducible 1 homolog 2 (DDI2) and enters the nucleus where it activates transcription of all proteasome subunits by binding to their ARE enhancers (Radhakrishnan et al., 2010; Sha & Goldberg, 2014). Such regulation pathways would, in theory, establish a link between synthesis and degradation. However, their role beyond proteotoxic stress has not been well documented.

1.3. Methods to quantify proteostasis

Based on temporal resolution, we classify methods that quantify protein synthesis and degradation into two categories: 1. Discontinuous methods that rely on ‘pulse’ or ‘pulse-chase’ procedure and 2. continuous methods such as fluorescent Timer. The separation of these two categories is not absolute, as when the time interval of the ‘pulse’ or ‘pulse-chase’ phase is short enough, it can provide continuous measurements with proper modelling.

For discontinuous methods, the ‘pulse’ phase allows a tracer molecular to be incorporated into the protein over a certain period, which can be used to measure the rate of protein accumulation, while the ‘chase’ phase measures the turnover of tagged proteins. Obviously, discontinuous methods are best suited for situations where temporal information is not crucial, such as at steady states. Nevertheless, the short-coming of temporal resolution is compensated by their superiority in proteome coverage and accuracy. One of the early examples of such methods is radiolabelling, which uses radioactive isotopes such as ^{35}S to label amino acids such as methionine. ^{35}S -methionine, once incorporated into proteins, can be quantified either on the protein gel by scintillation spectroscopy or by mass-spectrometry (Bonifacino, 2001; Coligan et al., 1983; Meisenhelder and Hunter, 1988). Radiolabelling was quickly replaced by its successor, stable isotope labelling by amino acids in cell culture (SILAC). It uses non-radioactive stable isotopes ^2H , ^{13}C , and ^{15}N to label amino acids such as arginine, lysine and leucine (Ong et al., 2002). Dynamic SILAC, which chases the turnover of isotope-labelled proteins, can resolve both synthesis and total turnover rates at the same time (Doherty et al., 2009; Pratt et al., 2002). This method has been employed successfully for quantifying proteome turnover both *in vivo* and *in vitro*. Most recent development integrates dynamic SILAC with tandem mass tags (TMT) to allow further sample multiplexing (Welle et al., 2016).

Without mass-spectrometry, ‘pulse’ or ‘pulse-chase’ labelled proteins can be visualised and quantified by fluorescent tagging. Certain amino acid analogs such as L-Homopropargylglycine (HPG) and azidohomoalanine (AHA), both are analogs of methionine carrying alkyne and azide group respectively, can be conjugated with a functional molecule via Copper (I) Catalysed Alkyne-azide 1,3-Dipolar cycloaddition (CuAAC, or click reaction) (Dieterich et al., 2010, 2006; Tornøe et al., 2002). This functional molecule can be azide or alkyne-carrying fluorophores. When used in ‘pulse’, protein synthesis rates can be inferred from the fluorescent-tagged proteins that are newly synthesised. They can also be used in ‘pulse-chase’ to measure the global turnover rate. O-propargyl-puromycin (OPP), an alkyne analog of puromycin, can be used similarly in ‘pulse’ and visualised by click reaction; however, it generates truncated proteins whenever OPP is incorporated at the C-terminal of the synthesising proteins (Enam et al., 2020; Liu et al., 2012). These truncated proteins have a much shorter half-life compared to full-length proteins (Lacsina et al., 2012).

'Pulse' or 'pulse-chase' methods are frequently used in microscopy. The advantage of microscopy is that the high sampling frequency can be obtained without an off-putting increase in labour or cost, so it is possible to obtain synthesis or turnover rate measurements with good time resolution. With proper modelling tools such as the Bayesian method of sequential inference (Mark et al., 2018; Metzner et al., 2015), it is even possible to extract continuous measurements from 'pulse' or 'pulse-chase' data. In addition, microscopy can provide single-cell measurements. SNAP tag (Keppler et al., 2004, 2002) has been successfully used for microscopic pulse-chase labelling as the fluorogenic ligands of SNAP can form covalent bonds with the tagged proteins (Alber et al., 2018; Alber and Suter, 2018; Bojkowska et al., 2011). Alber et al. (2018) applied this method to measure the half-life of endogenously tagged protein in mouse embryonic stem cells (mESC). Bojkowska et al. (2011) have used the SNAP tag to quantify protein turnover in adult mice. The bleach-chase method can also be used to measure the protein degradation rate (Eden et al., 2011; Geva-Zatorsky et al., 2012). In this method, all fluorescent proteins in the cells are bleached at time point 0, and the accumulation of new proteins is recorded over time, which can be used to deduce the total turnover rate assuming a stable total protein level (Eden et al., 2011; Geva-Zatorsky et al., 2012). In theory, photo-switchable and photo-activable fluorescent proteins can be used similarly to the SNAP pulse-chase method. Photo-switchable fluorescent proteins can change emission wavelength upon stimulation by specific excitation light, while photo-activable fluorescent proteins only become fluorescent when activated by a specific light source (Fuchs et al., 2010; Gurskaya et al., 2006; Wu et al., 2011; Zhang et al., 2007). A photo-switchable fluorescent protein Dendra has been used in *drosophila* to study protein turnover in septate junctions during development (Babatz et al., 2018).

The label-free approach could be used in 'pulse' or 'pulse-chase' methods using protein synthesis or degradation inhibitors. However, these inhibitors could trigger widespread cellular changes and often interfere with proteostasis. Translation inhibitors such as cycloheximide have been shown to alter degradation (Lokireddy et al., 2015) and dilution rates, while proteasome inhibitors also activate stress response and down-regulate synthesis rate.

Fluorescent timers (FT) and tandem fluorescent timers (tFT) are the other classes of tools that provide continuous measurements by default. Fluorescent timers are fluorescent proteins that switch excitation wavelengths during their maturation, which lasts for a few hours (Keppler et al., 2004). The ratio between the immature fluorescence and mature fluorescence proteins reports the average protein age over time directly, from which the synthesis and degradation rate can be modelled. The first discovered FT is a mutant form of DsRed (DsRed-E5). It cannot be used to tag proteins as it is a tetramer. Nevertheless, FTs have found applications in monitoring gene expression and reporting the age of organelle (Duncan et al., 2003; Keppler et al., 2004; Mirabella et al., 2004). Since then, monomeric

fluorescent timers have been engineered and employed for the study trafficking of lysosome-associated membrane protein type 2A (LAMP-2A) and dense-core vesicle exocytosis in mammalian cell lines (Subach et al., 2009; Tsuboi et al., 2010).

Tandem fluorescent timers are fusion proteins composed of two monochromic fluorescent proteins with distinct maturation rates. The disparity in maturation rates allows the fluorescent intensity ratio between the slow-maturing partner and the fast-maturing to be taken as relative protein age (Khmelinskii et al., 2012). The evolution of protein age over time can be again modelled to obtain synthesis and turnover rates (Alber et al., 2018; Barry et al., 2016). Since its creation, tFT has been adopted in several protein turnover studies in yeasts, *drosophila* and *zebrafish* (Donà et al., 2013; Durrieu et al., 2018; Kats et al., 2018; Knop and Edgar, 2014). Alber et al. (2018) applied a mammalian cell-optimised version of tFT to tag endogenous proteins in mESC to study their turnover dynamics during the cell cycle, which demonstrated its potential in modelling synthesis and degradation rates in a non-steady-state context.

To summarise, the advancement in proteomics provides means to quantify synthesis and degradation rates for thousands of proteins with a snapshot. However, it would be extremely costly to reach the temporal sampling rate that is required to study the dynamics of proteostasis. tFT is a good option to study protein homeostasis by microscopy, providing both snapshot and dynamic information. However, for tFT, solving synthesis and turnover rates by modelling is non-trivial, as it is, for the moment, heavily relied on presumptions of dynamics of synthesis and turnover. Implementing more sophisticated mathematical modelling tools (including the method demonstrated in this thesis) will be imperative to study complicated dynamics.

1.4. The objective of the thesis

Despite our current knowledge about proteostasis in mammalian cells, little is known about how protein synthesis and degradation are coordinated and how it affects the proteome concentration in physiological relevant cellular states. Furthermore, no study has convincingly elucidated the mechanisms behind such coordination. This work uses the tandem fluorescent timer (referred to as ‘Timer’) together with other microscopic, transcriptomic and biochemistry tools, aided by computational modelling, to dissect the coordination between synthesis, degradation and dilution rates in well-defined equilibrium and non-equilibrium contexts.

This thesis will be divided into the following parts.

1. Develop and validate a microscopy-computational modelling workflow to calculate synthesis and degradation rates from the tandem fluorescent timer in non-steady states.
2. Measure protein synthesis and degradation rates in different steady states.

3. Measure time-dependent evolution of synthesis and degradation rates in various non-steady states.
4. Determine how protein synthesis and degradation are coordinated.

2. Results

2.1. Timer as a method to monitor global proteostasis dynamics

The tandem fluorescent timer of sfGFP and mOrange2 has demonstrated the ability to measure its own synthesis and degradation rates at both steady and non-steady states. This was achieved by fitting sfGFP and mOrange2 time-lapse traces with a selection of functions and modelling with a set of differential equations (Eq. 2) (Alber et al., 2018; Knop and Edgar, 2014).

Eq. 2

$$\begin{aligned}\dot{B}_G &= s - (m_G + k)B_G \\ \dot{B}_R &= s - (m_R + k)B_R \\ \dot{G} &= m_G B_G - kG \\ \dot{R} &= m_R B_R - kR\end{aligned}$$

k is the protein degradation rate. m_G and m_R are the maturation rates of sfGFP and mOrange2, respectively. B_G and B_R are the concentrations of non-fluorescent sfGFP and mOrange2 protein. G and R are the concentrations of matured sfGFP and mOrange2 protein. The model also has a hidden parameter α , which multiplies the sfGFP fluorescence intensity. The reason α exists is that the observed fluorescence intensities of sfGFP and mOrange2 do not correspond to the relative number of fluorescent molecules due to the difference in the exposure time and the quantum yield (QY) that are specific to each channel and fluorescent protein. This model describes that the observable fluorescence is generated by the synthesis and maturation of fluorescent proteins, which are simultaneously destroyed by protein degradation.

We modified the model to consider the effect of dilution (Eq. 2), which enabled us to use the average of the mean intensity of the Timer from each cell for modelling instead of the integrated intensity from whole lineages. This omitted the necessity of accurate lineage tracking. The latter interpretation also involved considering the change in cell volume, while the measurements derived from the mean intensity had a definite physiologic meaning regardless of the volume.

Eq. 3

$$\begin{aligned}k &= K_{deg} + K_{dil} \\ \dot{B}_G &= s - (m_G + k)B_G \\ \dot{B}_R &= s - (m_R + k)B_R \\ \dot{G} &= m_G B_G - kG \\ \dot{R} &= m_R B_R - kR\end{aligned}$$

In the new equation, the definition of k is total protein turnover, comprising protein degradation and dilution. The units of B_G , B_R , G , and R are concentrations instead of the total amount. The unit of s is *concentration · time⁻¹*.

This model also provides a snapshot of the total turnover rate at the steady state through Eq. 4, as the G/R ratio has a non-linear relation with k .

Eq. 4

$$\frac{m_R + k}{m_G + k} = \frac{G}{R} \cdot \frac{m_R}{m_G}$$

In order to use the Timer as a proxy for global proteostasis, we employ a Timer construct with a hPEST (here referred to as PEST) sequence at its c-terminal from Alber et al. (2018). The PEST sequence targets the Timer to the 26S proteasome for degradation, bypassing the ubiquitination pathway (Ghoda et al., 1989; Zhang et al., 2003), therefore measuring the global protein turnover rate. This PEST degron originates from the c-terminal of mouse Ornithine Decarboxylase (ODC⁴²²⁻⁴⁶¹, D433A/D434A) (Fig. 1a) (Li et al., 1998) and has been proven to dramatically reduce the half-life of the otherwise very stable Timer construct (Alber et al., 2018). Very importantly, the degradation of PEST also appears to be Antizyme isoform 1 (Az1) independent, which orchestrates the rapid destruct of ODC but shows no influence in other PEST-tagged proteins (Zhang et al., 2003, Hoyt et al., 2005). In addition to the tandem fluorescent timer, a SNAP tag (Keppler et al., 2002) was inserted between the Timer-nls (nuclear localization signal) and the PEST sequence. SNAP protein can be covalently bound with fluorophores compatible with staining live cells. This design enables an independent measurement of protein degradation by pulse-chase labelling (Alber et al., 2018; Alber and Suter, 2018). The Timer-nls-SNAP-PEST fusion protein will be referred to as the ‘short-lived Timer’ and is expressed either constitutively by phosphoglycerate kinase 1 (PGK) promoter or by a doxycycline (Dox) inducible promoter. Apart from direct measurement of the proteasome activity, the short-lived Timer has the advantage of reaching equilibrium much faster, following changes in the balance of protein synthesis and degradation.

A truncated version of the PEST sequence (referred to as PEST* in Fig. 2a) failed to reduce the half-life of the Timer-nls-SNAP construct (Fig. 2b), which was consistent with a previous study on cODC ubiquitin-independent degradation (Takeuchi et al., 2008). Hence it will be referred to as the ‘long-lived Timer’, and it is constitutively expressed by elongation factor-1 α (EF1A) promoter. Both the short-lived and long-lived Timer are expressed in NIH 3T3 cells. Using different Timers allows us to sample the degradation of the different parts of the proteome. The degradation rate of the short-lived Timer was measured at $0.127 \text{ h}^{-1} \pm 0.035$ and the long-lived Timer at $0.016 \text{ h}^{-1} \pm 0.0064$ (Fig. 2b), corresponding to 5.4 and 42.9 h of half-life, respectively.

A set of constants had to be estimated and validated for the modelling of Timer, chiefly m_R , m_G , and α . m_G was difficult to measure experimentally as sfGFP folding happens in minutes. We instead used published data to set m_G to 6 h^{-1} (Pédelacq et al., 2006). m_R was estimated from experimental steady-state data (Chapter 2.2, Table. 1), using a deterministic optimization process with a cost function based on Eq. 3 (see Eq. 15), which set m_R to 0.091 h^{-1} (Fig. 2c, S1a, S1b). α could be estimated experimentally

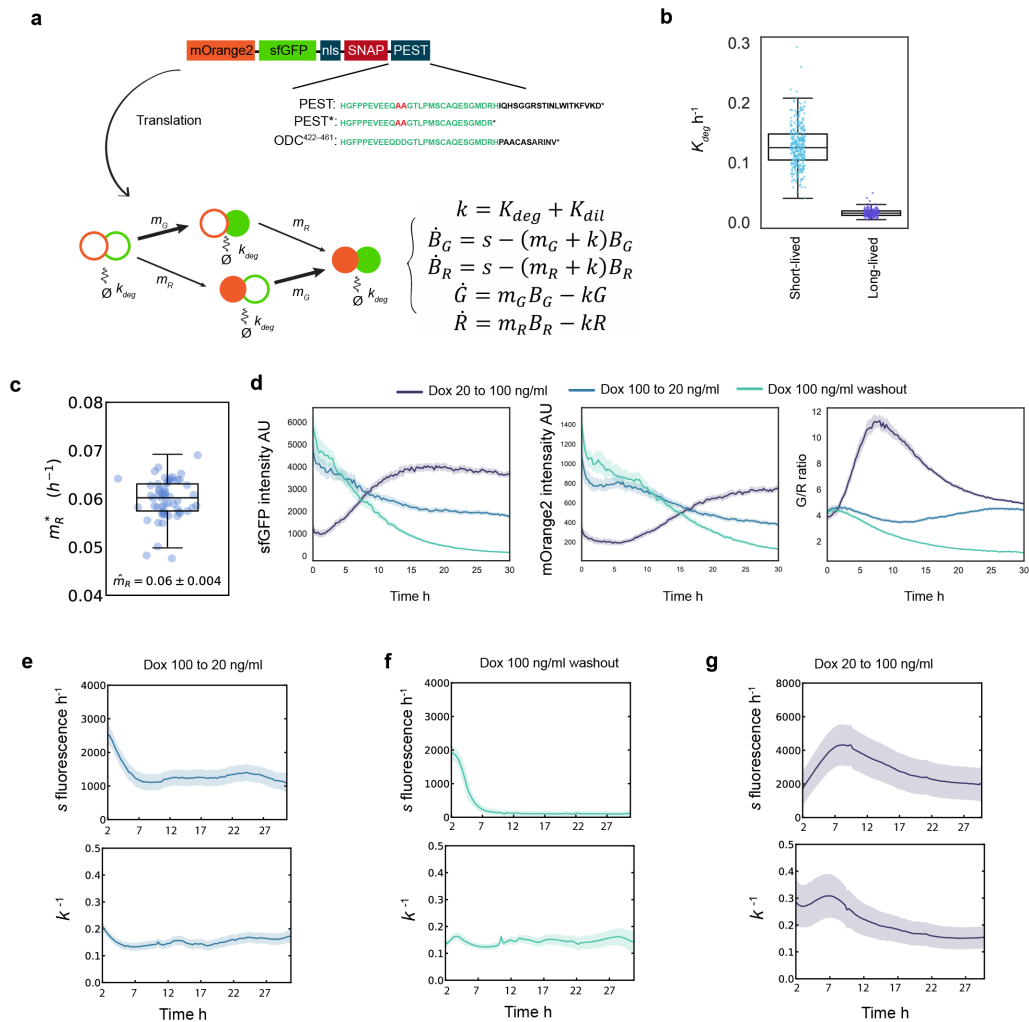


Figure 2 | Timer as a tool to measure dynamics of synthesis and degradation.

a, Scheme of Timer constructs, including the short-lived version and the long-lived version, which are different in their c-terminal PEST sequence. The murine cODC sequence is shown as a reference. For differential equations, see the explanation of Eq. 3. **b**, Degradation rates of long-lived and short-lived Timer were measured by SNAP pulse-chase labelling. Single lineages fitted data are plotted. **c**, Calculation of the mOrange2 maturation rate by fitting data from Table. 1. Each dot represents a m_R^* optimization at a different cycloheximide-induced steady state by Eq. 15. \widehat{m}_R is the median of all cost-minimized m_R^* (h^{-1}). **d**, Traces of sfGFP, mOrange2 mean intensity and the G/R ratio from the Dox inducible short-lived Timer. Corresponding concentrations of Dox were added 24 h before the movie, and concentrations of Dox were changed at the start of the movie. The median of all segmented cells per frame per condition is plotted (number of cells > 2000 for each condition at time point 0). Shading, 95% CI. s and k were calculated from Timer traces in Fig. 2d by superstatistical modelling for **e**, Dox 100 to 20 ng/ml, **f**, Dox 100 ng/ml washout, and **g**, Dox 20 to 100 ng/ml. The mean of the inferred posterior distribution is plotted. Shading: std of the posterior distribution.

using a Dox inducible Timer (Alber et al., 2018). It was assumed that no new protein could be synthesized after washing out Dox from the medium. A state as such would allow an increasing percentage of pre-existing mOrange2 proteins to mature over time. The G/R ratio eventually converged to a single value as almost all the sfGFP and mOrange2 proteins matured (Fig. 2d). α was determined experimentally each time when the exposure settings of the microscope were changed.

2.2. Validate a superstatistical Bayesian inference algorithm to infer protein synthesis and turnover rates from Timer traces

To calculate s and k dynamics at non-steady-state from Timer traces, we applied a superstatistical Bayesian inference algorithm (Mark et al., 2018; Metzner et al., 2015) (referred to as the superstatistical modelling) that can infer the distribution of time-varying parameters, namely s and k , from Eq. 3 at each time point. The advantage of this method is that no prior knowledge of the dynamics of s and k is required. This is in contrast with the technique Alber et al. (2018) applied, where a selection of functions for s and k is pre-determined to fit Timer traces.

To validate the modelling method and the estimated parameters, a Dox inducible short-lived Timer cell line was used to stage scenarios in which the synthesis rate was manipulated by changing the concentration of Dox at the time point 0. Then, time-lapse fluorescence microscopy was performed for sfGFP and mOrange2 channels at 15 min intervals. Change of Dox concentration, in theory, should only affect the synthesis rate of the Timer and the degradation rate remain constant. The fluorescence traces from the Timer exhibited different dynamics between the increase of Dox concentration and the decrease of Dox concentration, but importantly, G/R ratios of Dox 100 to 20 ng/ml and Dox 20 to 100 ng/ml conditions were converging towards the same value at the end of the movie (Fig. 2d), indicating a near steady-state had reached for both conditions with identical steady-state turnover rates k . For the Dox 100 ng/ml washout condition, G/R ratios did not converge to the same value as expected (Fig. 2d) since it could not reach the steady state for the Timer until all Timer proteins were degraded. We then calculated s and k from Timer traces by the superstatistical modelling. For the Dox 100 to 20 ng/ml and Dox 100 ng/ml washout, s and k showed expected trends as s decreased following the reduction of Dox, while k maintained more or less constant values throughout the movies (Fig. 2e, 2f). Notably, the values of k were close to 0.16 h^{-1} , which matched the predicted value (sum of K_{deg} , 0.127 h^{-1} for short-live Timer and K_{dil} , 0.047 h^{-1} for 3T3 cells). However, for the Dox 20 to 100 ng/ml condition, although the increase in s was expected, there was an unexpected increase in k during the first half of the traces, which then converged to the expected value towards the end of the traces (Fig. 2g). To assess whether the fitting of the Timer traces from the modelling was accurate, we performed a data retrodiction to calculate theoretical sfGFP and mOrange2 fluorescence traces from inferred s and k . Remarkably, the retrodicted Timer traces matched almost exactly with the experimental data for all three conditions (Fig. S1c, S1d, S1e). We deduced that the unexpected fluctuation of k was a correct interpretation from the Timer traces, rather than a problem in the modelling part. An increase in k could come from the stress response following a rapid increase of protein synthesis. In general, we conclude that our model can predict the time evolution of s and k from Timer fluorescence traces in dynamic situations.

2.3. Downregulation of protein degradation following the treatment of translation elongation inhibitor cycloheximide

To understand the coordination between protein synthesis and degradation, it is essential to create contexts where one of these rates could be manipulated globally. The challenge is to find treatments that are mild enough so that such recapitulation would be physiologically relevant. One criterion of the mildness of any treatment would be that cells reach a new steady state after such perturbation, which signifies that the manipulation is within the adaptive capacity of the cells rather than leading to a failure of proteostasis.

It has been shown that in 3T3 cells that low dose of cycloheximide (CHX) results in reduced protein synthesis and lengthened cell cycle but not causing cell death, as cells keep proliferating exponentially at a concentration as high as 0.1 $\mu\text{g/ml}$ (Medrano and Pardee, 1980). To measure the extent of inhibition of protein synthesis at such CHX concentration, 3T3 cells were treated with CHX for two days. Then, L-Homopropargylglycine (HPG), a methionine analog, was used to label newly synthesised proteins. Protein synthesis rates measured by HPG labelling showed a reduction of 2 to 3-fold at CHX 0.1 $\mu\text{g/ml}$ compared to control (Fig. 3a, S2f). However, the exact fold changes were difficult to calculate because of the uncertainty in estimating the background.

Next, we decided to use CHX to create a series of new proteostasis steady-states, where the protein degradation rate would be measured to test if it adapted to the inhibition of synthesis. We applied 56 different concentrations of CHX ranging from 0.002 to 0.5 $\mu\text{g/ml}$ to 3T3 cells carrying the short-lived Timer for 48 h since it was previously determined that sfGFP mOrange2 intensity, as well as the G/R ratio, would stabilise after 25 h of CHX addition (can be inferred from Fig. 5c). Then, the total turnover rate k and degradation rate K_{deg} were measured by SNAP pulse-chase labelling of the short-lived Timer reporter through time-lapse microscopy. The dilution rate K_{dil} was also measured from the movie. Intriguingly, raising CHX concentration caused K_{deg} to decrease correspondingly (Fig. 3b, c), indicating that the protein degradation rate reacted accordantly to the change of protein synthesis. It was also interesting that K_{dil} decreased concomitantly as the concentration of CHX raised (Fig. 3d, e). Both K_{dil} and K_{deg} were calculated by two independent methods, which yielded the same results (Fig. S2a, c). Consistent with the report from Medrano and Pardee, 1980, cells were able to proliferate exponentially at CHX concentration up to 0.2 $\mu\text{g/ml}$ (Fig. 3f).

Next, we asked if the change in k could completely compensate for the change in s . s and Timer reporter concentration $[P]$ was calculated by applying Eq. 3 at steady state.

Eq. 5a

$$s = G \cdot k \frac{m_G + k}{m_G}$$

Eq. 5b

$$[P] = G \frac{m_G + k}{m_G}$$

G is the concentration of fluorescent sfGFP species inferred from sfGFP mean intensity.

It showed that the change in k could not completely compensate for the change in s as the fold change of s was always greater (Fig. 3i). Both fold change of K_{deg} and K_{dil} were less than that of s , although K_{dil} seemed to be more adaptive than K_{deg} (Fig. 3k, l). As a result, the concentration of short-lived Timer decreased following the reduction of synthesis rate. Nevertheless, the fold change of the protein concentration $[P]$ was significantly less than s (Fig. 3j), demonstrating the buffering effect of the coordination between protein turnover and protein synthesis on the cellular protein concentration.

To determine if the Timer's G/R ratio could be taken as a proxy for protein turnover, G/R ratios were calculated from Timer fluorescent measurements across different CHX treatments. As expected, the G/R ratio had a good correlation with k (Fig. 3h). The correlation was near linear (Fig. 3h). This was because m_G was estimated to be at least 50 times bigger than m_R (Alber et al., 2018; Guerra et al., 2022; Khmelinskii et al., 2016, 2012), when k was smaller (below 5 h^{-1}) than m_G , the relation between G/R ratio and k would be in the linear range. Notably, K_{deg} and K_{dil} had a linear relation (Fig. 3g), which allowed us to infer the relative change in K_{deg} or K_{dil} from the G/R ratio directly (Fig. S2d).

Taken together, these results suggest that protein degradation and dilution can adapt to the change in protein synthesis. Since the short-lived Timer is degraded directly by the proteasome, the change in degradation rate indicates a change in proteasome activity, which affects the degradation rates globally. The result of the coordination between protein synthesis and degradation is the buffering effect on the Timer reporter's concentration. However, a such adaption from degradation and dilution cannot wholly compensate for the change of synthesis.

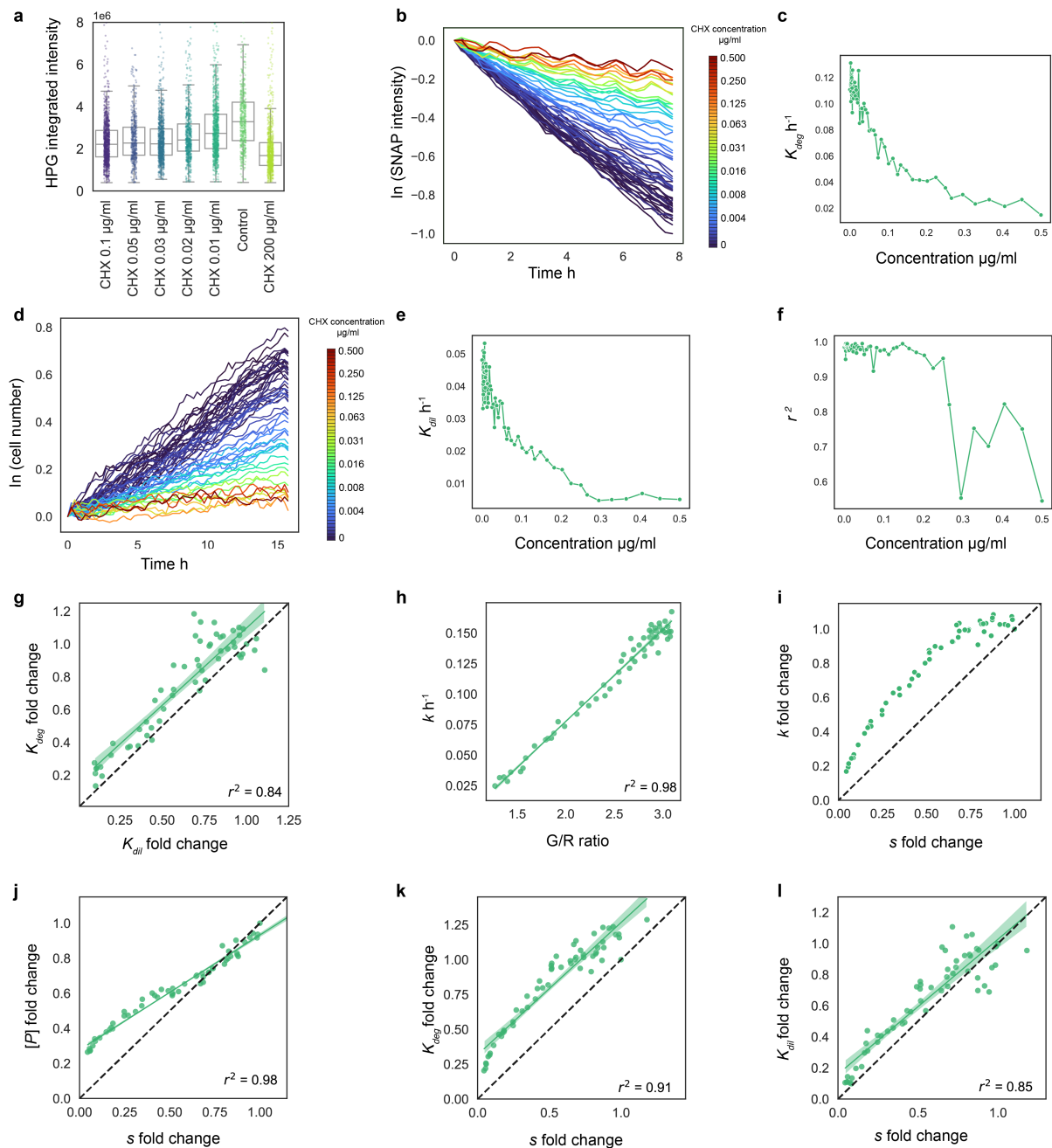


Figure 3 | Protein degradation adaption to prolonged CHX treatments.

a, HPG labelling of newly synthesised proteins after CHX prolonged treatment. The mean HPG intensity of each cell is plotted. CHX 200 $\mu\text{g/ml}$ was added to cells 30 min before and during HPG labelling as the negative control. **b**, SNAP pulse-chase labelling after prolonged CHX treatment. Traces are the sum of the intensity of all segmented nuclei per condition, normalized to the time point 0, then log-transformed. For **b** and **d**, the colourmap shows the CHX concentration for each condition. Each colour block represents a different concentration. Between indicated concentrations, drug concentration decreases by 10% from the previous one. **c**, Degradation rates across CHX concentration gradient after CHX prolonged treatments. Degradation rates were calculated by linear fitting of traces in Fig 3b. **d**, Cell number over time after CHX prolonged treatments. Cell number was calculated from segmented objects in the SNAP pulse-chase movie. Raw values were normalized to the time 0 and then log-transformed. **e**, K_{dil} across CHX concentration gradient. K_{dil} was measured by linear fitting of traces in Fig 3d. **f**, r^2 of exponential fitting of cell number over time for each CHX concentration (traces in Fig. 3d). Across all CHX prolonged treatment conditions, the correlation between **g**, fold change of K_{deg} (from Fig. 3c) and fold change of K_{dil} (from Fig. 3e); **h**, mean G/R ratio and total turnover rate k measured by SNAP pulse-chase; **i**, fold change of k and fold change of s ; **j**, fold change of Timer concentration $[P]$ and fold change of s ; **k**, fold change of K_{deg} (from Fig. 3c) and fold change of s ; **l**, fold change of K_{dil} (from Fig. 3e) and fold change of s . Shading: 95% CI (**g**, **h**, **j**, **k**, **l**). The Dash line is $y = x$ (**g**, **i**, **j**, **k**, **l**).

2.4. Downregulation of protein degradation following the treatment of an inhibitor of transcription factor Myc

c-Myc (or Myc) is a multi-function transcription factor that is involved in cell cycle control, transcription regulation, ribosome production, as well as differentiation, immune response and apoptosis (Amati et al., 1998; Das et al., 2022; Eisenman, 2001; Lourenco et al., 2021). It has been shown that Myc can act as a transcription amplifier that increases global transcription and protein synthesis (Elkon et al., 2015; Lin et al., 2012; Nie et al., 2020, 2020, 2012; Patange et al., 2022). A small molecule 10058-F4 (will be referred to as MYCi) is a potent inhibitor of transcription activity Myc protein by prohibiting the interaction between Myc and its coactivator Max, which is essential for the transactivation of Myc target genes (Yin et al., 2003). MYCi treatment has been shown to reduce global protein synthesis (Scognamiglio et al., 2016). In addition, a prolonged treatment by 64 μ M of MYCi in mouse embryonic stem cells (mESC) can arrest the cell cycle without visible toxicity or compromising the stem cell pluripotency (Scognamiglio et al., 2016). Although MYCi primarily acts on transcription, we reasoned that prolonged MYCi treatment should have a similar effect on protein synthesis as CHX. Moreover, inhibition of transcription by MYCi could have a delayed effect on protein synthesis compared to CHX, which provided a different dynamic for proteostasis adaption. The use of using more than one drug also minimised the possibility that any result was caused by the side effect of a particular drug.

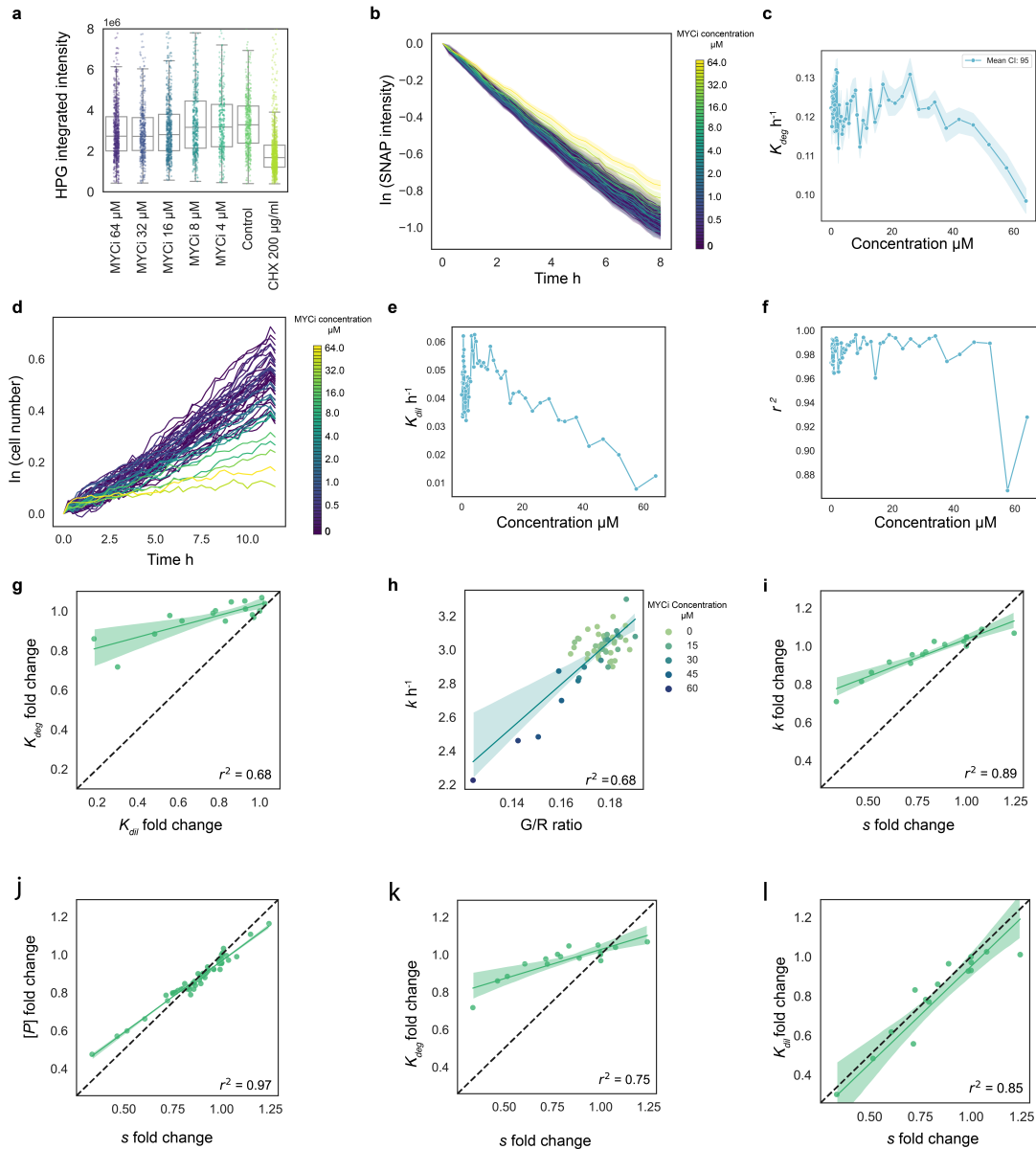


Figure 4 | Protein degradation adaption to prolonged MYCi treatment.

a, HPG labelling of newly synthesised proteins after MYCi prolonged treatment. The mean HPG intensity of each cell is plotted. CHX 200 $\mu\text{g/ml}$ was added to cells 30 min before and during HPG labelling as a negative control. **b**, SNAP pulse-chase labelling after prolonged MYCi treatments. Cell lineages were tracked, and the integrated nuclear intensity of daughter cells was summed within the lineage, normalized to time 0 then log-transformed. Means of per-lineage measurements per condition are plotted. Shading: 95% CI. For **b** and **d**, the colourmap shows MYCi concentration for each condition. Each colour block represents a different concentration. Between indicated concentrations, the drug concentration decreases by 10% from the previous one. **c**, Means of degradation rates across MYCi concentration gradient after MYCi prolonged treatments. Degradation rates were calculated by linear fitting of traces in Fig. 4b. Shading: 95% CI. **d**, Cell number over time after MYCi prolonged treatments. Cell number was calculated from segmented objects in SNAP pulse-chase movies. Raw values were normalized to time 0 then log was transformed. **e**, K_{dil} across MYCi concentration gradient. K_{dil} was measured by linear fitting of traces in Fig. 4d. **f**, r^2 of exponential fitting of cell number over time for each MYCi concentration (traces in Fig. 4e). Across all MYCi prolonged treatment conditions, the correlation between **g**, fold change of K_{deg} (from Fig. 4c) and fold change of K_{dil} for MYCi concentrations above 15 μM (from Fig. 4e); **h**, mean G/R ratio and total turnover rate k measured by SNAP pulse-chase; **i**, fold change of k and fold change of s for MYCi concentrations above 15 μM ; **j**, fold change of the Timer concentration $[P]$ and fold change of s ; **k**, fold change of K_{deg} (from Fig. 4c) and fold change of s for MYCi concentrations above 15 μM ; **l**, fold change of K_{dil} (from Fig. 4e) and fold change of s for MYCi concentrations above 15 μM . Shading: 95% CI (**g**, **h**, **j**, **k**, **l**). The dash line is $y = x$ (**g**, **i**, **j**, **k**, **l**).

To investigate if reduced protein synthesis by MYCi could result in the adaption of protein degradation, 56 different concentrations of MYCi were applied to 3T3 cells carrying short-lived Timer, ranging from 64 to 0.27 μM for 48 h. When measuring the protein synthesis rate by HPG after prolonged MYCi treatments, we found that at 64 μM MYCi, synthesis reduced about proximately 1.5-fold (Fig. 4a). We then measured protein degradation rate K_{deg} and turnover rate k by SNAP pulse-chase labelling. Although measurements of degradation rate were noisy at low MYCi concentrations, at high MYCi concentrations above 20 μM , protein degradation showed an apparent dose-dependent decrease (Fig. 4b, c), indicating the coordination between synthesis and degradation was present. We then measured the dilution rate K_{dil} , which showed a gradual reduction as the concentration of MYCi increased (Fig. 4d, e). MYCi did not induce quiescence in 3T3 cells when the same concentration used for mouse embryonic stem cells (mESC) in Scognamiglio et al., 2016 was applied. Instead, cells kept proliferating exponentially when MYCi concentration was below 55 μM , after which proliferation started to deviate slightly from the exponential function (Fig. 4f). Cell death throughout the treatment was minimal (inferred from the MYCi time-lapse movie, Fig. 8a). The noise in measured K_{deg} across MYCi conditions raised the question whether, at low MYCi concentration range, cells had reached the steady-state by the time of the measurements. To assess this, we checked the correlation between the k and G/R ratio, which should not be correlated when proteostasis deviated from the steady state. Although k and G/R ratios were generally correlated (Fig. 4h), the correlation was significantly worse compared to CHX treatments (Fig. 3h), which might explain the noise in the data.

To study the quantitative relation of the adaption of K_{deg} K_{dil} to protein synthesis s , we calculated s and $[P]$ using the steady-state Eq. 5. We then compared the fold change between K_{deg} , K_{dil} and s . Similar to CHX, the downregulation of k could not completely compensate for the effect of the protein synthesis inhibition by MYCi, as the fold change of s was greater than k (Fig. 4i). Consequently, the concentration of Timer was reduced after MYCi treatment. However, the buffering effect of k was still visible, resulting that the fold change of Timer concentration $[P]$ being less than s (Fig. 4j). Unlike CHX, folder change of K_{dil} was much more significant than that of K_{deg} (Fig. 4j, k, l), which might be explained by the direct effect of Myc inhibition on cell cycle progression. Overall, our results suggest that inhibition of protein synthesis through targeting transcription by MYCi leads to a similar compensatory effect from protein degradation and dilution to buffer the change in synthesis as observed in the CHX experiment.

2.5. The same fold changes in degradation and dilution rates to preserve the relative proteome composition during the CHX treatments

For dividing cells, each protein species has a shared global dilution rate, however distinct in their own degradation rates. The overall turnover rate of any protein j is governed by additive rather than multiplicative relations between K_{deg}^j for individual protein and a global K_{dil} .

Eq. 6

$$[P^j] = \frac{s^j}{K_{deg}^j + K_{dil}}$$

In Eq. 6, $[P^j]$ is the steady-state concentration of a specific protein species j , s^j and K_{deg}^j are the j protein-specific synthesis and degradation rates.

This means that during any changes in the proteostasis state if the fold change of concentration of each protein species is to be kept identical, in other words, the relative proteome composition is to be maintained, it is important for K_{deg}^j to have the same fold change as K_{dil} . There are contexts where K_{deg}^j acts independently from K_{dil} . For example, when cells exit the cell cycle, the fold change of K_{dil} is infinite. In such cases, the proteome composition is significantly rearranged, and additional mechanisms such as autophagy are employed by cells to tackle the imbalance of turnover rates across proteome (Zhang et al., 2017).

Interestingly, when 3T3 was treated with various CHX concentrations, the fold change of K_{deg} and K_{dil} were correlated linearly on the $y = x$ diagonal line (Fig. 3g), suggesting that cells coordinated the dilution and degradation rate to maintain the stoichiometry of proteins.

However, for prolonged treatments of MYCi, there was not enough variation for most of the data points to precisely calculate the slope. When fitted only the high MYCi concentration range (above 15 μ M), surprisingly, the slope deviated from 1, as K_{dil} had a bigger fold change than K_{deg} (Fig. 4g). This might be explained by the regulatory function of Myc on the cell cycle. We could not entirely exclude that if the MYCi treatment had lasted longer, K_{deg} might reach the exact fold change as K_{dil} .

2.6. Protein turnover dynamically adapts to the change of protein synthesis following CHX addition and CHX release

The evolution of synthesis and degradation rates over time during well-defined non-steady-states could provide not only the dynamics of their interaction but also the basis to study the mechanism of such coordination. The timescale and dynamics of the coordination between synthesis and degradation were investigated by applying CHX to create two different conditions in 3T3 cells (Fig. 5a):

1. CHX addition: Reduction of synthesis by adding 0.1 $\mu\text{g/ml}$ CHX at the time point 0.
2. CHX release: Synthesis recovery by pre-incubation cells with 0.1 $\mu\text{g/ml}$ CHX 0.1 for 48h, then wash-out CHX at the time point 0.

Subsequently, fluorescent time-lapse microscopy was performed to record sfGFP and mOrange2 intensities (Fig. 5b), which would then be used to solve the synthesis and degradation rates over time through superstatistical modelling with Eq. 3. We pooled fluorescence intensity measurements from hundreds to thousands of cells per condition at each time frame to create fluorescence trajectories of the ‘average cell’. The same experiment was performed for both the short-lived Timer (Fig. 5c) and the long-lived Timer (Fig. 5d). Modelling from Timer could only yield s and k . To obtain dynamics of K_{deg} , the evolution of K_{dil} over time needed to be modelled from the cell number accumulation curve (Fig. 5f, g) with the same superstatistical modelling method, as it would be unrealistic to assume that K_{dil} followed simple dynamics during the course of the movies.

For short-lived Timer, sfGFP, mOrange2, and G/R ratio showed distinctive changes between CHX release and CHX addition (Fig. 5c). For CHX addition, both sfGFP, mOrange2 signals and G/R ratio, after an initial decrease, stabilised after 20 h below the control level, indicating a reduction in protein turnover rate k when cells reached the steady-state after 20 h of CHX addition (Fig. 5c) (Eq. 4). The stabilised G/R ratio from CHX addition was lower than the CHX prolonged treated cells, which was unexpected (Fig. 5c). It could be arising from either the inaccuracy in estimating mOrange2 channel background level or cells adopted a slightly different and probably temporal steady-state. Nevertheless, this discrepancy should not affect the result of modelling since we were interested primarily in dynamics rather than absolute values of the synthesis and degradation rates. It was important to note that a factor of 2 should be multiplied by the G/R ratio in order to be comparable with values from the Table. 1, as α was different for both experiments resulting from unique microscopic exposure settings.

For CHX release, the sfGFP and mOrange2 intensities, as well as the G/R ratio, increased rapidly after CHX wash-out before stabilising around the control level after about 20 h (Fig. 5c). This suggested that the CHX-induced proteostasis state is reversible, as the Timer protein concentration could recover to control level once the drug was released. The fact that the G/R ratio eventually stabilised higher than

the control level after 12 h of drug release implied the resurgence of protein turnover rate k following

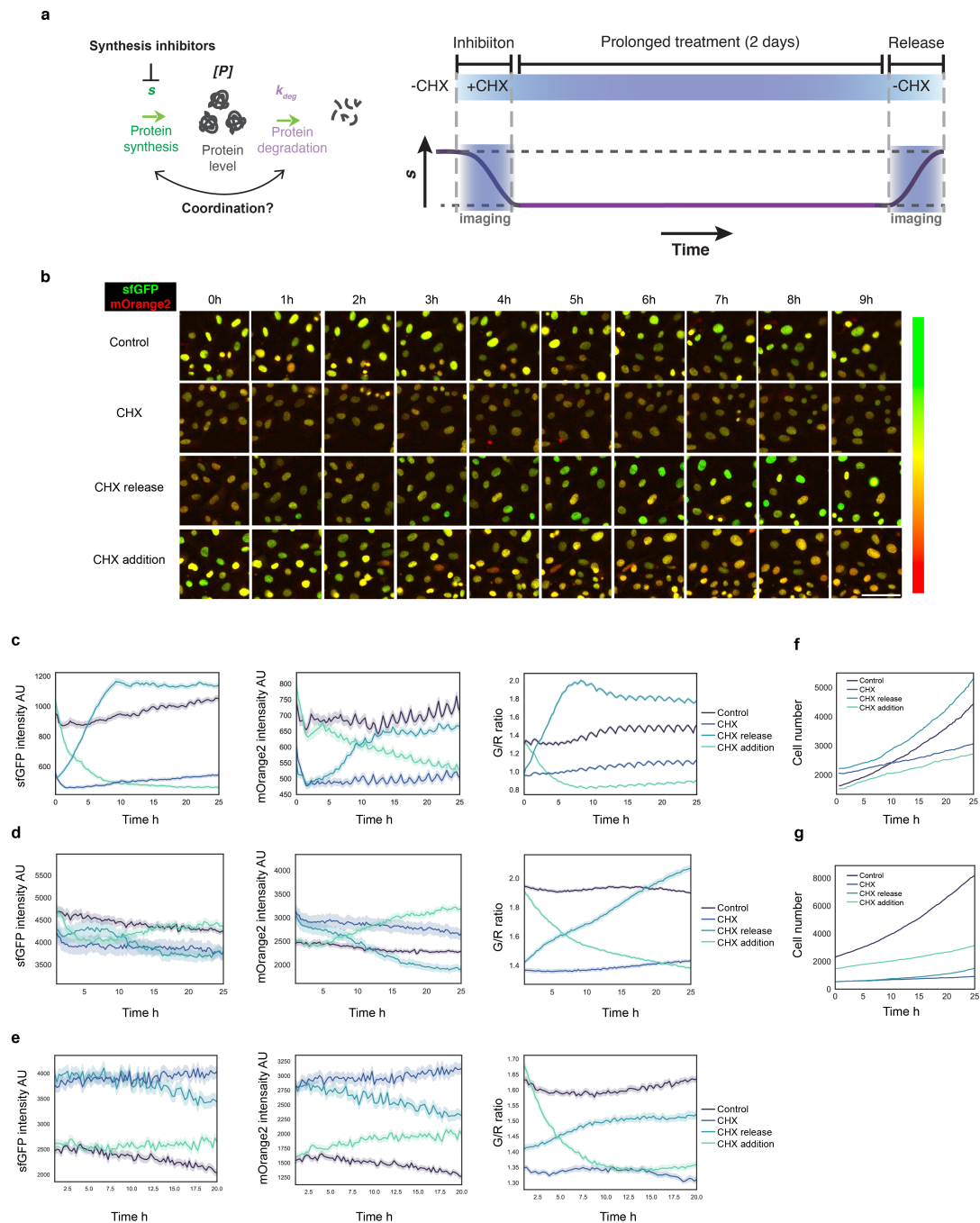


Figure 5 | Dynamics of synthesis and degradation during CHX and CHX release treatment.

a, Scheme of experimental design for creating dynamic proteostasis contexts by CHX addition or CHX release after prolonged treatment. **b**, Still images of time-lapse microscopy of 3T3 cells expressing short-lived Timer, shown as composite images. For the CHX release and CHX addition, the drug was added or washed out at 0 h. The colourmap indicates the theoretical colour range resulting from different sfGFP and mOrange intensity ratios, which should not be taken quantitatively. Scale bar: 100 μ m. Traces of sfGFP, mOrange mean intensities and the G/R ratio when applying different CHX conditions for **c**, short-lived Timer, **d**, long-lived Timer, and **e**, long-lived Timer in confluent cell culture. Cell number over time across CHX conditions for **f**, short-lived Timer (as in Fig. 5c), and **g**, long-lived Timer (as in Fig. 5d). For **c**, **d**, and **e**, means of all segmented cells per condition are plotted. Shading: 95% CI (**c**, **d**, **e**). For **c**, **d**, and **e**, more than 400 cells for each condition were analysed at time point 0. For **e**, cells reached confluency 2 days before the imaging. 20:1 ratio between WT and Timer cells was kept at the beginning of the cell culture. Traces are trimmed between 1 h and 20 h to exclude artefacts at the beginning and the end of the movie.

the recovery in protein synthesis (Fig. 5c). Again, we expected the G/R ratio from CHX release to be the same as control. However, experimental data showed eventual G/R ratio is high than the control (Fig. 5c), which could either be due to an error in background estimation or cells adapting a different, probably temporal steady state than the control (Fig. 5c).

The same experiment was performed for the long-lived Timer to sample the dynamics of the part of the proteome with lower degradation rates and exclude the promoter-specific effect that CHX treatments might produce. For the long-lived Timer, the sfGFP signal was less dynamic than mOrange2, which was the opposite from the short-lived Timer (Fig. 5d). Interestingly, the G/R ratio was higher for the control compared to CHX, implying the control cells had higher protein turnover rate k (Fig. 5d). Notably, the CHX condition had lower sfGFP intensity but higher mOrange2 intensity compared to the control (Fig. 5d). In contrast, for short-live Timer, both sfGFP and mOrange2 intensities were lower comparing the control (Fig. 5c). From this coincidence, we can estimate that between the CHX and the control cells, the fold change of k was slightly less than the fold change of s , but the two values were extremely close (Eq. 7).

Eq. 7

$$\frac{k_{control}}{k_{CHX}} < \frac{s_{control}}{s_{CHX}} < \frac{k_{control}}{k_{CHX}} \left(\frac{1 + \frac{k_{control}}{m_R}}{1 + \frac{k_{CHX}}{m_R}} \right)$$

$$\frac{k_{control}}{m_R} \approx 0.8$$

For the CHX addition, sfGFP traces showed relatively minor changes, while mOrange2 intensity increased after a delay of 5 h, indicating the downregulation of k following the change in s . For CHX release, the change of sfGFP intensity was again relative insignificant, whereas mOrange2 intensity started to decrease within 5h, implying the upregulation of k (Fig. 5d).

From the Timer fluorescence traces alone, we can already conclude that k changes accordantly with the change of s for both the short-lived and the long-lived Timer within a few hours following the CHX addition and release.

2.7. Dynamics of synthesis, degradation, and dilution rates during CHX addition or release

To infer changes in protein synthesis and turnover rates over time for the short-lived Timer following the increase or decrease of protein synthesis rates caused by CHX addition or release, short-lived Timer traces (from Fig. 5c) were modelled by the superstatistical modelling. To avoid the imaging artefact interfering with the modelling, Timer traces were smoothed, and the first 2 h of the movies was trimmed (Fig. S4). The modelling result showed that following the addition of CHX, s reduced and stabilised within 2 h. At the same time, a significant delay in the down-regulation of k was observed, which decreased gradually during the first 10 h before stabilising (Fig. 6a). For CHX release, s was up-regulated within 2 h. In contrast, k was up-regulated progressively with a similar 10 h delay (Fig. 6b). Data retrodiction showed that for CHX release, the retrodicted Timer traces from s and k overlapped very well with the empirical data (Fig. S5a), there is a slight disagreement between the two for CHX addition (Fig. S5b), suggesting some hyperparameters for modelling could still be optimised.

To calculate the time variation in K_{deg} , the change of K_{dil} over time needed to be modelled from the cell accumulation curves (Fig. 5f) through a time-evolving exponential function, then subtracted from k . The values of K_{dil} obtained from modelling recapitulated the values obtained from the single exponential fitting for CHX and control at the steady-state (Table.1) (Fig. 6c). The dynamics of K_{deg} were noisy as the errors propagated from the successive modelling of both k and K_{dil} (Fig. 6d, e). Nevertheless, we recovered the overall dynamics of K_{deg} . K_{deg} displayed similar dynamics with k . For the CHX addition condition, K_{deg} showed a 2-fold decrease for the first 10 h (Fig. 6d). For the CHX release condition, K_{deg} increased near 2-fold during the first 12 h before reaching near equilibrium (Fig. 6e). Dynamics of K_{deg} in both CHX addition and release suggest that K_{deg} adapts and compensates to the change in synthesis within a period of about 10 h. Overall, we have demonstrated that our modelling can retrieve the dynamics of protein synthesis, degradation and dilution from fluorescence traces of Timer at the non-equilibrium scenarios. Furthermore, we observed a persistent 10 h delay in both protein turnover and degradation rates to reach the equilibrium level when adapting to rapid changes in protein synthesis.

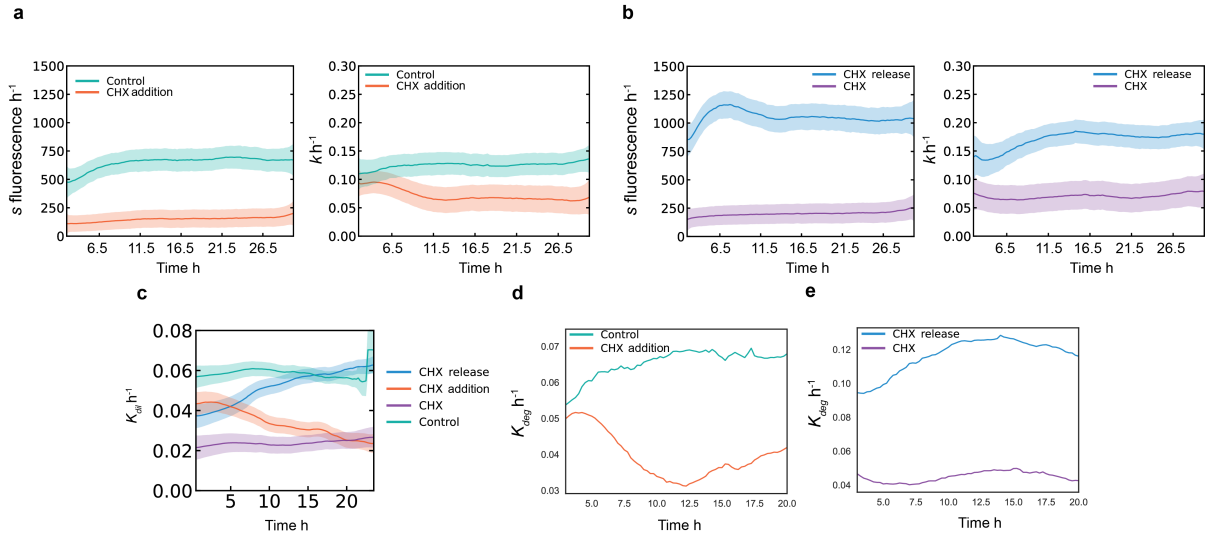


Figure 6 | Calculation of protein synthesis and degradation dynamics for CHX conditions.

a, b, s and k calculated from superstatistical modelling of short-lived Timer traces for CHX treatments (Fig. 5c). First 1.5 h of traces were trimmed before modelling to exclude imaging artefacts. The mean of the posterior distribution was plotted. Conditions are grouped between Control/CHX addition and CHX/CHX release as their s and k started at the same point at time point 0. **c**, K_{dil} evolution over time for short-lived Timer under different CHX treatments, calculated from superstatistical modelling of Fig. 5f. First two data points (first 15 min) were trimmed. **d, e**, K_{deg} calculated by subtracting K_{dil} (Fig. 6c) from k (Fig. 6a, b). The first 3 h is trimmed to exclude imaging artefacts. Shading for **a, b, c**: std of the posterior distribution.

2.8. Validation of modelled degradation rate by SNAP pulse-chase labelling

To validate the degradation rate dynamics calculated by the superstatistical modelling, we performed a SNAP pulse-chase labelling to obtain independent measurements of degradation rates at different time points after the washout of CHX. Since an exponential fitting could only give one K_{deg} from the entire duration of the SNAP chase movie, whereas K_{deg} was constantly changing over time, a simple assumption was made that K_{deg} evolved linearly over time so that K_{deg} measured by SNAP corresponded to the time point at the middle of the chase phase. For example, K_{deg} at 5 h of CHX release was calculated from the traces that started 1h after CHX release and finished at 9 h after CHX release. The result showed that K_{deg} started to increase between 5h to 7h after CHX release and stabilised at the control level 9 h - 11 h after CHX release (Fig. 7a, S6a). This agreed with the K_{deg} dynamics calculated from the Timer (Fig. 6e). Dilution rates measured from nucleus growth rates showed that K_{dil} was recovered within 5h after CHX release. However, the data were too noisy to infer the real dynamics (Fig. 7d, S6d).

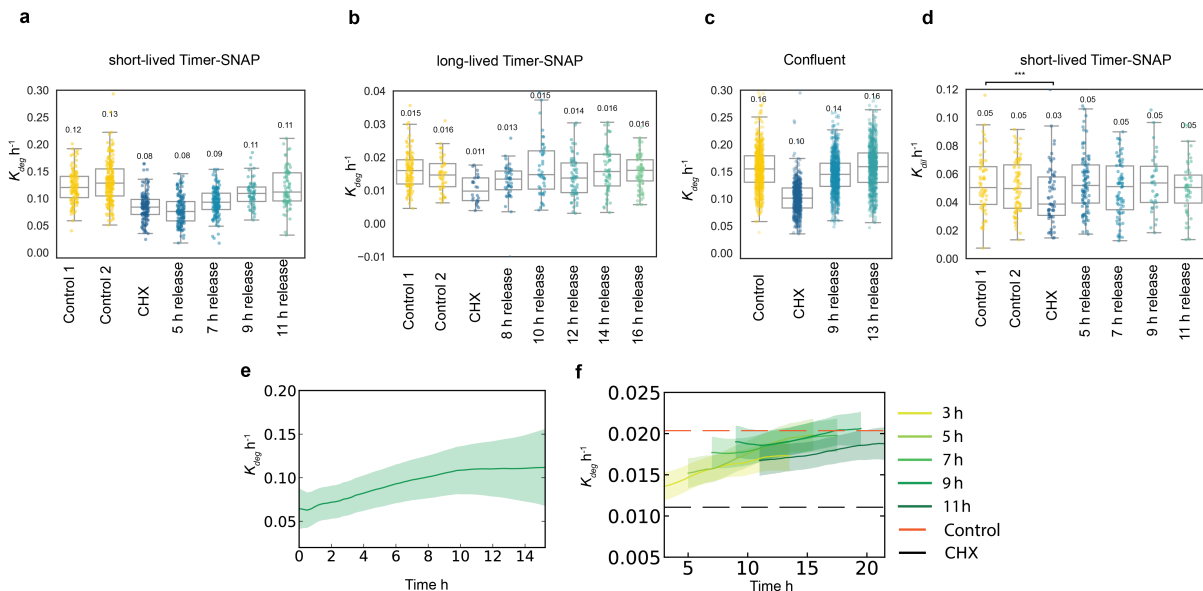


Figure 7 | Validation of degradation dynamics during CHX release.

The protein degradation rate measured by SNAP pulse-chase labelling at different time points after CHX release by **a**, short-lived Timer (traces from Fig. S6a, Table. 3), **b**, long-lived Timer (traces from Fig. S6b, Table. 4), **c**, short-lived Timer in confluent culture (traces from Fig. S6c). For **a**, **b**, **c**, the movie started at different time points proceeding with the alleviation of CHX. Single lineage traces were exponentially fitted. The time after the CHX release labelled in the x-axis is the pseudo-time calculated by adding half of the length of the SNAP chase phase to the time passed after the CHX release at the start of the SNAP chase. For **c**, cells reached confluency two days before imaging, and a 20:1 ratio between WT and Timer cells was seeded at the beginning of cell culture. **d**, K_{dil} of short-lived Timer measured by the fitting of nucleus area growth from single lineage traces. The test statistic: T-test, where*** signifies $p \leq 0.001$. Fitted values were filtered by $r^2 > 0.5$ (**b**, **d**). The Median is shown on top of the box plot (**a**, **b**, **c**, **d**). **e**, Time evolution of K_{deg} calculated from the superstatistical modelling of SNAP traces of the short-lived Timer after CHX release (Fig. S6a). Traces from different time points were overlaid to create a meta-trajectory. **f**, Superstatistical modelling of long-lived Timer after CHX release (Fig. S6b). Times in the figure legend represent the time after the CHX washout when the SNAP-chase movie started. Dash lines are the mean K_{deg} modelled from CHX and control traces (Fig. S6b). For **a**, **b**, and **d**, Control 1 and Control 2 were cells cultured in different densities (Control 1: about 80% confluency at the start of the movie. Control 2: 40% to 60% confluency). For **e**, **f**, CHX was washed out at time point 0. Shading for **e**, **f**: std of the posterior.

To examine whether the degradation of long-lived proteins followed the same dynamics, the same pulse-chase experiment was also performed for 3T3 cells carrying the long-lived Timer. Despite significant differences in half-lives between short-lived and long-lived Timer, the same degradation dynamics following CHX alleviation were retrieved (Fig. 7b, S6b).

To overcome the drawback of using a single exponential fitting to calculate the time-varying K_{deg} , we decided to employ the same superstatistical modelling method applied for cell number accumulation curves to resolve the time-dependent change of K_{deg} from SNAP traces. SNAP movies that started at the different time points of the CHX release were pooled to create an extended SNAP meta-trajectory from 0 h to 15 h after the CHX release. This trace was then modelled by a time-evolving exponential decay function. The result revealed a continuous and gradual increase of K_{deg} from within 1 h after CHX release till 10 h, after which it stabilised at the expected value around 0.11 h^{-1} (Fig. 7e, S6e). We then applied the same method for the long-lived Timer SNAP traces. Although hampered by less optimal fitting, we still recovered the same dynamics of K_{deg} as the short-lived Timer (Fig. 7f). These results reaffirm the accuracy of our superstatistical modelling of the sfGFP and mOrange2 traces. At the same time, we are able to confirm that the change in proteasomal degradation following the increase in protein synthesis affects the degradation rates in the same manner for both short-lived and long-lived proteins.

2.9. Protein degradation adaption to protein synthesis in non-dividing cells

For quiescent cells, the only source of sustained protein removal is degradation. The consequence of an imbalance between protein synthesis and degradation would be more severe as the flexibility provided by dilution does not exist. To examine the dynamics of coordination between synthesis and degradation in quiescent cells, confluent 3T3 cell culture was used. We measured the protein degradation rate using SNAP pulse-chase labelling for cells at different time points following CHX release from a 48 h prolonged treatment. The result showed that the degradation rate was down-regulated after CHX prolonged treatment. However, within 9 h after CHX release, the degradation rate was recovered to the control level (Fig. 7c), suggesting that coordination between synthesis and degradation exists in non-dividing cells.

To investigate the dynamics of synthesis and degradation rate during a CHX-induced non-steady state, Timer fluorescence microscopy was performed. As confluent cells were sensitive to phototoxicity, the long-lived Timer was used so that exposure time could be significantly reduced. To segment single cells and accurately estimate the fluorescence background, we mixed cells carrying Timer with wild-type (WT) cells in the culture so that Timer-carrying cells were spaced out by non-fluorescence cells when the culture became confluent. Surprisingly, we found CHX prolonged treated cells had high sfGFP and mOrange2 intensity compared to the control (Fig. 5e), suggesting down-regulation of K_{deg} overcompensated the change in s induced by CHX, resulting in higher protein level $[P]$ in the condition where the synthesis rate was lower. The G/R ratio in CHX-treated cells was lower than the control, suggesting that K_{deg} was indeed down-regulated with s (Fig. 5e). When CHX was added, rather curiously, both sfGFP and mOrange2 started to increase around 2 h and 6 h respectively after CHX addition (Fig. 5e), strongly suggesting that K_{deg} overcompensated change in s as soon as s was altered. The G/R ratio decreased over time after CHX was added, and eventually reached the steady state at CHX treated cells, indicating K_{deg} was down-regulated with CHX addition (Fig. 5e). Equally surprising was when CHX was released from prolonged treatment, sfGFP and mOrange2 intensity decreased over time, suggesting K_{deg} upregulated immediately after the recovery of s and overcompensated s (Fig. 5e). The G/R ratio increased after the CHX release compared to the CHX, suggesting K_{deg} was upregulated, though it did not recover to the control level (Fig. 5e). For both CHX release and CHX addition, G/R ratio reached the equilibrium after 10 h of the movie (Fig. 5e), which was significantly faster for long-lived Timer comparing to dividing cells where G/R never reached the equilibrium during 30 h of imaging (Fig. 5d). This strongly argues in non-dividing cells, the coordination between s and K_{deg} happens in a much shorter time window, which is consistent with the perception that non-dividing cells are forced to control protein level much stringently than dividing cells.

2.10. Protein degradation dynamically adapts to the change of protein synthesis following MYCi addition and MYCi release

Like CHX, MYCi is also a reversible inhibitor. Adding or washing out MYCi after prolonged treatment should cause protein synthesis to increase or decrease respectively. We expected MYCi would have a delayed effect on protein synthesis as it acted on transcription rather than translation. To investigate the dynamics of protein degradation adaption to the change of synthesis rate caused by MYCi, time-lapse fluorescent microscopy was performed for 3T3 cells carrying the short-lived Timer (Fig. 8a). At the start of the movie, 64 μ M MYCi was either added (MYCi addition) or washed out (MYCi release) after a 48 h prolonged treatment. The fluorescence traces showed that after the MYCi addition, sfGFP and mOrange2 concentration decreased over time as expected (Fig. 8b). The changes were less rapid compared with the CHX addition, reflecting the relative indirect effect of MYCi on protein synthesis. From the G/R ratio, which stabilised after 15 h near the level of MYCi treated cells, a 1.75-fold reduction of protein turnover rate could be inferred (Fig. 8b). Although rather unexpectedly, the G/R ratio of MYCi addition was lower than the prolonged MYCi treated cells (Fig. 8b).

For MYCi release, a similar profile of sfGFP and mOrange2 was observed as CHX release, except the recovery of both intensity and G/R ratio were slower compared to CHX release (Fig. 8b). Stabilisation of the G/R ratio near the control level after 10 h of MYCi release indicated the recovery of k following the bounce back of proteins synthesis (Fig. 8b).

We then modelled the short-lived Timer traces by Eq. 3 to calculate the dynamics of k and s (Fig. 8b). To avoid imaging artefacts at the beginning of the movie, Timer traces were smoothed, and the first hour was trimmed (Fig. S4). The modelling result showed that following the addition of MYCi, it took 6h for s to reduce by more than 2-fold (Fig. 8d). The inference of k was noisy; nevertheless, a gradual decrease during the first 15 h could be observed (Fig. 8d). For the MYCi release, s was progressive upregulated during the first 16 h, which was expected as the relative indirectness of MYCi affecting protein synthesis (Fig. 8e). Meanwhile, k gradually increased for the first 12 h before reaching equilibrium, demonstrating the coordination between k and s (Fig. 8e).

In order to obtain the dynamics of K_{deg} , we then modelled the time evolution of K_{dil} from the cell accumulation curves (Fig. 8c) by the superstatistical modelling (Fig. 8f), which were to be deducted from the k to get K_{deg} . K_{dil} from MYCi prolonged treated cells showed mild variation over time (Fig. 8f), suggesting cells were not in absolute steady-state, which could explain the decrease of G/R ratio for MYCi condition at the beginning of the movie (Fig. 8b). The dynamics of K_{deg} showed trends similar to CHX, as it adapted to both decrease and increase of synthesis with a delay (Fig. 8g, h, S7a, b). We

conclude that the time scale and the dynamics of K_{deg} adaption to s are largely similar between CHX and MYCi despite the differences in their drug induce dynamics of s .

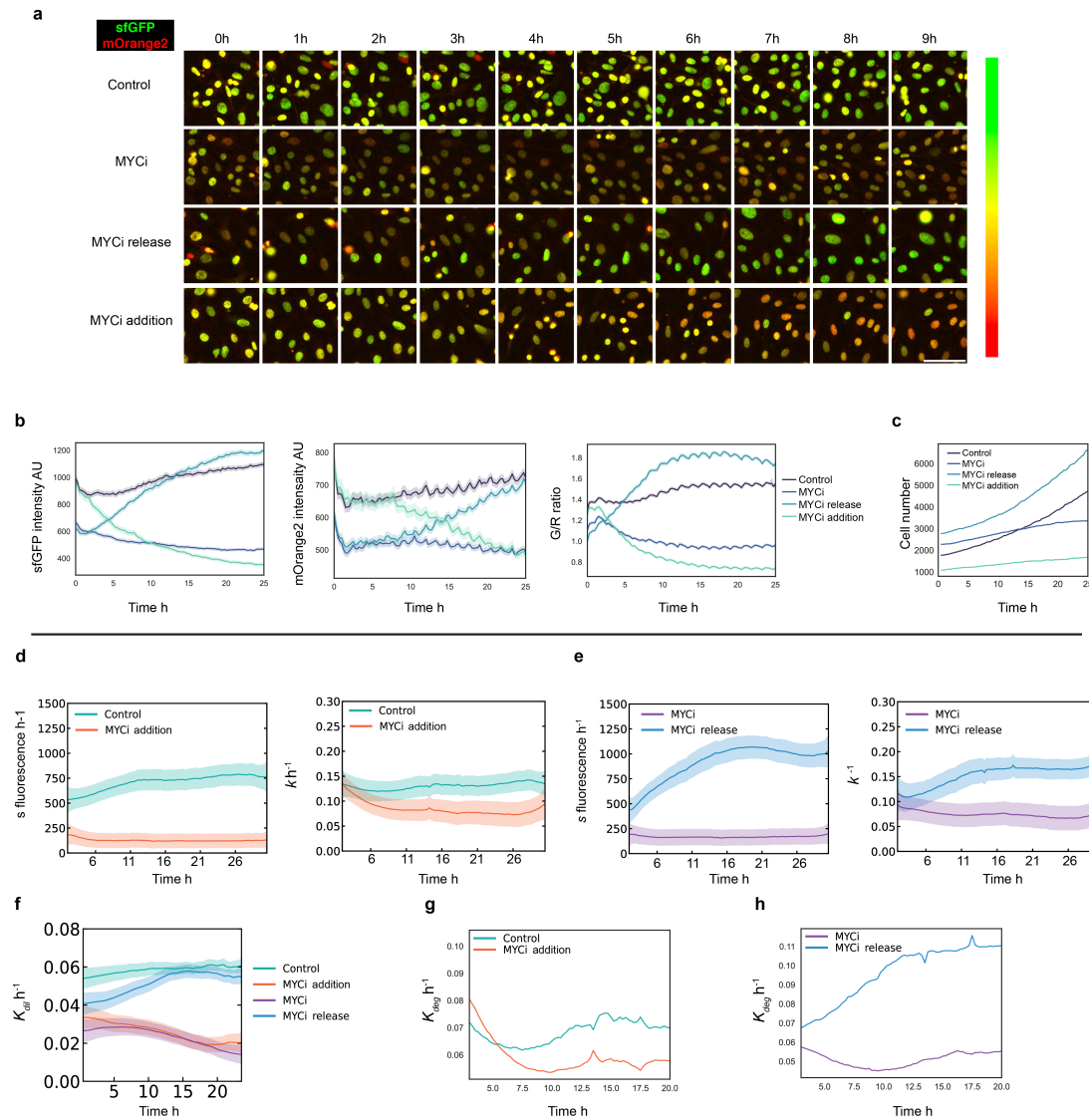


Figure 8 | Dynamics of synthesis and degradation during MYCi and MYCi release treatment.

a, Still images of time-lapse imaging of 3T3 cells expressing nuclear short-lived Timer, shown as composite images. For the MYCi release and the MYCi addition, the drug was added or washed out at 0 h. The colourmap indicates the theoretical colour range resulting from different sfGFP and mOrange intensity ratios and should not be taken quantitatively. Scale bar: 100 μm . **b**, Traces of sfGFP, mOrange mean intensity and G/R ratio. The mean of all segmented cells per frame per condition is plotted. Shading: 95% CI. Cell number per condition >1000 at time point 0. **c**, Cell number over time for different MYCi conditions. **d**, **e**, s and k calculated from superstatistical modelling of short-lived Timer traces for MYCi treatments (Fig. 8b). First 1 h of traces were trimmed before modelling to exclude imaging artefacts. The mean of the posterior distribution was plotted. Conditions are grouped between Control/MYCi addition and MYCi/MYCi release as their s and k started at the same point at time point 0. **f**, K_{dil} evolution over time for short-lived Timer under different MYCi treatments, calculated from the superstatistical modelling of Fig. 8c. First two data points (first 15 min) were trimmed. **g**, **h**, K_{deg} calculated by subtracting K_{dil} (Fig. 8f) from k (Fig. 8b, e). The first 3 h was trimmed to exclude imaging artefacts. Shading for **d**, **e**, **f**: std of the posterior distribution.

2.11. Transcription regulation during CHX release

The several-hour lag between the change of synthesis and adaption of degradation raised the possibility that coordination between synthesis and degradation was regulated transcriptionally. To investigate this conjecture, RNA-seq was performed for 3T3 cells taken during recovery from CHX release. Samples were treated with CHX for 48 h before washing out of the drug. Then RNAs from cells collected at 4 h, 6 h and 8 h after CHX release were extracted for the RNA-seq in order to recapitulate gene expression dynamics during CHX release.

PCA analysis showed that different treatment groups were ordered by the time taken after CHX release on the PC2 axis, as 8 h-release samples were closer to the control while 4 h-release samples were closer to CHX (Fig. 9a). This indicated that there were consecutive transcriptional changes for cells recovering from CHX. The correlation of the gene expression between conditions also indicated that the global gene expression was progressively changed following CHX release (Fig. S8e).

We reasoned that genes regulating the protein degradation recovery would upregulate once cells were released from CHX. To identify these genes, reads across samples were clustered according to their dynamics during CHX release (Fig. S8a, b). From these clusters, two groups of genes were selected for further analysis: in cluster 1 and cluster 10 were genes that had low expression levels in CHX but upregulated once CHX was released, while in cluster 5 were genes that had similar expression between CHX and Control but expression surged 4 h after CHX release (Fig. 9b, c). We named genes in cluster 1 and cluster 10 ‘revival genes’ and genes in cluster 5 ‘induced genes’. Encouragingly, genes contributing the most variance on PC 2 also had expression profiler matching either ‘revival genes’ or ‘induced genes’ (Fig. S8c). Moreover, many of these genes overlapped with genes in selected clusters (cluster 1, 5, 10) when they were filtered by 0.5 log₂ fold change between CHX and Control (Fig. S8d). Thus, we only focused on analysing ‘revival genes’ and ‘induced genes’ groups.

To characterise the functions of ‘revival genes’ and ‘induced genes’, an over-representation analysis was performed on gene sets from the Enrichr (Chen et al., 2013; Kuleshov et al., 2016; Xie et al., 2021). It was found that genes related to the proteasome, P53 pathway, autophagy, ubiquitin ligases and mTORC1 targets were over-represented among the ‘revival genes’ (Fig. 9d). In contrast, genes related to the ribosome, oxidative phosphorylation pathway and protein ER process pathway were over-represented among the ‘induced genes’ (Fig. 9d). Furthermore, ‘induced genes’ were also enriched with genes that were upregulated when treated with the proteasome inhibitor bortezomib or knockdown of proteasome subunits PSMD13 (Fig. S11), suggesting shared mechanisms between the cellular response to proteasome inhibition and the degradation adaption to the increase in protein synthesis.

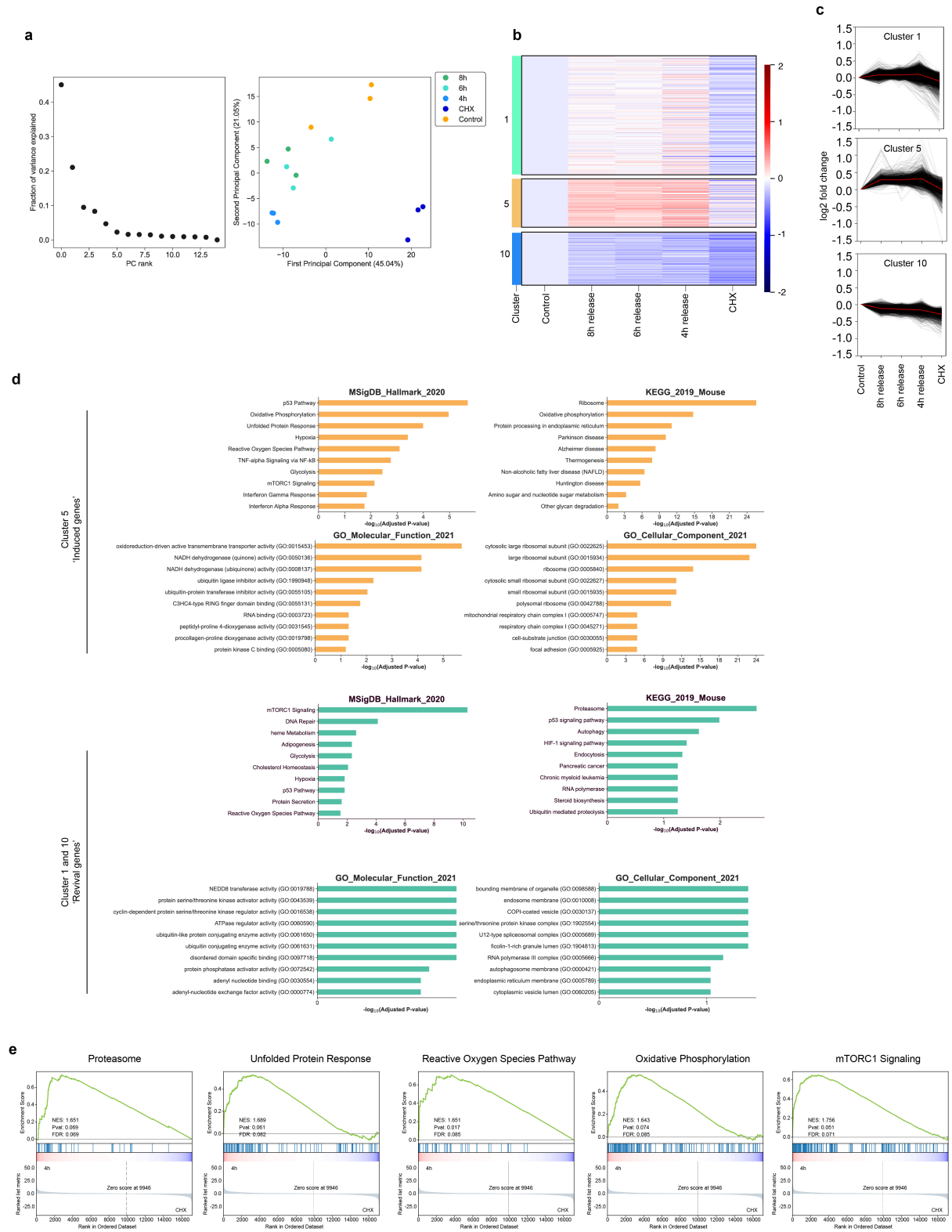


Figure 9 | Transcriptional regulation of proteostasis during the CHX release.

a, PCA of RNA-seq samples taken at indicated hours after the alleviation from prolonged CHX treatment. **b**, Heatmap of genes clustered according their expression dynamics after CHX release. Cluster 1,5,10 are displayed from Fig. S8a. Log₂ fold change of each gene was normalized to Control. **c**, Log₂ fold change (to Control) of genes across different time points after CHX release in cluster 1,5, and 10 (from Fig. 9b). Red line is the mean for each condition. **d**, Over-representation assay for cluster 1,10 and cluster 5, respectively, (Fig. S10) with corresponding Enrichr gene sets. FDR cut-off for plotting: 0.05. **e**, GSEA for selected gene sets between 4 h after CHX release and the CHX. Means of replicates per condition were used for the calculation of **b**, **c**, and **d**.

We wanted to reassess the result from over-representation analysis with Gene Set Enrichment Analysis (GSEA) (Subramanian et al., 2005), which is a more unbiased method as it considers the expression level of all genes across replicates. As we observed that most gene expression changes for selected clusters happened between the CHX and 4 h after release, we performed the GSEA comparing these two conditions for proteasomal genes, unfolded protein response targets, ROS pathway, oxidative phosphorylation genes and mTORC1 targets. Interestingly, all these genes were enriched in the 4 h sample, suggesting the up-regulation of these pathways after CHX release.

Next, we investigated the expression profile of individual genes from these pathways of interest. mTORC1 target genes were among the most over-represented pathways in the ‘revival genes’ group. Most target genes of the mTORC1 pathway were down-regulated in CHX-treated cells but recovered to the control level after 4 h of CHX release (Fig. 10a). Many of these genes were involved in the cholesterol pathway, glycolysis, amino acid metabolism and proteasome (Fig. S9a, b). Proteasomal

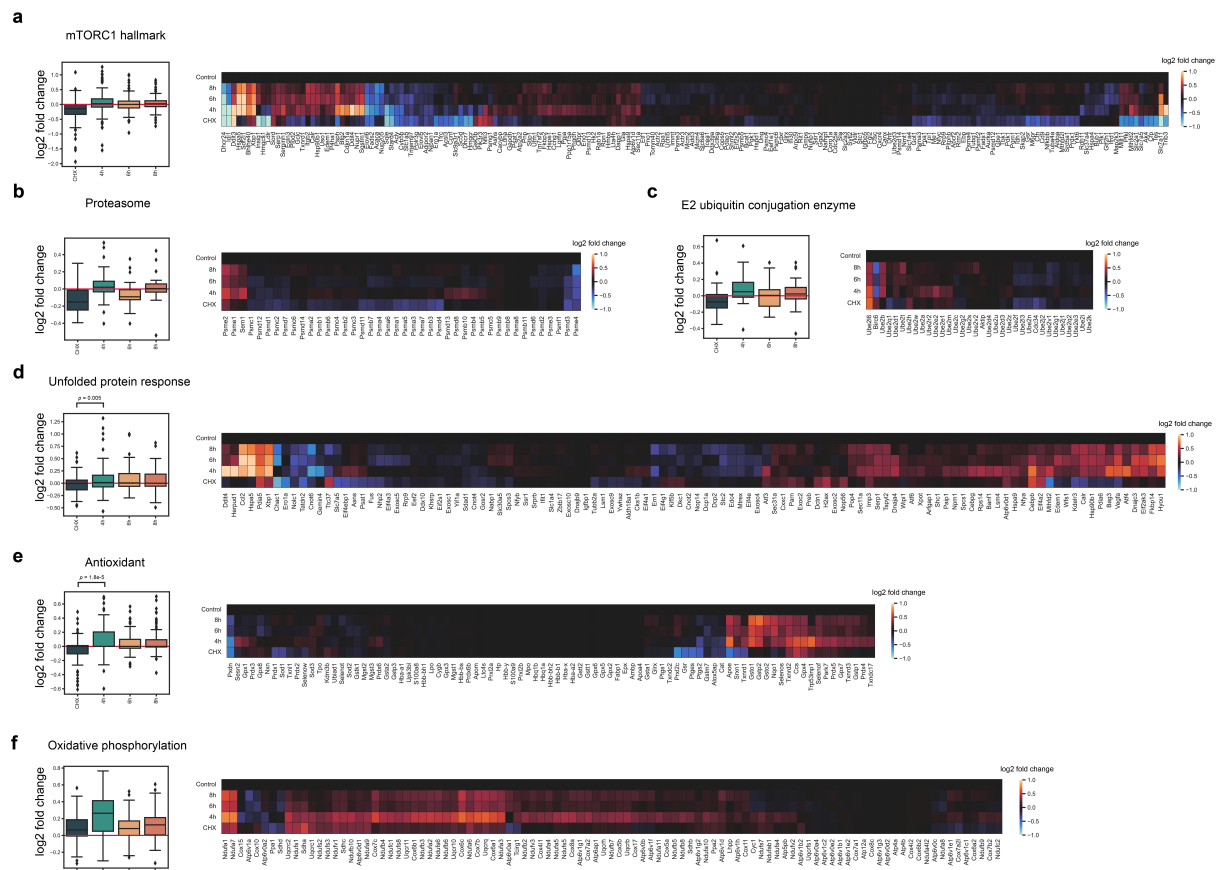


Figure 10 | Dynamics of pathways during the CHX release.

The expression profile of **a**, mTORC1 targets, **b**, the proteasomal subunits, **c**, E2 ubiquitin conjugation enzymes, **d**, Unfolded protein response pathway, **e**, Antioxidant genes, and **f**, genes participating in the mitochondria oxidative phosphorylation. Log₂ fold change of all genes are normalized to the control. Red line in the boxplot is the expression level of the control. The heatmaps indicate relative expression level of individual genes from the group across conditions. Genes in the heatmap are clustered by *hierarchical clustering* based on their expression profiles. The test statistic for **d** and **e**: T-test. Means of replicates per condition were used for the calculation of all figures. Hours labelled for conditions indicate the time after CHX release.

genes exhibited uniform dynamics as the expression of most of the CP and RP subunits were downregulated with CHX treatment but resurged to the control level 4 h after CHX release, whereas after 4 h, the expression level mostly remained stable (Fig. 10b). However, fold changes of expression among different conditions were rather mild for all subunits (Fig. 10b). E2 ubiquitin conjugation enzymes also showed similar dynamics as the proteasome, though again, the fold changes were rather mild (Fig. 10c). Interesting, expression of many genes involved in UPR and oxidative stress response were expressed at the same level between the control and CHX-treated cells, but highly were upregulated 4 h after CHX release (Fig. 10d, e, S10a). The dynamics of UPR genes were exemplified by genes regulated ERAD such as Herpud1 Syvn1 (Fig. 10d, S9c, d, S10a), ER Hsp 70 chaperons (Fig. 10d, S9d, S10a), and ATF4 targets (Fig. S9c). For antioxidant genes, Nrf2 targets such as the antioxidant glutathione (GSH) pathway were also upregulated within 4 h of CHX release (Fig. 10e). This observation indicated the activation of stress sensing mechanisms, which would limit the dynamic range of protein synthesis, forming a protein synthesis self-regulation negative feedback loop. As aforementioned, genes involved in mitochondrial oxidative phosphorylation were enriched among the 'induced genes'. A closer examination revealed that genes encoding for the NADH dehydrogenase, succinate dehydrogenase, cytochrome c, and ATP synthase were uniformly upregulated and peaked at 4 h after CHX release (Fig. 10f, S10b). This probably reflects the energy demand from the increase in protein synthesis, which may also affect the protein degradation rate since it was also an energy-intensive process.

Overall, transcription profiling provides a picture where within 4 h of CHX release, the increase in protein synthesis drives a transient stress response and upregulation in mitochondrial genes to meet the burden of protein quality control, antioxidant and energy demands. At the same time, various metabolic pathways regulated by mTORC1 adapt permanently to the new proteostasis. It does not exclude that transcriptional control of the UPS and E2s could contribute to the increase in protein degradation rate after CHX release; however, the small fold change in related genes means such a contribution is likely to be limited.

2.12. Proteasome content and peptidase activity during CHX release

Previous experiments established that proteasomal mediated degradation of short-lived Timer showed significant change during the CHX addition and release. Since the proteasome degrades the short-lived Timer without ubiquitination, the change in degradation could only result from the alteration in proteasome activity or content. Proteasomal degradation itself contains several successive steps that could be modulated individually. To disentangle which was the critical parameter that caused the adaption of proteasome activity, we performed a series of *in vitro* assays to quantify the proteasome concentration, relative proteasome amount per cell, proteasome assembly form (the 20S, 26S and 30S), and chymotrypsin peptidase activity for samples at different time points after CHX release. The proteasome concentration, amount per cell, and assembly form can be visualised on the tris-acetate native gel, which keeps the protein complex intact on the gel. We expected the proteasome concentration and amount to increase following the CHX release. Surprisingly, proteasomal concentration or amount per cell was slightly higher in CHX-treated cells compared to other conditions (Fig. 11a). Proteasome peptidase activity measured by Suc-LLVY-AMC showed that proteasome peptidase activity per cell was lower in CHX compared to control (Fig. 11b, c), and activity progressively increased following CHX release, though the fold changes were mild. However, measurements from peptidase activity per protein concentration were too noisy to conclude (Fig. 11e, f).

In general, our result suggests that the proteasome concentration is not the factor that drives the protein degradation adaption, nor its assembly form. A mild change in proteasome peptidase activity was observed though it is likely not the main factor in the degradation rate change. As previously discussed, the proteasome activity does not necessarily correlate with the proteasome concentration. The proteasomal peptidase activity assay also does not report the rate of the ATP-driven protein-unfolding process, which is the rate-limiting step of proteasomal degradation.

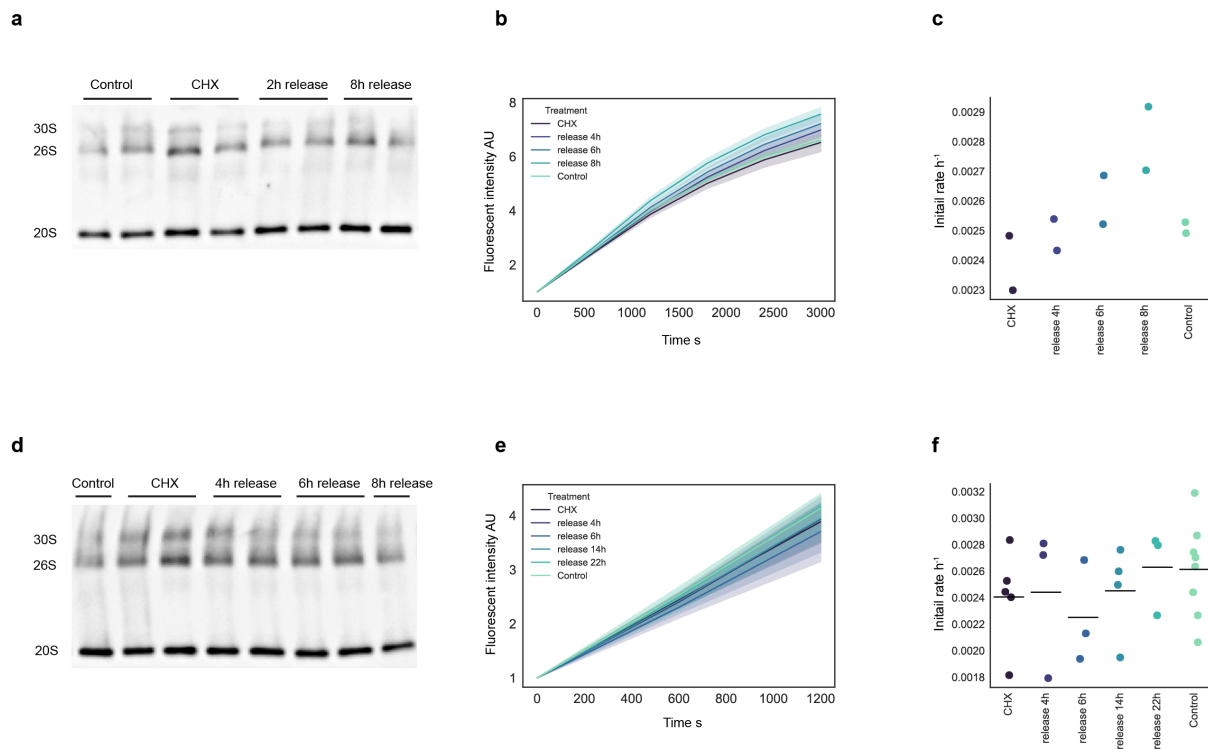


Figure 11 | Measure the proteasome concentration, amount per cell, and activity *in vitro*.

a, Immunoblot of 20S proteasomal subunits on the native gel. Equal volume of lysates extracted from the same number of cells were loaded on each lane. **b**, Fluorescence readout of the proteasome chymotrypsin-like peptidase activity from digestion of the Suc-LLVY-AMC substrate. Lysates of equal numbers of cells were used. Each data point was subtracted from the background measured by applying the proteasome inhibitor lactacystin. **c**, Initial rates of proteasome peptidase activity assay from each sample. They were calculated by linear fitting of data points for the first 1000 s of Fig. 11b. **d**, Immunoblot of 20S proteasomal subunits on the native gel. Equal volume of lysates containing equal amounts of total proteins was loaded on each lane. **e**, Fluorescence readout of the proteasome chymotrypsin-like peptidase activity assay. Lysates of equal total protein amounts were used. Each data point was subtracted from lactacystin background. **f**, Initial rates of the proteasome peptidase activity calculated from Fig. 11e. Solid lines indicate the mean. For **b**, **e**, shading: 95% CI.

2.13. Steady-state protein levels could be predicted using a passive adaption model

Since protein degradation and dilution rates didn't fully compensate for the change in protein synthesis, steady-state protein concentration would therefore alter, which affects both synthesis and degradation rates, as these rates depend on protein concentrations in the respective pathways. If there was no active mechanism to coordinate protein synthesis and degradation, changes in synthesis rates would affect protein concentrations and therefore affect the degradation rates passively (Fig. 12a). We named this process "passive adaption". To model this process, we came up with a mathematical description by introducing the effective concentration of the protein degradation machinery A , whose dynamics could be described by (to simplify the model, dilution will be ignored for the moment):

Eq. 8

$$\frac{d[A]}{dt} = s_A - k_A[A] = s_A - \hat{k}_A[A]^2$$

s_A is the synthesis rate of A , k_A is the turnover rate of A , while \hat{k}_A represents A 's intrinsic, concentration independent protein degradation rate for itself, independent of A 's concentration. We assume that the degradation rate of any protein is proportional to the concentration of A : $k \propto [A]$. Therefore, for the concentration of protein of interest B we have:

Eq. 9

$$\frac{d[B]}{dt} = s_B - k_B[B] = s_B - \hat{k}_B[A][B]$$

s_B is the synthesis rate of B , k_B is the turnover rate of B , while \hat{k}_B represents the concentration independent degradation rate for A degrading B .

Determining the effective cellular concentration of A and the rate \hat{k}_A was a near-impossible task. Nevertheless, we circumvented this problem by finding an analytical solution to derive the fold change of s and k , in which the values of A and \hat{k}_A were not required (See the deduction in chapter 4.18.3.1; Eq. 21 to Eq. 28). In this solution, given the adaption of degradation to the change in synthesis was passive, the fold change of steady-state protein concentrations $[P]_f/[P]_i$ and degradation rates k_f/k_i should equal the square root of the fold change of protein synthesis $\sqrt{s_f/s_i}$ (Eq. 10). We would refer to s_f/s_i as α .

Eq. 10

$$\frac{[P]_f}{[P]_i} = \sqrt{\alpha}$$

This solution was verified by the *in silico* integration of Eq.8 and Eq. 9 to reach the steady state (See chapter 4.17.3.2). Moreover, by assuming that K_{deg} and K_{dil} always kept the exact fold change, which was the case for CHX prolonged treated cells (chapter 2.2. and Table. 1), we could take dilution into account, and prove that Eq.10 still held (See the proof in chapter 4.18.3.3, Eq. 29 - Eq. 32).

The “passive adaption” model could be tested using data obtained from cells prolonged treated with CHX (chapter 2.2. and Table. 1). Before testing this hypothesis, we first needed to exclude the promoter-specific effect, which could affect protein concentration and the generality of our modelling. PGK promoter, which we used to express the short-lived Timer, also controls the expression of Pgl1. In our RNA-seq data, Pgl1 gene was downregulated by 1.2-fold in 0.1 μ g/ml CHX prolonged treated cells, while the decrease in protein concentration was 2-fold at the same CHX concentration according to Table. 1. We reasoned that the effect of the promoter was negligible.

We then plotted the correlation between the fold change of the turnover rate k_f/k_i and α from the short-lived Timer data (Table. 1) against predictions of two naïve models:

1. The “perfect adaption” where K_{deg} neutralises the change in s , and 2. The “no adaption”, where K_{deg} does not change despite a change in s (Fig. 12b).

As expected, the experimental data fell in between the two native models (Fig. 12b). Interesting, the fold change in the protein turnover rate matched well with the prediction of the passive adaption model (Fig. 12c). Furthermore, the fold change of the short-lived Timer concentration also agreed with the passive adaption model, while the change in dilution rate alone was insufficient to explain the protein concentration (Fig. 12d). Changes of both degradation and dilution rates follows the trend of the model prediction (Fig. 12e) across α . For the short-lived Timer, the degradation contributes 70% of the turnover rate and 30% for the dilution, rendering protein degradation the main driving force to attenuate the effect of synthesis (Fig. 12f).

To expand the applicability of the passive adaption model beyond the short-live Timer, we measured the nuclear total protein concentration after treating cells with a series of concentrations of CHX with fluorescently labelled N-Hydroxysuccinimide Ester (NHS ester). NHS ester reacts with amino groups and can be used as a proxy of total proteins (Neurohr et al., 2019). Since the average nuclear proteins have a much slower turnover rate, we treated cells with CHX 6 days before the staining so that long-

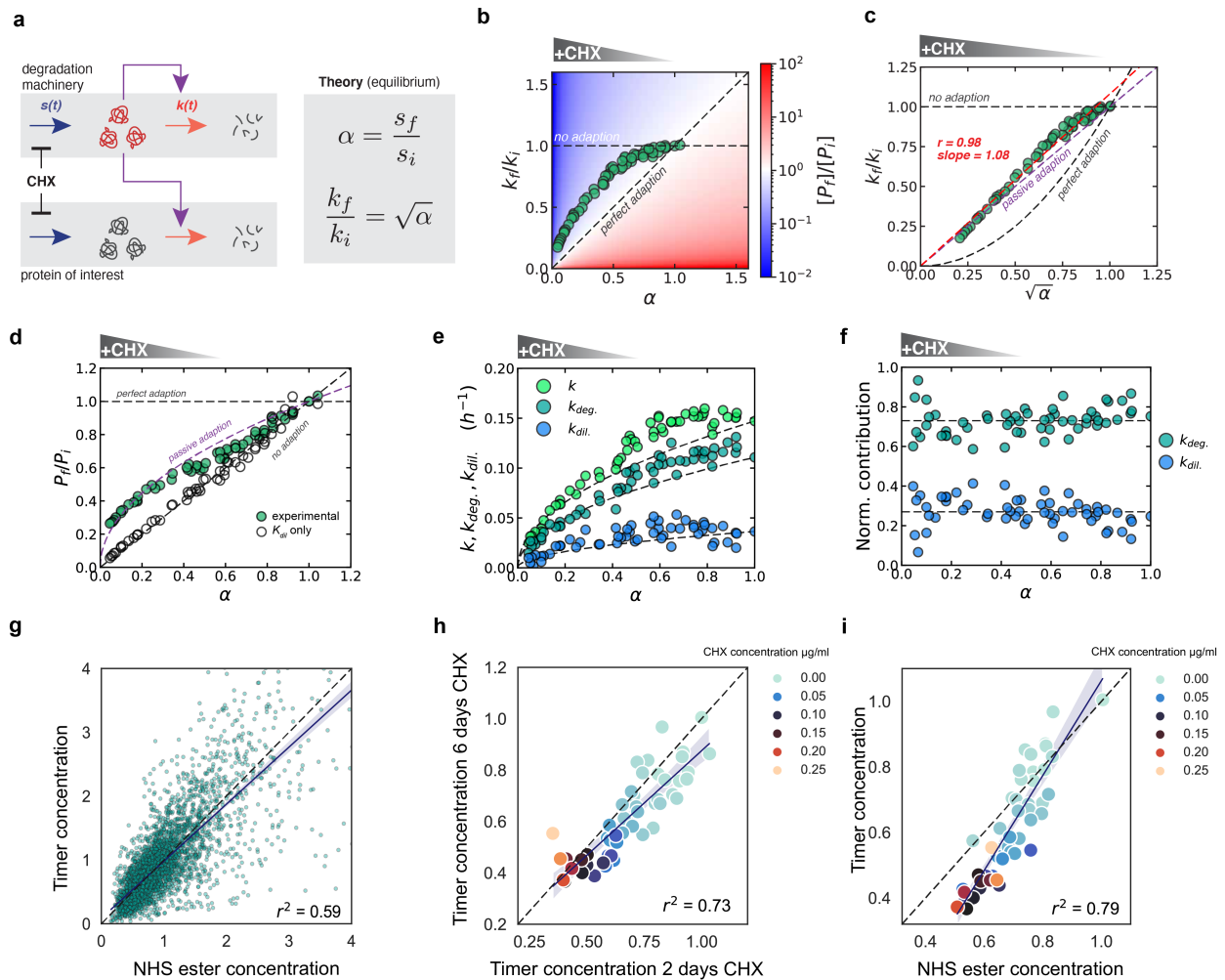


Figure 12 | The change of the steady-state degradation rate could be explained by the “passive adaption” model.

a, The scheme of the “passive adaption” model. On the left, synthesis inhibition reduces the concentration of degradation machinery, causing a decrease in the degradation rate. On the right, the “passive adaption” model predicts the fold-change of the equilibrium degradation rate k_f/k_i equals to the square root of the fold-change of the protein synthesis rate α . **b**, The relation between the fold-change in k_f/k_i and the fold-change in the synthesis rate α (from Fig. 3i, Table. 1) is plotted against two naive models: “perfect adaption” and “no adaption”. The colour gradient signifies the relative steady-state protein concentration in the log 10 scale. **c**, The relation between the fold-change in k_f/k_i and α is plotted against “passive adaption”, “perfect adaption”, and “no adaption” model predictions. The purple diagonal dash line is the correlation predicted by the “passive adaption” model. The red dash line is the observed correlation. **d**, The relation between the fold-change in the Timer relative concentration P_f/P_i and the $\sqrt{\alpha}$ is plotted against “passive adaption”, “perfect adaption”, and “no adaption” model predictions. The black diagonal dash line is the correlation predicted by the “no adaption” model. The “ K_{dil} only” data points are the predicted P_f/P_i against α only considering the change in K_{dil} . **e**, The contribution of K_{deg} and K_{dil} to the change in the total turnover rate k across α . Dash lines are predictions of the “passive adaption” model by fixing the $\alpha = 1$ point. **f**, The relative contribution of K_{deg} and K_{dil} to the change in k across α normalised to k . Dash lines are the mean values. **g**, The correlation of single cells nuclear short-lived Timer concentration versus nuclear NHS ester concentration, which labels the amino group. **h**, The mean of nuclear short-lived Timer concentration is plotted for cells treated for 2 days with a series of concentrations of CHX (Fig. 3) versus cells treated for 6 days of CHX. **i**, The mean of nuclear short-lived Timer concentration is plotted against the mean of nuclear NHS ester concentration for cells treated with CHX for 6 days. For **g**, **h**, and **i**, the Timer and NHS ester concentrations are normalised to the mean of the control, shading: 95% CI.

lived proteins could reach equilibrium. We found that concentrations of nuclear NHS ester and the

short-lived Timer had a reasonable correlation for the control cells (Fig. 12g), validating such an approximation. Encouragingly, the 6-day CHX treatment didn't significantly alter the relative concentration of the short-lived Timer compared to the previous 2-day treatment (Fig. 12h), signifying that the same proteostasis was maintained for this duration. Intriguingly, under CHX treatment, the nuclear NHS ester concentration showed a dose-dependent decrease, indicating a change in global nuclear proteome concentration (Fig. 12i). The concentrations of NHS ester and the short-lived Timer were well correlated across the CHX gradient; however, the correlation deviated from the diagonal line (Fig. 12i), suggesting the concentration of nuclear proteome was more affected by the adaption of protein turnover than the short-lived Timer. We could not definitively conclude from this observation since NHS-ester can stain non-protein components, possibly contributing to the underestimation of the proteome concentration fold change.

To summarize, our result shows that, at least for proteasome substrates, their degradation rates and protein level could be explained by the passive adaption model. Moreover, the global nuclear proteome concentration is altered by synthesis manipulation, but effect of which is buffered by the adaption in protein turnover. However, we cannot conclude whether it follows the passive adaption model. The concentrations of other cellular proteins need to be examined to expand the passive adaption model.

3. Discussion

3.1. Global protein degradation rate is coordinated with protein synthesis

Despite emerging evidence of the existence of protein synthesis and degradation coordination in mammalian cells, the effect and mechanism of such coordination have rarely been investigated. Here, we have generated a series of reversible proteostasis states with protein synthesis inhibitors. With CHX at 0.1 $\mu\text{g/ml}$, cells not only proliferate exponentially after 2 days but also maintain the same proteostasis after 6 days of treatment, signifying that our treatments result in new cellular protein steady states. We have quantified synthesis, degradation, and dilution rates in these series of proteostasis and showed that the protein degradation rate alters significantly when the protein synthesis rate changes. Unlike studies with serum deprivation or mTORC1 inhibition where protein synthesis and degradation are heading towards the opposite direction (Zhao et al., 2015), we have shown that when the synthesis rate is directly manipulated through inhibitors, the change of protein degradation is coordinated with the change in synthesis. Moreover, the shift of degradation rate has an unambiguous buffering effect on both the short-lived Timer reporter's concentration and global nuclear proteome concentration.

Furthermore, we have characterised the dynamic of the adaption of protein degradation following a sudden decrease or increase in protein synthesis. In both cases, it took roughly 10 h for the degradation rate to reach a new equilibrium when adding or releasing CHX or MYCi. This temporal information can be important for the deduction of the mode of such coordination and for studying the regulation of protein degradation rate in the future. Of note, our result should not be compared with previous reports showing CHX alters proteasome activity, as CHX concentrations used in these studies were 200 to 1000 times higher (Dai et al., 2013; Sakellari et al., 2019).

Most of our conclusions were drawn from the short-lived Timer, which binds proteasome directly without ubiquitination, thus directly measuring the proteasome activity. Changes in proteasome activity could influence the degradation rate of the global proteome, which has been demonstrated in various scenarios (Chen et al., 2018; Lokireddy et al., 2015; VerPlank et al., 2020). However, it is yet to see if the whole proteome is affected equally. Most cellular proteins are degraded through ubiquitination, and it has been established that global ubiquitination can be very adaptive at least in stressed conditions. We do find from our experiment that the fold change and the dynamics of K_{deg} following CHX release were almost identical between the short-lived Timer and the long-lived Timer. This is somewhat encouraging given the 10-time difference in their half-lives and the fact that short-lived Timer is degraded by proteasome without ubiquitination. This observation may expand the implication of our result beyond being confined to a specific proteasome targeting reporter protein. However, we cannot

completely exclude the possibility that the long-lived Timer is degraded by the same pathway as the short-lived Timer, as both contain the PEST sequence with a putative proteasome binding site, albeit difference in their c-terminal length. More diverse types of reporter proteins will be needed to probe the effect of degradation adaption on proteins undergone through different degradation pathways. Our data also show that the change in degradation and dilution rates never completely offsets the change in protein synthesis in proliferating cells, suggesting proliferating cells can tolerate a wide range of protein concentrations without a significant impact on viability. Our result does not address the function implication on the buffering effect of protein degradation and dilution towards synthesis. If there had not been any compensation from the degradation, overall protein concentration would be estimated to be 10-20 % lower with synthesis inhibition. As we know, a decrease in global proteome concentration could have a tangible impact on the proliferation rate as well as the decision of cell cycle entry (Neurohr et al., 2019). It remains to see if such a difference can have any physiological influence.

In confluent cells, however, protein degradation has a larger fold decrease with the same level of protein synthesis inhibition compared to proliferating cells. More surprisingly, protein degradation actually over-compensated the change in protein synthesis, causing protein levels to increase immediately after the addition of the synthesis inhibitor. All these results imply that non-proliferating cells tolerate a much narrower range of protein concentration. It is possible that different mechanisms are responsible for maintaining proteostasis in confluent cells with respect to proliferating cells. It has also been shown that confluent cells rely on the autophagy pathway to compensate for the loss of the dilution rate (Welle et al., 2016; Zhang et al., 2017). It would be of great interest to conduct a comparative study that further elucidates the difference in protein degradation dynamic and regulation between proliferating cells and non-proliferating cells.

We could not definitively identify the mechanisms that coordinate protein synthesis and degradation. From RNA-seq, fold change of proteasome and ubiquitin ligases are relatively small. Moreover, we showed that proteasome concentration, amount per cell, and assembly form do not correlate with its activity in degrading the short-live Timer. This leaves us with a few possibilities: 1. The concentration of some proteasome subunits or auxiliary proteins determines the activity of the proteasome. 2. Post-transcription modifications on the proteasome determine the proteasome activity. 3. Cellular concentration of ATP, which may follow the passive adaption, dictates the overall degradation rate. Albert et al. (2020) have shown that most cellular proteasomes are inactive, illustrating that proteasome amount and its cellular activity are not associated directly. We also measured proteasome peptidase activity *in vitro*, which showed a slight change during CHX recovery, but may not be sufficient to explain the fold change of degradation in cells. More comprehensive studies are needed to clarify the source of change in proteasome activity, such as measuring proteasome ATPase activity, *in vitro*

degradation of proteins or ubiquitinated substrate, etc. It is urgently needed to establish the link between the global protein degradation rate and aspects of proteasome activity.

The dynamic change of concentration of proteome presents a problem: how can cells maintain the proteome stoichiometry? We have shown that keeping the relative composition of the proteome requires the degradation rate and dilution rate to maintain the exact fold change, which we have observed in CHX conditions but not with MYCi. The same-fold change rule, in theory, also applies to non-steady-state situations. Our data are not precise enough to prove or disprove this assumption during CHX release or addition. But it is clear that dilution and degradation act in a similar time scale. There are still many questions left unanswered regarding proteome stoichiometry. It is interesting to know if other cellular processes are employed to keep proteome composition during MYCi treatment. What is the consequence if proteome stoichiometry is perturbed? This could be tested by decoupling the protein degradation rate from the dilution rate. Finally, what pathways keep protein degradation and dilution coupled in the first place? A question for which there is no trivial mechanism that could explain.

We have shown that in proliferating cells, the protein degradation rate of direct proteasomal substrate follows the passive adaption model, meaning that the decrease in protein degradation can be primarily explained by the reduction in the global protein concentration caused by protein synthesis inhibition. Passive adaption is an elegant model that could illustrate how cells set the steady-state level protein concentration without any active mechanisms. It seems passive adaption alone is sufficient to explain the change in protein degradation in proliferating cells. However, from *in vitro* assay, we found proteasome concentration did not decrease with the synthesis inhibitor. This presents an apparent paradox, which brings back the question of what dictates the activity of the proteasome. It is feasible to theorise that the concentration of determinants of the proteasome follows the passive adaption, which raises the question of why the Timer concentration follows the prediction of passive adaption while the proteasome concentration does not. We note that proteasome concentration may yet reach the steady state in the duration of our experiment, but it would not be sufficient to explain why no decrease in proteasome level could be observed when cells were treated with CHX.

If passive adaption alone could explain the steady-state protein level, could it also be sufficient to explain the dynamics in the change of the degradation rate in non-steady-states? We don't have the answer to this question yet. It would require more extensive modelling. What we could show from RNA-seq is that other cellular pathways, such as ERAD and UPR, were activated during the period when the degradation rate was increasing to compensate for the synthesis. It is very likely that they contribute to the dynamics of protein degradation as well. Using our non-steady state context as the basis, it could be possible to target these pathways during degradation recovery to investigate their involvement in the coordination between synthesis and degradation.

3.2. Measure dynamics of protein synthesis and turnover rates

This study presents a novel microscopy-computation method to measure protein synthesis and turnover rate by combining Timer measurement with a superstatistical Bayesian inference algorithm. We also employed the same method for more straightforward problems, such as solving the evolution of cell division rate over time and the evolution of degradation rate from the SNAP pulse-chase labelling method. In fact, very few studies have achieved comparable temporal resolution of protein synthesis degradation rates in general, especially without prior assumptions about their dynamics. We have demonstrated that it is possible to model complicated cellular dynamics with a relatively simple microscopy technique and limited computational resources. In addition, the model prediction could be used to recapitulate the empirical data by retrodiction, which provides a compelling metric to evaluate the modelling quality. We believe that the modelling methods employed here hold great promise for solving other kinds of dynamic data containing multiple time-varying parameters.

A few challenges have emerged while modelling the Timer traces. The computational method is robust in dealing with unstructured noise but highly prone to systematic aberrations common in microscopy data. Thus, accurate illumination correction, robust background estimation, and minimising bleaching are prerequisites for any quantitative analysis. It is also imperative to avoid overcrowding of the cells over a long treatment period, which will result in futility in accurately estimating the background. Even if these steps are correctly taken, additional anomalies could arise from the autofluorescence of drugs and medium, temperature fluctuation, the flickering of autofocus, etc. Therefore, independent methods should always be applied to validate the modelling result.

4. Material and Method

4.1. Cell Culture

NIH3T3 and HEK293T cells were routinely cultured in DMEM (Gibco; 41966029), supplemented with 10% fetal bovine serum (Gibco, 10270-106), 1% Penicillin/Stre (BioConcept, 401F00H) at 37 °C, 5% CO². Cells were passaged by trypsinization (Sigma, T4049-100ML) every 2-3 days while confluency reached no more than 80%. E14 mouse embryonic stem cells were routinely cultured in GMEM (Sigma-Aldrich, G5154) supplemented with 10% ES cell-qualified fetal bovine serum (Gibco, 16141-079), 2 mM sodium pyruvate (Sigma-Aldrich, 113-24-6), 1 % non-essential amino acids (Gibco, 11140-050), 1% penicillin/streptomycin (BioConcept, 4-01F00H), 2 mM L-glutamine (Gibco, 25030-024), 100 μM 2-mercaptoethanol (Sigma-Aldrich, 63689), leukaemia inhibitory factor (in-house, cite), 3 μM GSK-3 Inhibitor XVI (Merck, 361559) and 0.8 μM PD184352 (Sigma-Aldrich, PZ0181) at 37 °C, 5% CO². Cells were plated on gelatin (Sigma-Aldrich, G9391) coated dishes. Cells were passaged every 2-3 days by trypsinization (Sigma-Aldrich, T4049) when density reached approximately 3.0×10⁴ cells/cm² (Mulas et al., 2019).

4.2. Live-imaging of Timer after prolonged treatments with inhibitors

Roughly 72 h before imaging, NIH3T3 cells were seeded on a 96-well plate coated with fibronectin (Sigma, F4759) at a density that does not exceed 80% confluency for each well when imaging starts. For example, if cells were to be treated with CHX at 0.1 μg/ml or MYCi at 64 μM for 48 h, 800 cells should be seeded per well, whereas non-treated control cells should be seeded 200 cells per well. After seeding, cells were cultured overnight without the drug in FluoroBrite™ DMEM (Gibco, A1896701) supplemented with 10% fetal bovine serum (Gibco, 10270-106), 2 mM L-glutamine (Gibco, 25030-024), and 1% Penicillin/Stre (BioConcept, 401F00H). The next day, drugs were applied at desired concentrations. During the treatment, the medium was changed every 24h. Before imaging, all wells were washed once with medium, and then medium containing desired drug concentration was added. Live-imaging was performed with Operetta CLS (Perkin Elmer), 20× objectives (Air immersion, Plan Apochromat, NA 0.8), at 37 °C, 5% CO², with 15 min intervals for more than 20h if not specified otherwise. For the sfGFP channel, the filter Ex: BP 435-460, 460-490, Em: HC 500-550 was used. For the mOrange2 channel, the filter Ex: BP 490-515, 530-560, Em: HC 570-650 was used.

4.3. Use the SNAP tag to measure the degradation rate

Cells were seeded and cultured in 96-well plates following the live-imaging procedure. 45 minutes before imaging, cells were incubated with an imaging medium that contained SNAP Cell 647 Sir dye (NEB, S9102S) for 30 min. Cells were then gently washed five times with fresh medium, which took

about 15 min. Then the fresh imaging medium was added containing SNAP Cell Block (NEB, S9106S), which was to prevent the binding of the residue SNAP dye to newly synthesized SNAP-tagged proteins. Imaging was performed with Operetta CLS (Perkin Elmer), 20× objectives (Air immersion, Plan Apochromat, NA 0.8), at 37 °C 5% CO₂, at 15 min intervals. For the sfGFP channel, the filter Ex: BP 435-460, 460-490, Em: HC 500-550 was used, and for the SNAP channel, the filter Ex: BP 615-645, BP 650-675, Em: HC 655-760 was used. The imaging analysis will be detailed below.

4.4. Measure protein synthesis rates by L-Homopropargylglycine labelling

L-Homopropargylglycine, an alkyne surrogate of methionine, can be incorporated into the elongating peptides replacing the methionine. The alkyne group can be then conjugated with a fluorophore containing an azide group. L-Homopropargylglycine (HPG) labelling was performed using Click-iT™ HPG Alexa Fluor™ 594 Protein Synthesis Assay Kit (Invitrogen, C10429).

Cells were seeded on a 96-well plate coated with fibronectin (Sigma, F4759), and we applied CHX or MYCi treatment for 48 h, as described in chapter 2.3. and 2.4. Before HPG labelling, negative control cells were treated with CHX 100 µg/ml for 30 min. For HPG labelling, we followed the manufacturer's instructions. To summarize, methionine and cystine-free DMEM medium (Gibco, 21013024) supplemented with HPG 50 µM (Invitrogen, C10186), cysteine 200 µM (Sigma-Aldrich, 168149), and β-mercaptoethanol (Sigma-Aldrich, M3148), as well as the corresponding concentration of CHX or MYCi, was added to cells, and then incubated for 30 min or specified otherwise. Cells were washed once with PBS before fixing with 4% formaldehyde in PBS for 15 min at room temperature (RT). The fixative was subsequently removed, and cells were washed twice with PBS containing 3% BSA. Cells were then permeabilised with 0.5% Triton® X-100 in PBS for 20 min at RT before washing once with PBS containing 3% BSA. The click-reaction proceeded as follows. The reaction cocktail was prepared by following the manual. In the click-reaction cocktail, Alexa 647 Azide (Invitrogen, A10277) was used instead of Alexa Fluor™ 594 provided in the kit. Cells were incubated for 30 min with the reaction cocktail at RT and protected from light. The reaction cocktail was then removed, and cells were washed once with Click-iT® reaction rinse buffer (Component F). Nucleus staining was performed by incubating cells with 1X HCS NuclearMask™ Blue Stain (Component G) in PBS for 30 minutes at RT, protected from light. Cells were washed twice with PBS containing 3% BSA. Finally, samples were mounted with PBS. Imaging was carried out with Operetta CLS (Perkin Elmer), 20× objectives (Air immersion, Plan Apochromat, NA 0.8), at RT, using the filter Ex: BP 615-645, BP 650-675, Em: HC 655-760 for the HPG channel.

4.5. Measure protein synthesis rates by O-propargyl-puromycin labelling

O-propargyl-puromycin (OPP) is an alkyne analog of puromycin that can be incorporated into the elongating peptides and blocks the elongation. The truncated proteins are then released from ribosomes. OPP labelling was performed using Click-iT™ Plus OPP Alexa Fluor™ 647 Protein Synthesis Assay Kit (Invitrogen, C10458).

3T3 or mESC cells were seeded on a 96-well plate with corresponding coatings. Before OPP labelling, negative control cells were treated with CHX 100 µg/ml for 30 min. For OPP labelling, we followed the manufacturer's instructions. To summarize, OPP was diluted in cell culture medium to 20 µM final concentration. This medium (with corresponding concentration of CHX or MYCi) was added to cells for a 30 min incubation or specified otherwise. Cells were washed once with PBS before fixing with 4% formaldehyde in PBS for 15 min at room temperature (RT). The fixative was subsequently removed, and cells were permeabilised with 0.5% Triton® X-100 in PBS for 15 min at RT before washing once with PBS. The click-reaction proceeded as follows. The reaction cocktail was prepared by following the manual. Cells were incubated for 30 min with the reaction cocktail at RT and protected from light. The reaction cocktail was then removed, and cells were washed once with Click-iT® reaction rinse buffer (Component F). Nucleus staining was performed by incubating cells with 1X HCS NuclearMask™ Blue Stain (Component G) in PBS for 30 minutes at RT, protected from light. Cells were washed twice with PBS. Finally, samples were mounted with PBS. Imaging was carried out with Operetta CLS (Perkin Elmer), 20× objectives (Air immersion, Plan Apochromat, NA 0.8), at RT, using the filter Ex: BP 615-645, BP 650-675, Em: HC 655-760 for the OPP channel.

4.6. Measure total nuclear protein concentration by *N*-Hydroxysuccinimide

Cells were seeded on a 96-well plate coated with fibronectin (Sigma, F4759) and cultured overnight. The cell seeding number was adjusted so that on day 7, none of the wells should be more than 80% confluent. On day 2, 48 different CHX concentrations ranging from 0.002 to 0.25 µg/ml were applied to cells for the next 6 days. The medium was changed every 48 h.

On day 7, cells were fixed with 4% formaldehyde in PBS for 15 min at RT before washing once with PBS. Then, cells were permeabilized with 100% pre-cooled methanol at -20 °C for 10 min. Before staining, cells were washed once with 0.2 M sodium bicarbonate. The *N*-Hydroxysuccinimide (Invitrogen, A37573) was diluted in 0.2 M sodium bicarbonate to a final concentration of 50 µg/ml and applied to cells at RT for 30 min. The cells were washed twice with PBS and mount with Vectashield containing DAPI (Vector, H-1500-10). Imaging was performed with Operetta CLS (Perkin Elmer), 20× objectives (Air immersion, Plan Apochromat, NA 0.8), at RT, using the filter Ex: BP 615-645, BP 650-675, Em: HC 655-760 for the NHS-ester channel.

4.7. Image pre-processing

For background correction, image intensity was modelled as such:

Eq. 11

$$I_{total} = f(I_{FOI} + I_{AF} + D)$$

I_{total} is the intensity value of the raw image. f is the uneven illumination pattern. I_{FOI} is the fluorescence signal of interest. I_{AF} is the auto-fluorescence from the medium. D is the dark field signal. In practice, D was ignored as it was negligible compared to I_{FOI} or I_{AF} . f was generated by imaging a well only with the medium with the same exposure settings. This image was subsequently normalized to its mode and named f image. Raw images were divided by f image to generate flat-field corrected images. I_{AF} was calculated for every single frame by applying the appropriate thresholding method to the field-corrected images, which created a binary image that masked foreground signals I_{FOI} ('Percentile' was used for short-lived Timer traces). The mask was then enlarged by erosion. Finally, the mean or the mode was measured from the unmasked region. We didn't generate background subtracted images but rather subtracted this value from final single-cell measurements inside the Jupyter notebook.

4.8. Cell segmentation and tracking

For segmentation and tracking nuclear Timer cells, Trackmate (7.1) (Ershov et al., 2022) was used through a groovy script (written by Olivier Burri and Romain Guet, EPFL) that enabled processing images in batch. This script was tailored for using the Stardist (Schmidt et al., 2018) as the detector to segment cell nuclei on the sfGFP channel. Tracking was then performed with the LAP algorithm (Munkres, 1957) inside the same script. The script generated Trackmate XML files that permitted the review of the tracking result with the Trackmate user interface. Both sfGFP and mOrange2 traces were smoothed with a Savitzky-Golay filter (window length: 100, polynomial order: 6) (Savitzky and Golay, 1964) prior to superstatistical modelling.

For HPG labelling, cytoplasm segmentation was performed by Cellpose 2.0 (Stringer et al., 2020) guided by both HPG and nucleus channels, employing a built-in "Cytoplasm2" model.

4.9. Calculate s , k , and K_{deg} from SNAP pulse-chase labelling

To measure the degradation rate with SNAP, the integrated intensity for each lineage was transformed by natural log, then linear-fitted with a standard linear regressor or a robust RANSAC regressor (random state: 42) from the scikit-learn package (1.0.2). When cells were divided, intensities from daughter cells were summed.

To measure the total protein turnover rate with SNAP, which was the combined effect of K_{deg} and K_{dil} , the mean intensities for each lineage were transformed by natural log and then linear-fitted with a robust regressor RANSAC (random state: 42). When cells were divided, intensities from daughter cells were averaged.

To compute the rates s , we assumed equilibrium for all our measurements. With μ_G, μ_R , the mean intensity for sfGFP and mOrange2 fluorescence, we computed the synthesis rate as:

Eq. 12

$$s = \mu_G \times \frac{k(m_G + k)}{m_G}$$

To translate fluorescence into concentrations, and thus take into account the volume-mediated effect on the degradation rate, we first computed the volumetric mean intensity (concentration) v_G . To do so, we computed the (average) nucleus volume (in pixels) V_{nuc} from the (average) nucleus size S_{nuc} assuming a spherical nucleus (refs):

Eq. 13

$$V_{nuc} = \frac{4}{3} \times \frac{S_{nuc}^3}{\sqrt{\pi}}$$

It comes:

Eq. 14

$$v_G = \frac{\mu_G \times S_{nuc}}{V_{nuc}}$$

From this we can compute the synthesis rate s in *concentration.h⁻¹* [*concentration* \equiv *fluorescence.(pixel - size)⁻³*]:

4.10. Calculate K_{dil} from time-lapse movies

To measure the dilution rate, two separated methods were used. Either rate of cell division was measured by counting cell number per imaging frame over time, or the nuclear growth rate was measured by segmenting nuclei area and tracking its expansion over time. The dilution rate was then calculated by transforming the cell number or area with the natural log and linear fitted with the RANSAC regressor (random state: 42). K_{dil} was also calculated by $k - K_{deg}$ when the cell number was not sufficient.

4.11. Estimate the mOrange2 maturation rate

To use the Timer data quantitatively, *i.e.*, to compute the protein synthesis and the turnover rates, s and k respectively, we need to estimate the values of the constants appearing in Eq. 3, namely m_G , m_R , in addition to the already described technical parameter α . We assumed that the maturation rate for sfGFP was close to the previously reported value ($m_G \approx 6h^{-1}$) (Pédelacq et al., 2006). and determined m_R by matching the degradation rate k measured with SNAP chase — in different drug treatment conditions (Table. 1)— from the one computed using the green over red ratio. Mathematically, we maximized the log-transformed ℓ_2 -norm:

Eq. 15

$$m_{R,i}^* = \arg \max_{m_R \in \Omega_{m_R}} - \ln \left[(k_{\mathcal{R},i}(m_R) - k_{SNAP,i})^2 \right]$$

for $\Omega_{m_R} = [0.01,1]$ discretized in 10^5 linear bins. $k_{SNAP,i}$ is the degradation rate measured from the SNAP chase experiment in drug condition i (Table.1). $k_{\mathcal{R},i}(m_R)$ is the degradation rate computed from the timer's sfGFP and mOrange2 fluorescence for a given maturation rate m_R (see related section) and condition i . $m_{R,i}^*$ is the optimal — *i.e.*, inferred — maturation rate for mOrange2 protein at the condition i . We then selected the maturation rate, \widehat{m}_R , as the median of all $m_{R,i}^*$.

4.12. RNA extraction, library preparation and sequencing

Cells were collected by trypsinization (Sigma, T4049-100ML), then pelleted by centrifuge at 1000 rpm 5 min at RT. Cell pellets were flash-frozen in liquid nitrogen and then stored at -80. For RNA extraction, pellets were resuspended in Buffer RLT (74004, Qiagen), and then RNA was extracted using RNeasy Micro Kit (74004, Qiagen) following the manufactural instruction. After RNA extraction, RNA concentration and quality were measured by the Nanodrop one (Thermo Fisher) and Tapestation TS4200 (Agilent). Some variability in samples' qualities was observed, with RIN values from the Tapestation TS4200 ranging from 7 to 10. Still, the overall quality was good enough for the polyA-based stranded mRNA library prep method. mRNA library preparation was performed using "Illumina stranded mRNA ligation" (ISML) prep with 1000 ng of RNA per sample, according to Illumina protocol 1000000124518 v01. Library concentrations and qualities were determined by the Qubit DNA HS (Thermo Fisher) and TapeStation TS4200 (Agilent). Libraries bearing unique dual indexes were subsequently loaded at 100 pM on a Novaseq 6000 SP flow cell (Illumina) and sequenced according to manufacturer instructions, yielding pairs of 60 nucleotide reads. Reads were trimmed of their adapters with belconvert v00.000.000.3.9.3 (Illumina) and quality-controlled with fastQC v0.11.9. FastQ Screen v0.14.0 tool was used for screening FASTQ file reads against multiple reference genomes.

4.13. RNA-seq data processing

RNA sequencing processing was performed on the Galaxy EU server. Sequences were aligned by HISAT2 (Kim et al., 2019) to the murine mm10 genome. Mapped reads were counted by the FeatureCounts (Liao et al., 2014). Reads normalization and differential expression were performed by the DEseq2 (Love et al., 2014). r-Log normalized counts were used for transcriptome analysis.

4.14. Transcriptome analysis

Transcriptome analysis was performed in a Jupyter notebook. PCA was performed on rescaled data using Standard Scaler (scikit-learn 1.0.2). The contribution of genes to each PCA axis was calculated. The top 1000 genes with the highest contributions on PCA 2 axis were selected, and their dynamics were visualized by hierarchical clustering. In parallel, r-Log normalized data were clustered by the Agglomeration algorithm. Ten clusters were set to find subsets of genes that exhibited different dynamics over CHX release. Over-representation assay was performed for selected clusters using the GSEAPy package. A subset of pathways was selected based on enrichment scores or their functions, on which the normalized reads of individual genes were mapped. In addition, The Gene Set Enrichment Assay (GSEA) was performed for selected gene sets between CHX and 4 h CHX release samples using the GSEAPy package. Differential expression of genes in the enriched pathways as visualized by the Pathview (Luo et al., 2017; Luo and Brouwer, 2013).

4.15. Native protein extraction

Cells were collected by trypsinization (Sigma, T4049-100ML) and then pelleted by centrifugation at 1000 rpm 5 min at RT before flash-freezing in liquid nitrogen. In order to estimate cell numbers in the pellets, a small fraction of cells was pelleted separately and counted on a Countess II (Thermo Fisher) machine. Pellets could then store at -80 indefinitely. Proteins were extracted by resuspending pellets in the lysis buffer (50 mM Tris-HCl, pH 7.5, 250 mM sucrose, 5 mM MgCl₂, 0.5 mM EDTA, 0.025%, 2mM ATP, 1 mM DTT). When downstream experiments required samples to be normalized to cell number, the additional lysis buffer was added and designed to compensate for each sample's difference in cell number. The volume of lysis was always 4-5 times the volume of the pellet. Resuspended pellets were incubated on a rotor at 4 °C for 30 min. Afterwards, lysates were centrifuged at 12'000xg for 15 min at 4 °C and supernatants were collected, aliquoted and stored at – 80 °C.

When samples were to be normalized to the protein concentration, an equal volume of lysis buffer was used to resuspend pellets (4-5 times the volume of the pellet). Resuspended pellets were incubated on

a rotor at 4 °C for 30 min. After collecting supernatants by centrifuge, a reducing agent-compatible BCA assay (Abcam, ab207003) was performed to determine the protein concentration. Additional lysis buffer was added to samples to compensate for the difference in the protein concentration. Lysates were then aliquoted and stored at – 80 °C.

4.16. Proteasome native gel and Western blot

The native gel was performed following the protocol from Yazgili et al., (2021). Briefly, 5X native gel loading buffer (0.05% (w/v) Bromophenol Blue, 43.5% Glycerol, 250 mM Tris (pH 7.5)) was added to cell lysates, which were then loaded on a NuPAGE 3%–8% Tris-Acetate gel (Invitrogen, EA0378BOX), 20 µl per well. For the gel running buffer, Novex™ Tris-Glycine Native Running Buffer (Invitrogen, LC2672) was used, supplemented with 5 mM MgCl₂ and 1 mM ATP. The gel was run at 150 V for 4 h at 4 °C. In order to transfer proteins to the membrane for Western blot, the gel was soaked in Solubilisation Buffer (2% (w/v) SDS, 66 mM Na₂CO₃, 1.5% (v/v) β-Mercaptoethanol) for 10–15 min at RT. Meanwhile, a PVDF membrane (Merck Millipore, IPVH07850) was activated by soaking into methanol for 1 min. Subsequently, wet electroblotting was performed at a constant current of 40 mA overnight with standard transfer buffer (1X transfer buffer, 10% ethanol (v/v)). Immunoblotting was performed as follows. Firstly, unspecific binding sites of the PVDF membrane were blocked with Block solution (PBST 0.05% Tween + 5% BSA) for 1 h at RT. Then, the membrane was placed into a 50ml falcon tube and incubated with primary antibody (Anti-Proteasome 20S alpha 1+2+3+5+6+7, Abcam, ab22674, 1/1000 diluted) diluted in Block solution on a rotator at 4°C overnight or 1 h at RT. After being stained with the primary antibody, the membrane was washed once with PBST (0.1% Tween) for 10 min at RT. The secondary antibody staining was performed with the Horseradish peroxidase (HRP) Conjugated secondary antibody (Anti-Mouse IgG (H+L), HRP Conjugate, Promega, W4021, 1/10'000 diluted) diluted in Block solution. The secondary antibody was incubated with the membrane on a rotator for 45 min at RT. Four washing steps were then performed: once with PBST (0.1% Tween) for 5 min; and three times with PBS-T (0.05% Tween) for 15 min each. The membrane was put into a small black box to perform a chemiluminescent reaction with Clarity Western ECL Substrate (BIO-RAD, 170-5060). Imaging of the membrane was carried out with FUSION FX (VILBER).

4.17. *in vitro* proteasomal chymotrypsin peptidase activity assay

The chymotrypsin peptidase activity of the proteasome was measured in cell lysates with the fluorogenic substrate Suc-Leu-Leu-Val-Tyr-AMC. First, the Suc-Leu-Leu-Val-Tyr-AMC substrate (Enzo, BML-PW8720) was diluted in Lysis buffer (without digitonin) to 1 mM (10X working solution). Then, 90 µl cell lysate was added per well of a 96-well plate. For each sample, a control was planned

by inhibiting proteasome activity with proteasome inhibitor lactacystin. This was to determine the background caused by other peptidases. Lactacystin (Enzo, BML-PI104-0200) was added 30 min before the assay at 25 μM final concentration and incubated with lysates for 30 min at 37 $^{\circ}\text{C}$. The chymotrypsin peptidase activity assay was performed by adding 10 μl 10X Suc-Leu-Leu-Val-Tyr-AMC working solution to each well. The final concentration of the substrate was 100 μM if not stated otherwise. The fluorescent signal was recorded at 10 min intervals for 1 h at 37 $^{\circ}\text{C}$, using a Spark[®] plate reader (Tecon). The machine was set Ex/Em at 380/460 nm, 50% gain.

Background intensity measured from the lactacystin control was subtracted for individual samples at each time point. During the first few time points, the fluorescence increase was linear. The initial rate V_0 could be calculated from the slope of the fluorescence signal over time and was used as the relative proteasomal peptidase activity.

4.18. Modelling and inference of Timer

4.18.1. Inference algorithm — Timer trajectories

4.18.1.1. Principle

We adopted a superstatistical Bayesian inference algorithm developed by Metzner et al., 2015 for autoregressive models (AR-1) for ordinary differential equation (ODE) systems. We computed the (joint) posterior distribution of s and k along with the latent variable B_G (see related section) at each timepoint and propagated this posterior forward and backwards along the trajectory. In our case, the trajectories used for the inference are G (sfGFP) and R (mOrange2) fluorescence trajectories acquired by live-cell imaging. Propagation of the posterior distribution relies on two hyperparameters chosen for their ability to recapitulate the data (data retrodiction) and fixed for a whole dataset.

4.18.1.2. Likelihood

The posterior distribution was computed from the likelihood. Keeping the same argument as in the original Alber et al. (2018) study, we chose a likelihood suitable for Gaussian processes — *i.e.*, we assumed normally distributed and independent measurement errors. Therefore, the likelihood \mathcal{L} reads:

Eq. 16

$$\mathcal{L} = P(G_o(t), R_o(t)|s(t), k(t), B_{G_0}G_0, t) = \frac{1}{\sigma\sqrt{2\pi}} e^{-\frac{(G_o(t)-G_m(t))^2}{2\sigma^2}} \times \frac{1}{\sigma\sqrt{2\pi}} e^{-\frac{(R_o(t)-R_m(t))^2}{2\sigma^2}}$$

with $\sigma = 20$, which could be considered a hyperparameter of the algorithm. $G_o(t)$ ($G_m(t)$) and $R_o(t)$ ($R_m(t)$) are the observed (modelled) sfGFP and mOrange2 fluorescence at time t , respectively.

4.18.1.3. Data retrodiction

For data retrodiction, we used inferred time evolution of the rates s and k along with inferred "black-green" fluorescent protein level B_G to integrate the ODEs describing the time evolution of timer species levels (see related section). Briefly, we used DifferentialEquations.jl package (Rackauckas and Nie, 2017) in Julia to integrate the ODE system using Euler integrator, a timestep of 0.001 hours, and applying forcing functions $s(t)$, $k(t)$ and $B_G(t)$.

4.18.1.4. Test on synthetic data

To gain confidence in the ability of our algorithm to infer the time-variation of the protein synthesis and decay rate s and k , we generated synthetic timer trajectories with known underlying dynamics of the rates. We integrated the set of equations describing timer fluorescence dynamics *in silico* using DifferentialEquations.jl in Julia programming language. Tsit5() integrator was used, with a total integration time of 30 h and a sampling time of 15 min to mimic experimental data. Gaussian noise, $\mathcal{N}(0,10)$, was then added to the trajectories in order to mimic experimental noise. All other model parameters were fixed to biological plausible values. For all cases tested, including non-realistic extreme rates time-variations (e.g. dephased sinusoidal variations), we observed a close-to-perfect agreement between inferred time variations and ground truth.

4.18.2. Inference algorithm — SNAP and cell number trajectories

4.18.2.1. SNAP trajectories

We assumed that the time variation of SNAP fluorescence level is described by:

Eq. 17

$$S(t) = S(t = 0)e^{-k(t) \times t}$$

where S is the SNAP fluorescence level, and $k(t)$ is the (time-dependent) decay rate of the fluorescence.

The likelihood \mathcal{L} used for the inference is:

Eq. 18

$$\mathcal{L} = P(S_{norm,o}(t)|k(t), t) = \frac{1}{\sigma\sqrt{2\pi}} e^{-\frac{(S_{norm,o}(t)-S_{norm,m}(t))^2}{2\sigma^2}}$$

with $\sigma = 0.0125$, which can be considered as a hyperparameter of the algorithm. $S_{norm,o}$, respectively $S_{norm,m}$, is the observed, respectively modelled, normalized (at timepoint $t = 0$) SNAP fluorescences at time t .

4.18.2.2. Cell number trajectories

We assumed that the time variation of cell number N is given by:

Eq. 19

$$N(t) = N(t = 0)2^{k(t) \times t}$$

where $k(t)$ is the (time-dependent) growth rate. The likelihood \mathcal{L} used for the inference is:

Eq. 20

$$\mathcal{L} = P(N_{norm,o}(t)|k(t), t) = \frac{1}{\sigma\sqrt{2\pi}} e^{-\frac{(N_{norm,o}(t)-N_{norm,m}(t))^2}{2\sigma^2}}$$

with $\sigma = 0.005$, which can be considered as a hyperparameter of the algorithm. $N_{norm,o}$, respectively $N_{norm,m}$, is the observed, respectively modelled, normalized (at timepoint $t = 0$) cell number at time t .

4.18.3. Passive adaption model

4.18.3.1. Principle

Let's use the following definition for the concentrations: *Protein degradation machinery* $\equiv A$ and *Any protein* $\equiv B$. Without the consideration of the dilution, the effective concentration of A varies according to:

Eq. 8

$$\frac{d[A]}{dt} = s_A - k_A[A] = s_A - \hat{k}_A[A]^2$$

because we assume that the degradation rates are proportional to the effective protein degradation machinery concentration: $k \propto [A]$. For B we have:

Eq. 9

$$\frac{d[B]}{dt} = s_B - k_B[B] = s_B - \hat{k}_B[A][B]$$

At steady-state $d[A]/dt = d[B]/dt = 0$ It implies that:

Eq. 21

$$[A]_{eq} = \left(\frac{s_A}{\hat{k}_A} \right)^{\frac{1}{2}}$$

and:

Eq. 22

$$[B]_{eq} = \frac{s_B}{\hat{k}_B} \times \left(\frac{s_A}{\hat{k}_A} \right)^{-\frac{1}{2}}$$

Now imagine $s_A \propto s_B \propto s$ and imagine $\hat{s} = s/\alpha$ it implies that $\hat{s}_A \propto \hat{s}_B \propto \hat{s}$

Interestingly we have:

Eq. 23

$$[B]_{eq} \Big|_{\hat{s}} = \frac{s_B}{\alpha} \times \frac{1}{\hat{k}_B} \times \left(\alpha \frac{\hat{k}_A}{s_A} \right)^{\frac{1}{2}} = \sqrt{\frac{1}{\alpha}} \times [B]_{eq} \Big|_s$$

and importantly:

Eq. 24

$$[B]_{eq} \Big|_{\hat{s}} = \frac{\hat{s}_B}{\hat{k}_B} \times \frac{\sqrt{\alpha}}{[A]_{eq} \Big|_s}$$

and defining the effective degradation rate \tilde{k}_B we obtain:

Eq. 25

$$[B]_{eq} \Big|_{\hat{s}} = \frac{\hat{s}_B}{\tilde{k}_B}$$

with:

Eq. 26

$$\tilde{k}_B = \hat{k}_B \times \frac{[A]_{eq}|_s}{\sqrt{\alpha}} = k_B|_s \times \frac{1}{\sqrt{\alpha}}$$

which finally implies:

Eq. 27

$$\frac{k_B|_s}{\tilde{k}_B} = \sqrt{\alpha}$$

Finally, it is worth noting that in this case, the equilibrium protein level $[B]_{eq}$ fold change is given by:

Eq. 28

$$\frac{[B]_{eq}|_{\hat{s}}}{[B]_{eq}|_s} = \sqrt{\alpha}$$

In conclusion, the holistic approach consists in assuming proteostasis as an interlinked network, so assuming *long-range interactions* leads to a change in the degradation rate k_B only due to a *global change* in the synthesis rate s . It also proves that *long-range interactions* and *self-regulation in the network* disrupt canonical homeostasis.

4.18.3.2. *In silico* passive adaption model simulation

To validate our analytical developments, we integrated the set of equations describing passive adaption until reaching a steady state. Integration was performed using DifferentialEquations.jl in Julia programming language. Tsit5() integrator was used. We observed a perfect correspondence between simulation results and analytical predictions for $k_f/k_i \equiv k_B|_s/\tilde{k}_B$ and $[P]_f/[P]_i \equiv [B]_{eq}|_{\hat{s}}/[B]_{eq}|_s$.

4.18.3.3. Model approximations taking dilution into account

In reality, we have to take into account protein dilution coming from cell division (and cell growth). The previous equations read:

Eq. 29

$$\frac{d[A]}{dt} = s_A - k_A[A] = s_A - (\hat{k}_A[A] + k_{dil})[A]$$

Eq. 30

$$\frac{d[B]}{dt} = s_B - k_B[B] = s_B - (\hat{k}_B[A] + k_{dil})[B]$$

So, at equilibrium, we have:

Eq. 31

$$[A]_{eq} = \frac{k_{dil} \pm \sqrt{k_{dil}^2 + 4s_A \hat{k}_A}}{2s_A}$$

and our previous simplification leading to the closed Eq. 27 stands only if

Eq. 32

$$\frac{k_{dil} \pm \sqrt{k_{dil}^2 + 4\alpha s_A \hat{k}_A}}{2\alpha s_A} \approx \left(\frac{s_A}{\hat{k}_A}\right)^{\frac{1}{2}}$$

for all α , as defined in the previous section. We observe that this is the case (relative error $< 1\%$ for $\alpha \geq 0.1$) with realistic parameters' values. Analytically, assuming $k_{dil} \ll \alpha s_A$ we recover relation Eq. 29. This can be replunged into equation Eq. 30 and observing that $FI(k_{dil}) = FI(\hat{k}_B[A])$ where $FI(.)$ is the fold increase between conditions, we can recover Eq. 27.

4.18.3.4. Effect of the cellular volume

Let's now rewrite our previous equations in terms of concentrations, i.e. dropping the hypothesis the volume of the cell is constant at all drug concentrations.

For instance, let us take:

Eq. 33

$$\frac{d[B]}{dt} = s_B - k_B[B]$$

Dividing by the cellular volume Ω we recover:

Eq. 34

$$\frac{d\frac{[B]}{\Omega}}{dt} = \frac{s_B}{\Omega} - k_B \frac{[B]}{\Omega}$$

Now, imagine that there is no adaption of the degradation through structural homeostasis — this is equivalent to assuming $[A]$ is constant:

Eq.35

$$\frac{d[B]}{dt} = \frac{s_B}{\Omega} - k_B \frac{[B]}{\Omega} = \frac{s_B}{\Omega} - \hat{k}_B \frac{[A][B]}{\Omega^2}$$

Interestingly we have:

Eq. 36

$$k_B = \hat{k}_B \frac{[A]}{\Omega} \propto \frac{1}{\Omega}$$

It is worth noting that k_B is *what we measure*. So, we have an effect of the volume such that:

Eq. 37

$$FI(k) = \frac{k_B(s_1)}{k_B(s_2)} = \frac{\Omega(s_2)}{\Omega(s_1)}$$

4.18.4. Modelling of "no adaption", "perfect adaption", "volume-mediated adaption" and " K_{dil} -mediated adaption" models

4.18.4.1. "No adaption" model

In this model, we assume that only the protein synthesis rate s changes upon CHX treatment. Using the same notations as previously, s is changing by a factor α . At equilibrium, the protein level is thus changing as follows:

Eq. 38

$$\frac{[P]_f}{[P]_i} = \frac{\alpha \times s_i}{k} \times \frac{k}{s_i} = \alpha$$

Where $[P]_f$, $[P]_i$ is the final, respectively initial, protein concentration. Similarly, s_f , s_i is the final, respectively initial, protein synthesis rate. In this case, the protein decay rate k is constant.

4.18.4.2. "Perfect adaption" model

In this model, we assume that a process is able to *sense* variation in the protein synthesis rate s mediated by CHX treatment and adapts the decay rate k consistently in order to maintain the initial protein level.

It is worth noting that this model is based on the assumption of *naïve* homeostasis, in which the protein expression system *adjusts* to maintain its set-point while perturbed. In this case, we will have, trivially:

Eq. 39

$$\frac{[P]_f}{[P]_i} = 1$$

and, subsequently:

Eq. 40

$$FI(k) = \frac{k_f}{k_i} = \alpha$$

4.18.4.3. "Volume-mediated adaption" model

As shown in a previous section, when the volume of the cell changes upon drug treatment, the effective protein decay rate k changes due to concentration (of the degradation machinery) changes:

Eq. 41

$$FI(k) = \frac{k_f}{k_i} = \frac{V_{nuc,i}}{V_{nuc,f}}$$

Where k_f, k_i is the final, respectively initial, protein decay rate. Similarly, $V_{nuc,f}, V_{nuc,i}$ is the final, respectively initial, average nucleus volume. In this case, still at equilibrium, the protein level is changing as follows:

Eq. 42

$$\frac{[P]_f}{[P]_i} = \frac{s_f}{s_i} \times \frac{k_i}{k_f} = \alpha \times \frac{V_{nuc,f}}{V_{nuc,i}}$$

4.18.4.4. " K_{dil} -mediated adaption" model

Our passive adaption model does not predict the change in dilution rate but rather incorporates its variations in the predicted variation of the degradation rate, thanks to observations highlighted in chapter 2.4. Nonetheless, these observed variations could be able, in principle, to drive the total protein decay rate k variations. In this section, we remind that $k = K_{deg.} + K_{dil.}$ with $K_{deg.}$ the protein

degradation rate and K_{dil} , the protein dilution rate (the cell division rate). Thus, in a model in which such an adaption is fully driven by K_{dil} , we have:

Eq. 43

$$FI(k) = \frac{k_f}{k_i} = \frac{K_{deg,i} + K_{dil,f}}{K_{deg,i} + K_{dil,i}}$$

And, as before, we can compute the expected protein level fold change:

Eq. 44

$$\frac{[P]_f}{[P]_i} = \frac{s_f}{s_i} \times \frac{k_i}{k_f} = \alpha \times \left(\frac{K_{deg,i} + K_{dil,f}}{K_{deg,i} + K_{dil,i}} \right)^{-1}$$

4.18.4.5. Change in proteome content in the passive adaption model: absolute abundance, relative abundance, and concentration

Here we want to stress how the passive-adaption model should theoretically affect proteome composition. This question can be approached at three different, while interrelated, levels: concentrations, absolute and relative abundances. As shown previously,

Eq. 45

$$t_f = \sqrt{\alpha} \times [P_i]_{t_i}$$

where $[P_i]_{t_f}$ and $[P_i]_{t_i}$ are the protein concentration for protein i at the final and initial time, respectively. From this relation, we can derive the change in absolute protein abundance:

Eq. 46

$$\frac{P_{i,t_f}}{V_f} = \sqrt{\alpha} \times \frac{P_{i,t_i}}{V_i}$$

where V_f and V_i are the cell volume at the final and initial time, respectively. Rearranging the equation, we have:

Eq. 47

$$P_{i,t_f} = \sqrt{\alpha} \times \frac{V_f}{V_i} \times P_{i,t_i}$$

Now, we define the relative abundance of protein i , σ_i as:

Eq. 48

$$\sigma_i = \frac{P_i}{\sum_i P_i}$$

We can compute this relative abundance at the time t_i and t_f :

Eq. 49

$$\begin{aligned} \sigma_{i,t_i} &= \frac{P_{i,t_i}}{\sum_i P_{i,t_i}} \\ \sigma_{i,t_f} &= \frac{P_{i,t_f}}{\sum_i P_{i,t_f}} \\ &= \frac{\sqrt{\alpha} \times \frac{V_f}{V_i} \times P_{i,t_i}}{\sum_i \sqrt{\alpha} \times \frac{V_f}{V_i} \times P_{i,t_i}} \\ &= \frac{P_{i,t_i}}{\sum_i P_{i,t_i}} \\ &= \sigma_{i,t_i} \end{aligned}$$

Finally, we observed that, while the protein concentration and absolute protein abundance change by modulation of α in the passive adaption model, the relative abundance stay constant: the relative proteome composition is not affected by changes in α . It is worth noting here that we assumed — as observed — that the dilution/division rate scales as the protein degradation rate.

0.06643013	0.027722305	0.1074161 4	2344.23306	5367.45407 6	290.4310808	0.0761390 2	0.02699898 2	0.07969383 5	2.3916651 8	0.10555815	586.87301 1	5463.5459 4	4949.5369 3
0.07381125	0.026892168	0.0986169 4	2112.11843 6	5076.74810 9	277.2278548	0.0586685 5	0.02326690 9	0.07172477 5	2.4036285 2	0.10641149	508.88219 4	5160.1903 4	4615.8883 6
0.0820125	0.022293718	0.0960662 1	2025.28914 5	4685.66718 8	305.2069537	0.0726705 3	0.0219857	0.07377248 8	2.3135793 7	0.09999417	457.34138 3	4760.6895 7	5332.0183 6
0.091125	0.024718873	0.0904703 9	2212.72836 7	4948.40450 6	296.3484113	0.0669247 1	0.02445301 3	0.06575152 1	2.2363361 8	0.0945002	454.43446 5	5023.0185 2	5101.5706 5
0.10125	0.029182646	0.0922613 6	1969.42427 8	4262.61101 1	287.312864	0.0541294 2	0.02097121 5	0.06307871 8	2.1643944 7	0.0893922	399.32164 4	4328.1567 3	4870.0408 8
0.1125	0.019827151	0.0836383 3	1991.19578 6	4210.97653 1	304.9717958	0.0581488 3	0.01954645 3	0.06381118 1	2.1147978 3	0.08587572	357.10861 7	4269.6763 7	5325.8571 7
0.125	0.018627996	0.0678553 3	1973.05730 2	3706.55095 3	334.2126211	0.0459088 3	0.02112878 2	0.04922732 9	1.8785825 2	0.06918328	254.35359 5	3748.4691 6	6109.9023 6
0.13286025	0.020888578	0.0735932 1	2086.95697 5	4147.87895 3	270.2006634	0.0530930 1	0.01757345 9	0.05270463 2	1.9875249	0.07687043	308.99985 1	4198.7549 1	4441.4994 9
0.1476225	0.022031869	0.0773580 1	2097.91033	4030.99595	282.6928978	0.0489442 1	0.01972035 3	0.05532614 4	1.9214338 6	0.07220462	315.85026 2	4082.9675 9	4753.0496 9
0.164025	0.016549324	0.0639603 2	1897.73704 3	3513.60159 8	290.1652414	0.0419651 7	0.01721483 4	0.04741100 1	1.8514691 5	0.06727313	227.12674 6	3551.0567 9	4942.7435 9
0.18225	0.015280162	0.0636231 3	1986.57922 7	3608.36628 9	272.6977016	0.0415975	0.01486308 8	0.04834296 7	1.8163717	0.06480229	232.00994 1	3646.6288 8	4503.2101 7
0.2025	0.017435252	0.0624507 3	1917.46887 9	3438.76760 9	296.1640245	0.0408364 1	0.01426364 9	0.04501547 5	1.7933890 1	0.06318542	216.98879	3474.5598 7	5096.8101 2
0.225	0.011150268	0.0574944 3	1959.74508 1	3290.28769 3	288.82912	0.0436484 4	0.01000004 1	0.04634416 4	1.6789365 7	0.05514629	190.98595 7	3321.8165 6	4908.6432
0.25	0.009103854	0.0476188 4	1897.48282 1	3013.82769 1	290.2918306	0.0356559 3	0.00948382 4	0.03851498 1	1.5883293 7	0.04879715	144.65396 7	3037.7468 5	4945.9784 7
0.2657205	0.00647256	0.0392705 6	1849.78088 7	2885.08306 4	296.6274585	0.0277445 4	0.00647998 1	0.03279800 2	1.5596890 9	0.046793	114.04038 4	2903.9662	5108.7779 4
0.295245	0.004880905	0.0364473 3	1852.42564 2	2843.94202 1	266.3993089	0.0304831 5	0.00474334 1	0.03156642	1.535253	0.04508409	104.28373 3	2861.2177	4348.1011 7
0.32805	0.005583095	0.0360650 2	1859.72535 3	2666.70772 1	299.1432475	0.0233576 3	0.00499537 1	0.03048191 7	1.4339255 6	0.03800819	96.752936 9	2682.7368 6	5173.9092 4
0.3645	0.006637643	0.0285095 9	1804.88985 2	2526.53267 5	299.0863522	0.0266186 4	0.00523259 4	0.02187194 6	1.3998265 2	0.03563071	72.372666 4	2538.5377 4	5172.4332 4
0.405	0.007020548	0.0320298 6	1783.86910 9	2431.75973 2	298.4814323	0.0215370 9	0.00690128 4	0.02500930 9	1.3631940 4	0.03307868	78.304711 5	2444.7412 2	5156.7488 5
0.45	0.005782244	0.0314949 8	1824.34673 3	2406.97676 3	300.271976	0.0266984 6	0.00532141 6	0.02571273 4	1.3193636 5	0.03002803	76.205605	2419.6113 8	5203.2201 7
0.5	0.004449788	0.0247864 1	1849.1169	2351.55174 4	299.8302663	0.0148963 5	0.00506340 5	0.02033662 6	1.2717161 1	0.0267152	58.527321 9	2361.2661 7	5191.7432 4

Table 2. Measurements from steady states induced by 48 h MYCi treatment

Concentration on μM	K_{sw} Nuclear growth h^{-1}	k h^{-1}	mOrange2 mean intensity A.U.	sGFP mean intensity A.U.	Nuclear size μm^2	K_{sw} h^{-1}	K_{sw} cell division h^{-1}	K_{sw} (Calculated from k and K_{sw}) h^{-1}	G/R Ratio A.U.	k Theoretical h^{-1}	s A.U.	[P] A.U.	Volume A.U.
0	0.03409608	0.17481013	2944.96673	9239.41324	319.029009	0.11107388	0.04121622	0.14071405	3.13735742	0.159207995	1662.20025	9508.60374	5698.29937
0.2657205	0.03760331	0.17096215	3129.89278	9771.85605	334.008265	0.11236905	0.04547835	0.13358884	3.12210569	0.158101245	1718.21958	10050.2923	6104.29931
0.295245	0.0489356	0.17532502	2793.58576	8637.33835	376.562093	0.1042335	0.04852256	0.12638943	3.0918465	0.155906648	1558.59187	8889.72861	7307.26571
0.32805	0.02944844	0.1810917	2902.01182	8923.28693	327.871604	0.11803688	0.03344809	0.15164326	3.07486236	0.154675532	1664.70518	9192.60912	5936.84497
0.3645	0.04654124	0.17768648	2757.29268	8476.19777	322.130342	0.11595817	0.04922505	0.13114524	3.07410158	0.154620397	1550.70818	8727.21539	5781.59213
0.405	0.03357315	0.18129613	3123.95845	9987.18874	304.575301	0.11228885	0.05437504	0.14772298	3.19696594	0.163537336	1865.34894	10288.9618	5315.47432
0.45	0.0492767	0.17546204	2951.67	8696.99394	347.572003	0.09877307	0.04506295	0.12618534	2.94646554	0.145384433	1570.61791	8951.32599	6479.88323
0.5	0.0495605	0.17819271	2855.76711	8551.91317	335.935359	0.11001505	0.05484646	0.12863221	2.99461155	0.148865104	1569.14621	8805.8946	6157.20449
0.531441	0.0608739	0.1639344	2707.8575	8058.27782	378.691928	0.10498782	0.06204287	0.1030605	2.97588696	0.147510959	1357.12264	8278.44931	7369.34811
0.59049	0.04524929	0.17861871	2879.03612	8871.30692	306.974241	0.11016647	0.05319131	0.13336942	3.08134617	0.155145461	1631.75409	9135.40383	5378.39757
0.6561	0.04516936	0.18175558	2955.68706	8984.67485	329.777104	0.11355652	0.04523814	0.13658622	3.03979233	0.152134994	1682.48306	9256.84399	5988.67506
0.729	0.064715	0.17545032	2786.48579	8417.49229	335.850158	0.10338907	0.05923052	0.11073532	3.02082728	0.150762004	1520.03743	8663.63425	6154.86223
0.81	0.04726093	0.18088839	2997.22727	8994.29046	356.868155	0.10896889	0.0512072	0.14082746	3.00087035	0.149317867	1744.7538	9276.24406	6741.58002
0.9	0.0323092	0.18031784	3007.39509	8969.93817	325.188043	0.11609354	0.03506619	0.14800864	2.98262713	0.147998333	1666.04877	9239.51149	5864.10654
1	0.04294238	0.18645856	2628.07702	8032.78092	388.418606	0.1170896	0.04934941	0.14351617	3.05652417	0.153346817	1544.3264	8282.41104	7655.08536
1.062882	0.03328674	0.17535397	2778.44061	8209.16973	348.11272	0.11581947	0.04353975	0.14206722	2.95459608	0.145971946	1481.58111	8449.08814	6495.01023
1.18098	0.03729604	0.18059481	2862.12901	8392.59187	375.145508	0.11053081	0.03851926	0.14329877	2.93228985	0.144360366	1561.27855	8645.20162	7266.0708
1.3122	0.0390232	0.17350958	3047.82007	9125.12928	355.386616	0.10931824	0.0424271	0.13448638	2.99398556	0.148819823	1629.08353	9389.01217	6699.64208
1.458	0.03103586	0.18113281	3079.1496	8929.29118	348.708945	0.1106847	0.03209405	0.15009695	2.89992119	0.142023298	1666.21459	9198.85578	6511.70371
1.62	0.04033916	0.18638811	2877.6135	9045.80183	325.384601	0.12108502	0.04501922	0.14604895	3.14350827	0.159654447	1738.40589	9326.80681	5869.42413
1.8	0.04874034	0.18202759	2903.42065	8520.71947	319.526336	0.10994344	0.04436928	0.13328724	2.93471753	0.14453572	1598.06031	8779.22047	5711.62899
2	0.03913274	0.18000936	3139.28602	9187.08162	318.923761	0.12125795	0.04744184	0.14087662	2.92648761	0.143941304	1703.37605	9462.70839	5695.4798
2.125764	0.04051394	0.17075904	2835.80956	8350.71953	385.353353	0.10973323	0.03557155	0.1302451	2.94473918	0.145259701	1466.54351	8588.37968	7564.6478
2.36196	0.04356344	0.16534473	2586.34794	7794.21949	358.567363	0.09511062	0.04039476	0.12178128	3.01360052	0.150238978	1324.24729	8009.00833	6789.78677
2.6244	0.03517529	0.17090273	3001.37253	8932.5829	367.571662	0.10681248	0.04827381	0.13572744	2.97616601	0.147531135	1570.08623	9187.0167	7047.14218
2.916	0.04434618	0.1752903	2685.78113	7951.96856	351.342567	0.09835309	0.0458927	0.13094413	2.96076566	0.146417836	1434.62594	8184.28572	6585.61223
3.24	0.0577738	0.16685543	2734.99317	8392.07614	407.883651	0.09777067	0.0621029	0.10908164	3.06840845	0.154207841	1439.20377	8625.45339	8237.67108
3.6	0.05068506	0.16736734	2751.39169	8431.7511	368.745279	0.09951053	0.05684978	0.11668228	3.06454044	0.153927575	1450.56453	8666.95106	7080.92026
4	0.04534994	0.17517814	2791.71068	8334.30141	374.241214	0.10052178	0.05106415	0.12982821	2.98537433	0.148197002	1502.61375	8577.63265	7239.81418
4.251528	0.05257147	0.16556208	2645.34003	8054.29662	376.812921	0.09881616	0.06251146	0.11299061	3.04471128	0.152491205	1370.28189	8276.54431	7314.56796
4.72392	0.05427329	0.1774849	2920.21172	9003.17769	359.128648	0.10765435	0.06009843	0.12321161	3.08305648	0.155269432	1645.19615	9269.49904	6805.73564
5.2488	0.05447502	0.18182802	2714.41123	8275.05843	331.475158	0.10820364	0.05240929	0.12735301	3.04856476	0.152770288	1550.23506	8525.83135	6034.98896
5.832	0.05122574	0.17415221	3173.68974	9593.3379	338.132927	0.10895329	0.05317872	0.12292647	3.02277118	0.150902706	1719.19368	9871.78806	6217.7205
6.48	0.05122793	0.18431388	2690.0467	8274.50506	356.865496	0.11475253	0.05138406	0.13308595	3.07597079	0.154755862	1571.95585	8528.68942	6741.50466
7.2	0.04772766	0.1776958	2870.72841	8709.60814	345.916963	0.10891587	0.05257578	0.12996814	3.03393665	0.151711002	1593.49629	8967.55161	6433.65532
8	0.04576252	0.17666049	3063.56402	9293.70953	339.39064	0.11795911	0.05078263	0.13089797	3.03362668	0.151688559	1690.17244	9567.34808	6252.44371
8.503056	0.05369768	0.17841803	2983.64239	8912.03789	309.540532	0.106863	0.05021409	0.12472036	2.98696584	0.148312101	1637.35108	9177.04926	5445.98308
9.44784	0.05236654	0.17638044	2776.63726	8345.27934	359.9613	0.09968593	0.05834344	0.12401391	3.00553459	0.149655323	1515.21443	8590.60336	6829.41837
10.4976	0.05627832	0.17704293	3107.08341	9330.29187	390.496399	0.09657897	0.05344679	0.12076461	3.00291001	0.149464532	1700.60392	9605.60223	7716.59222

11.664	0.05128349	0.17886213	2712.65085	8385.06471	350.091231	0.10269199	0.04953611	0.12757864	3.09109618	0.155852251	1544.47923	8635.02646	6550.46075
12.96	0.0434704	0.18323183	2582.15498	7751.82928	335.988493	0.11935409	0.04708521	0.13976143	3.00207747	0.149405198	1463.75838	7988.55959	6158.66536
14.4	0.05182972	0.17814465	2931.71968	8966.00349	381.798538	0.105003	0.0512589	0.12631493	3.05827449	0.153473614	1644.66902	9232.21108	7460.21581
16	0.03537981	0.17924369	3201.25717	9275.55811	347.56711	0.1167625	0.03821259	0.14386388	2.89747359	0.141846649	1712.25324	9552.65565	6479.74639
17.006112	0.03342346	0.18669554	3072.16867	10138.4053	284.732292	0.11865664	0.04165779	0.15327208	3.30008094	0.171040923	1951.69107	10453.8711	4804.5762
18.89568	0.03573017	0.19034473	2877.12175	8858.27922	300.896563	0.1153512	0.0422526	0.15461456	3.0788684	0.15496587	1739.61761	9139.30034	5219.46322
20.9952	0.04197654	0.18274356	2826.72804	8797.20244	315.966371	0.1074943	0.04001725	0.14076702	3.11215027	0.15737904	1656.59615	9065.14112	5616.44218
23.328	0.02766822	0.17914519	2589.66138	7925.01277	353.333694	0.11623027	0.03545867	0.15147696	3.06025059	0.153616773	1462.11749	8161.63409	6641.6744
25.92	0.02720313	0.18328178	2858.17411	8824.49511	320.725869	0.11228126	0.03834669	0.15607865	3.08745891	0.155588561	1666.77489	9094.05664	5743.82216
28.8	0.03925959	0.17635465	2839.19261	8340.06952	334.405179	0.10899928	0.03974581	0.13709506	2.93747929	0.144735217	1514.04076	8585.20453	6115.18349
32	0.02619278	0.16737121	2677.60612	7585.0288	325.763451	0.11126939	0.03226077	0.14117843	2.83276497	0.137180178	1304.92885	7796.61471	5879.67791
34.012224	0.03459638	0.16950995	2688.29864	7788.61155	338.659094	0.10990345	0.03175639	0.13491357	2.89722705	0.141828856	1357.54636	8008.65275	6232.23919
37.79136	0.04544649	0.16700965	2557.16919	7202.12152	336.831523	0.10545403	0.0342644	0.12156316	2.81644309	0.136004244	1236.3043	7402.59215	6181.85898
41.9904	0.01725609	0.15908228	2528.45847	7265.8466	317.188605	0.10856569	0.02299111	0.14182619	2.87362703	0.140126126	1186.51377	7458.49117	5649.06233
46.656	0.02178437	0.16022448	2427.62706	6551.82466	363.809631	0.10559349	0.02546281	0.13844012	2.69885962	0.12754606	1077.79567	6726.78511	6939.23007
51.84	0.02515871	0.15071439	2371.533	5889.43088	358.476567	0.09819668	0.01992364	0.12555568	2.48338559	0.112106639	909.918244	6037.36788	6787.20797
57.6	0.01572075	0.14243941	2281.13939	5613.6756	356.908166	0.09548098	0.00762721	0.12671866	2.46090862	0.11050057	818.591293	5746.94371	6742.7138
64	0.01458181	0.12406032	2092.88306	4658.2775	352.367584	0.07967433	0.01240641	0.10947851	2.22577056	0.093749487	589.856616	4754.5954	6614.45283

Table 3. SNAP measurements from the short-lived Timer

	$K_{deg} \text{ h}^{-1} (\pm \text{ std})$	$K_{dil} \text{ h}^{-1} (\text{Theoretical})$	$k \text{ h}^{-1} (\pm \text{ std})$	sfGFP mean intensity normalized
Control	0.126 ± 0.033	0.045	0.171 ± 0.038	1
CHX	0.084 ± 0.033	0.027	0.111 ± 0.032	0.412
5h release	0.079 ± 0.026	0.041	0.120 ± 0.028	0.376
7h release	0.093 ± 0.024	0.042	0.135 ± 0.029	0.491
9h release	0.109 ± 0.025	0.050	0.159 ± 0.035	0.585
11h release	0.120 ± 0.036	0.041	0.161 ± 0.032	0.867

- $K_{dil} \text{ h}^{-1} (\text{Theoretical})$ was calculated from k and K_{deg} .

Table 4. SNAP measurements from the long-lived Timer

	$K_{deg} \text{ h}^{-1} (\pm \text{ std})$	$K_{dil} \text{ h}^{-1} (\text{Theoretical})$	$k \text{ h}^{-1} (\pm \text{ std})$
Control	0.0131 ± 0.0076	0.036145	0.047448 ± 0.027559
CHX	0.0047 ± 0.0060	0.022733	0.039721 ± 0.026256
8h release	0.0035 ± 0.0996	0.064034	0.058203 ± 0.050095
10h release	0.0151 ± 0.0175	0.042120	0.055997 ± 0.024568
12h release	0.0112 ± 0.0074	0.041752	0.057039 ± 0.026636
14h release	0.0133 ± 0.0114	0.038112	0.050826 ± 0.022869
16h release	0.0131 ± 0.5000	0.040197	0.054074 ± 0.018498

- $K_{dil} \text{ h}^{-1} (\text{Theoretical})$ was calculated from k and K_{deg} .

6. Supplementary figures

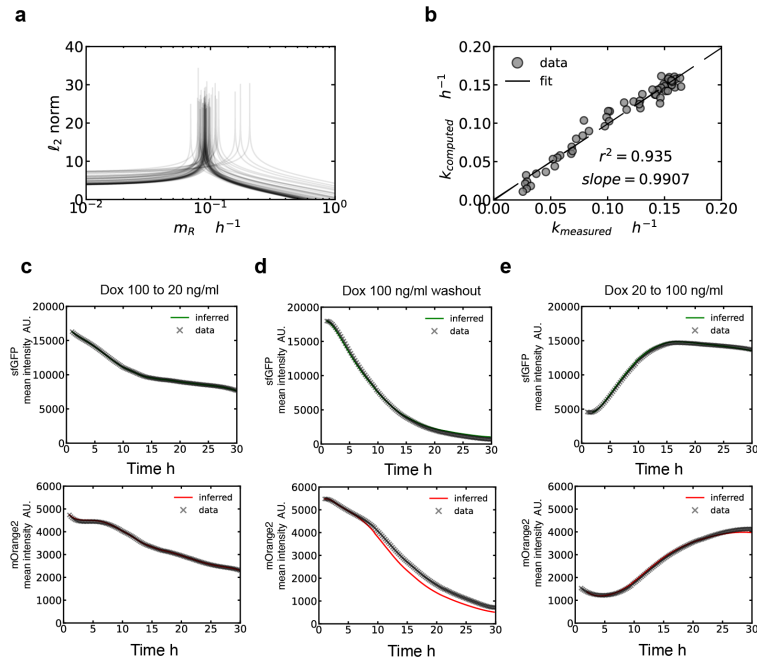


Figure S1 | Calculation of Timer constants and validation of Timer modelling.

a, Calculate mOrange2 maturation rate by optimizing a cost function for CHX-induced steady-states. Each line is an optimization process for a CHX steady-state in Table 1. ℓ_2 is the function to maximize. **b**, Correlation between the experimental k measured by SNAP pulse-chase (Fig. 3a, b, Table 1.), and k calculated from Eq. 4 by using Timer fluorescence intensity (Table 1) and estimated m_G and m_R . Retrodiction of Timer fluorescent traces using modelled s and k for **c**, Dox 100 to 20 ng/ml (Fig. 2e), **d**, Dox 100 ng/ml washout (Fig. 2f), and **e**, Dox 20 to 100 ng/ml (Fig. 2g).

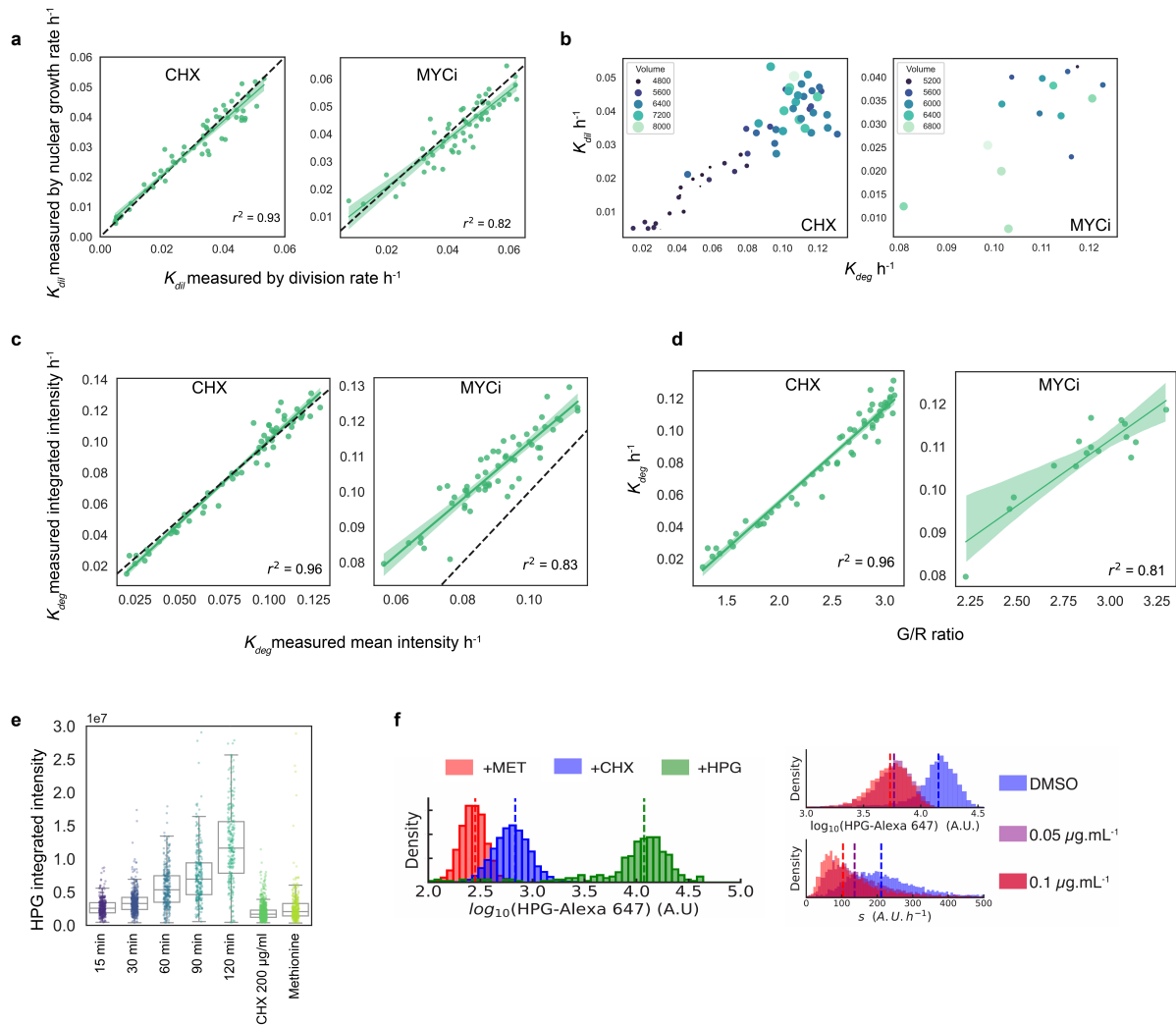


Figure S2 | Validation of calculations for protein degradation adaption to CHX and MYCi treatment.
a, Correlation between K_{dil} measured by division rate and K_{dil} measured by the growth rate of the nucleus. Each data point is a different CHX or MYCi concentration as in Fig. 3e and Fig. 4e. **b**, Correlation between K_{dil} , K_{deg} and mean nuclear volume estimated from the nuclear area after CHX and MYCi prolonged treatment. The unit of nuclear volume is arbitrary. Only MYCi concentrations above 15 μM are plotted. **c**, For CHX and MYCi prolonged treated cells, the correlation between two methods of calculating K_{deg} , either by the exponential fitting of SNAP mean intensity to calculate k , then subtract K_{dil} (from Fig. 3e and Fig. 4e), or by the exponential fitting of SNAP integrated intensity per cell lineage. **d**, Correlation between G/R ratio and degradation rate for CHX or subset of MYCi prolonged treated groups. MYCi uses data from concentrations above 15 μM . **e**, HPG labelling newly synthesized protein for various incubation times. Mean cellular fluorescence intensities are plotted. **f**, HPG labelling of CHX prolonged treated cells analysed by flow cytometry. On the left, +CHX is the condition where CHX 200 $\mu\text{g}/\text{ml}$ was added to cells 30 min before and during HPG labelling as the negative control. +MET is the negative control where methionine instead of HPG was supplemented to the medium. For **a**, **c**, **d**, the dash line is $y = x$, shading: 95% CI.

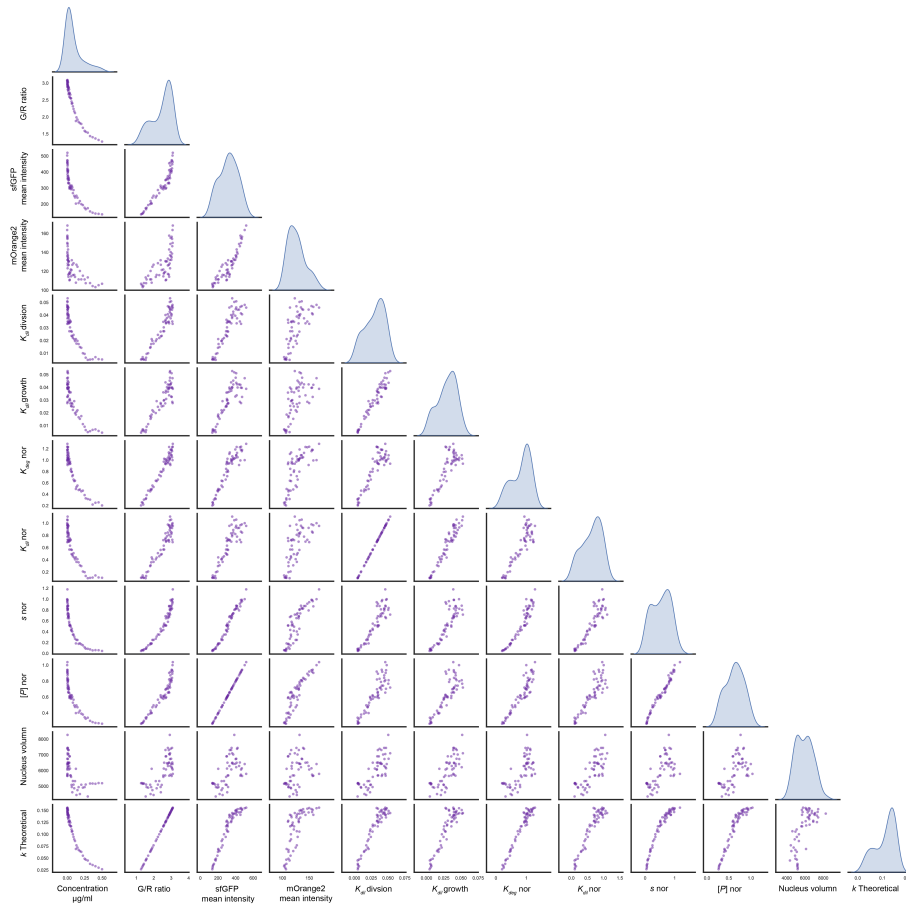
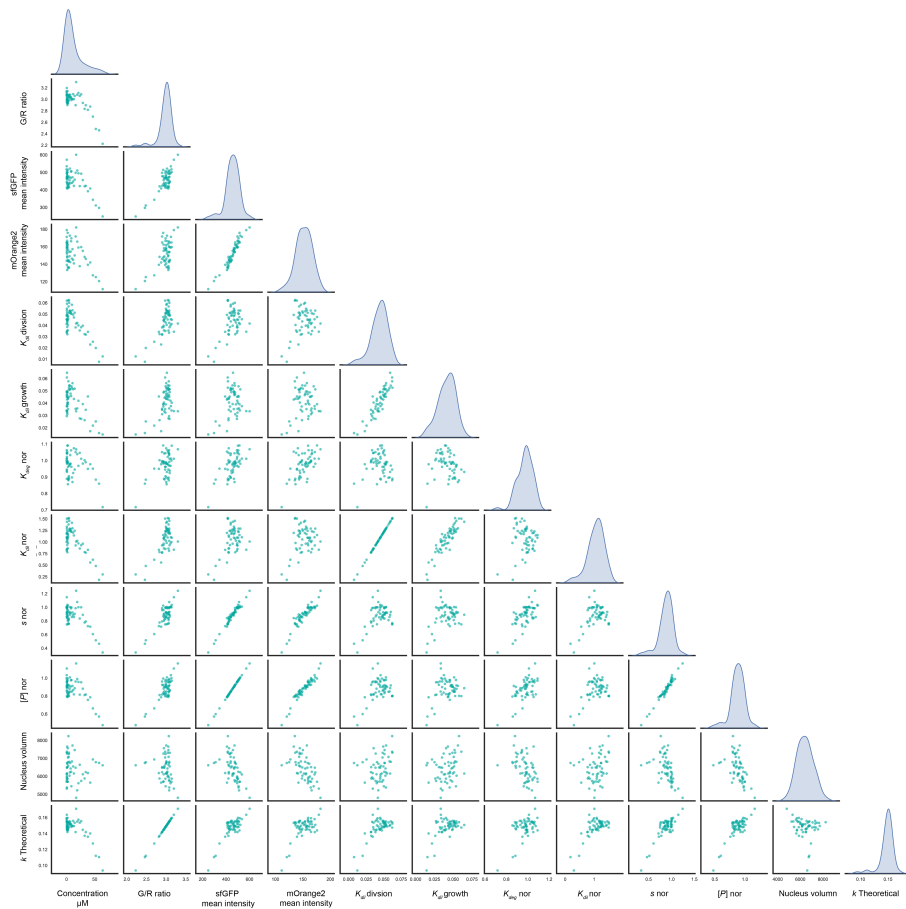
a**b**

Figure S3 | Correlations between all the calculations from CHX and MYCi steady-states.

Pairplots of all parameters of steady-states resulted from **a**, CHX and **b**, MYCi prolonged treatment. 'nor' signifies the fold change relative to control without drugs. 'Concentration' is the concentration of CHX or MYCi. K Theoretical is calculated from the G/R ratio using Eq. 4.

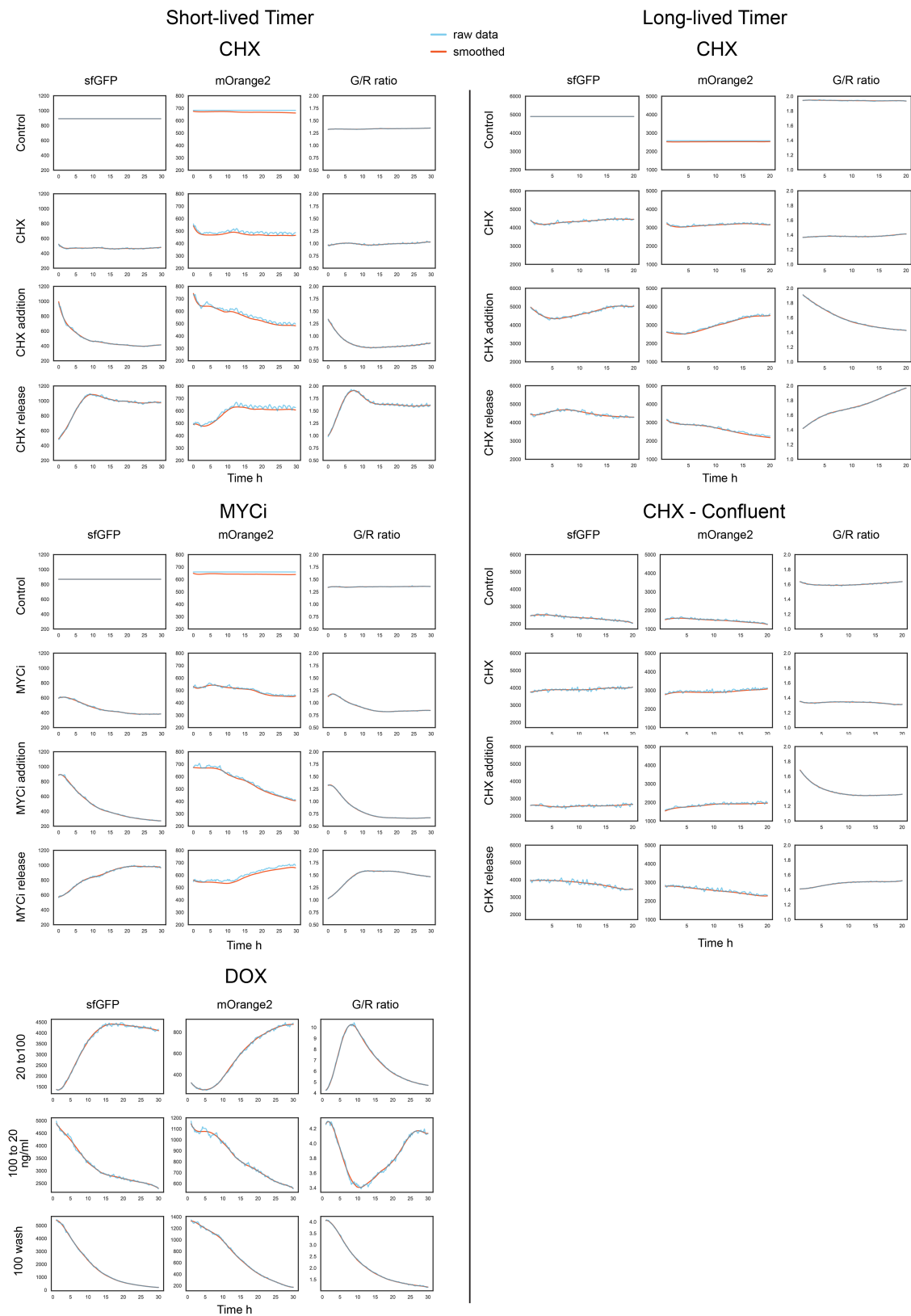


Figure S4 | Pre-processing of Timer traces for modelling.
 sfGFP and mOrange2 traces were smoothed with the Savitzky-Golay filter (window length: 100, polynomial order: 6) prior to modelling.

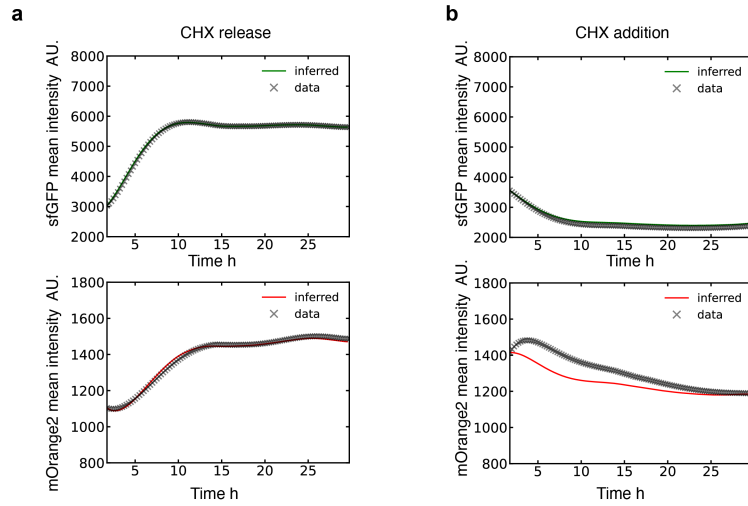


Figure S5 | Retrodiction of Timer traces from modelled s and k for CHX addition and release.

Retrodiction of Timer fluorescent traces using modelled s and k (from Fig. 6a, b) for **a**, CHX release and **b**, CHX addition.

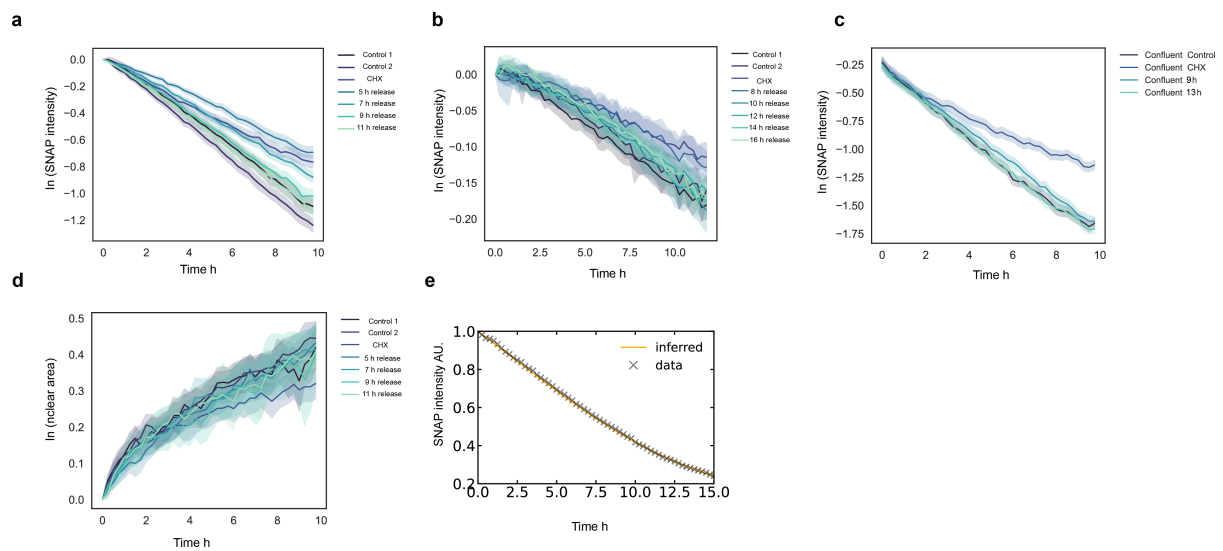


Figure S6 | Validation of degradation dynamics during CHX release.

Pulse-chase labelling of SNAP to calculate K_{deg} at different time points after CHX release. Means of integrated SNAP intensity per lineage are plotted from **a**, short-lived Timer (Fig. 7a), **b**, long-lived Timer (Fig. 7b), and **c**, short-lived Timer in confluent culture (Fig. 7c). **d**, Nuclear area over time for short-lived Timer after CHX release (Fig. 7d). Mean of the integrated area of each lineage is plotted. **e**, Retrodiction of short-lived SNAP traces using modelled k (from Fig. 7d). For **a,b,c,d**, time after release labelled in figure legends is pseudo-time calculated by adding half of the length of the SNAP chase phase to the time that had passed after CHX release at the start of the SNAP chase. Shading: 95% CI (**a, b, c, d**).

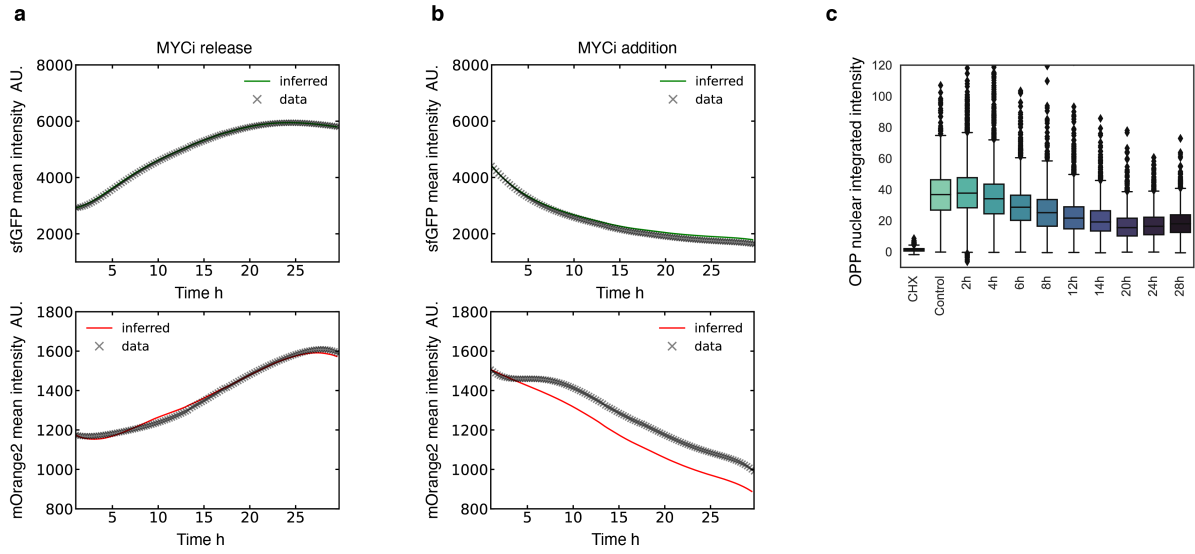


Figure S7 | Dynamics of synthesis and degradation during MYCi and MYCi release treatment.

Retrodiction of Timer fluorescent traces using modelled s and k for **a**, MYCi release (Fig. 8e) and **b**, MYCi addition (Fig. 8d). **c**, OPP labelling newly synthesized proteins in mESC cells at indicated hours after MYCi addition. Subtract background estimated from CHX, which is added at 100 $\mu\text{g}/\text{ml}$, 1 h before OPP labelling.

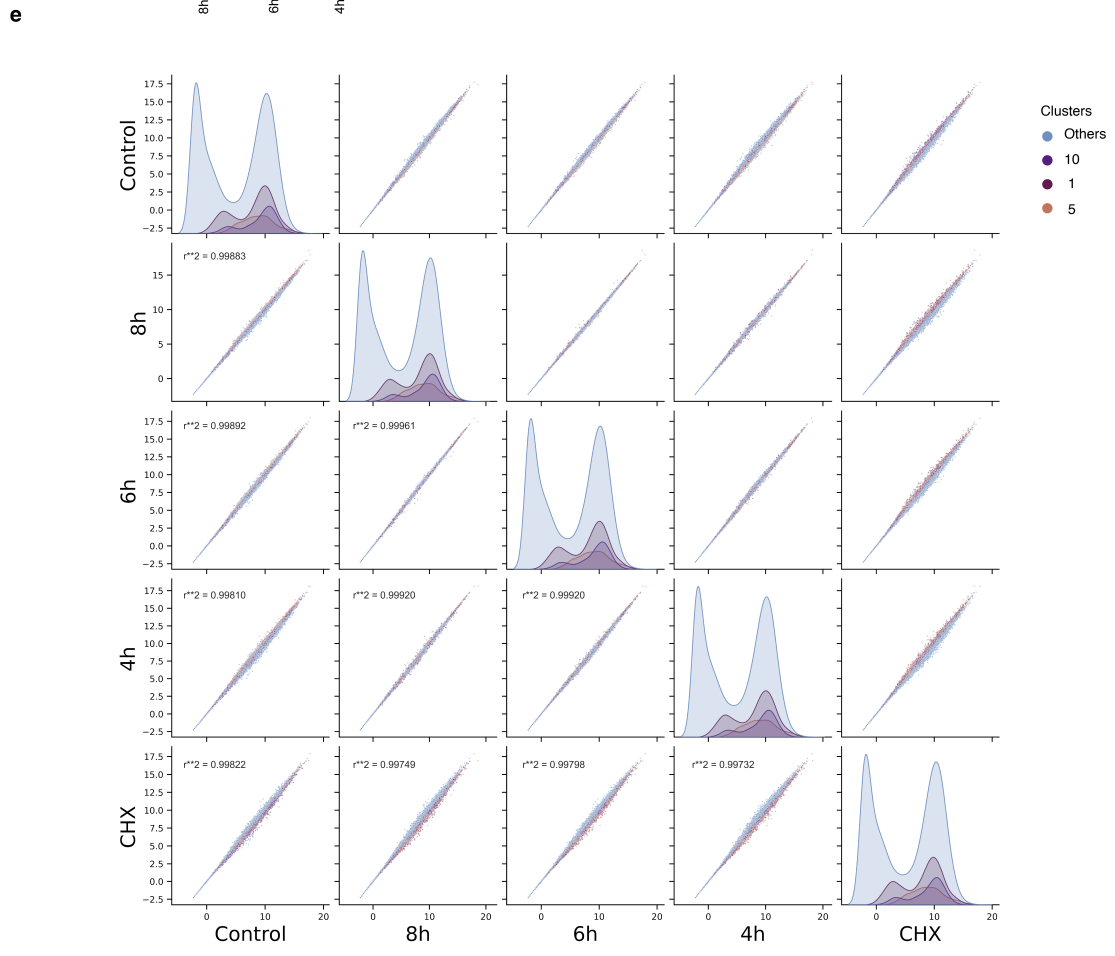
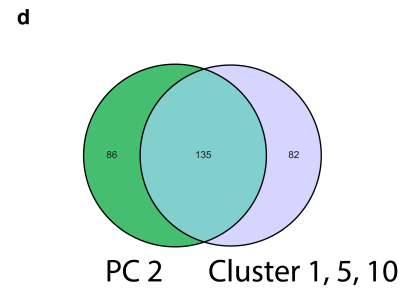
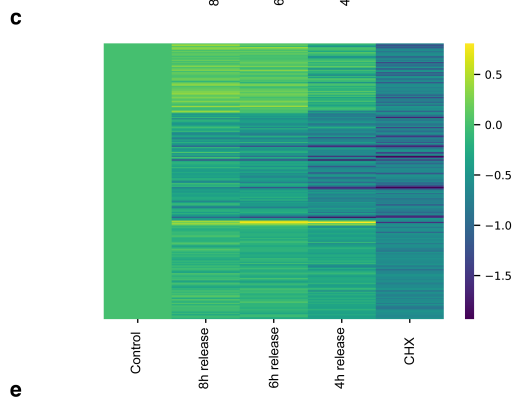
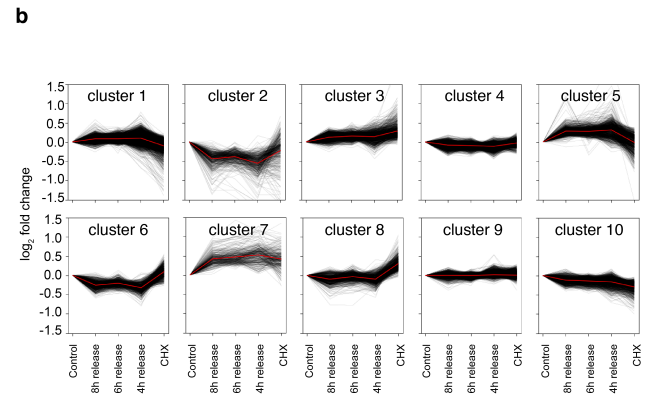
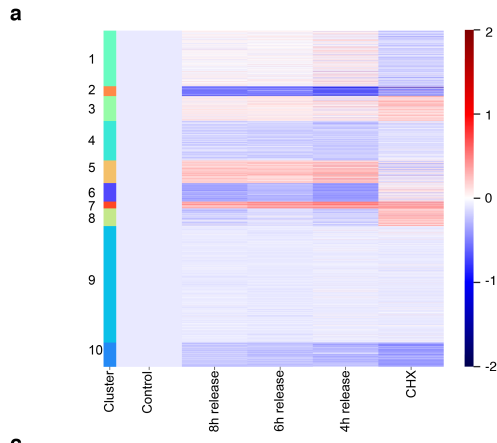


Figure S8 | Clustering genes based on their dynamics during CHX release.

a, Heatmap of log 2 fold change (to Control) of genes expression profile, clustered into ten groups based on their dynamics during CHX release (Fig. 9b). **b**, Log 2-fold change of genes across time after CHX release in all clusters. The red line is the mean for each condition (Fig. 9c, S8a). **c**, Heatmap of log 2 fold change (to Control) of genes which contribute the most variance on the PC2 axis (Fig. 9a), clustered by their dynamics. Genes are filtered by log 2 fold change (Control vs CHX) > 0.5. **d**, Overlapping between genes from Cluster 1,5, 10 and genes contributing most variance on the PC2 axis. All genes are filtered by log 2 fold change (Control vs CHX) > 0.5. **e**, Correlation of RNA raw reads between different conditions. Genes belonging to cluster 1, 5, 10 are highlighted. For **a**, **b**, **c**, **d**, **e**, means of replicates per condition are plotted.

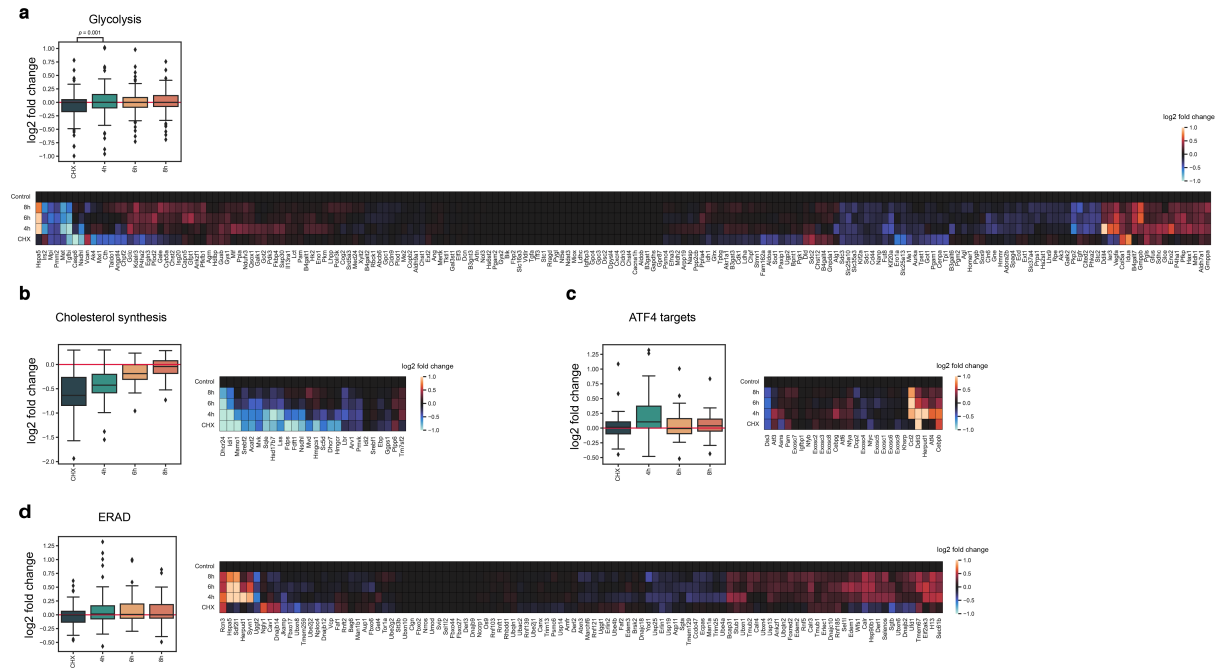
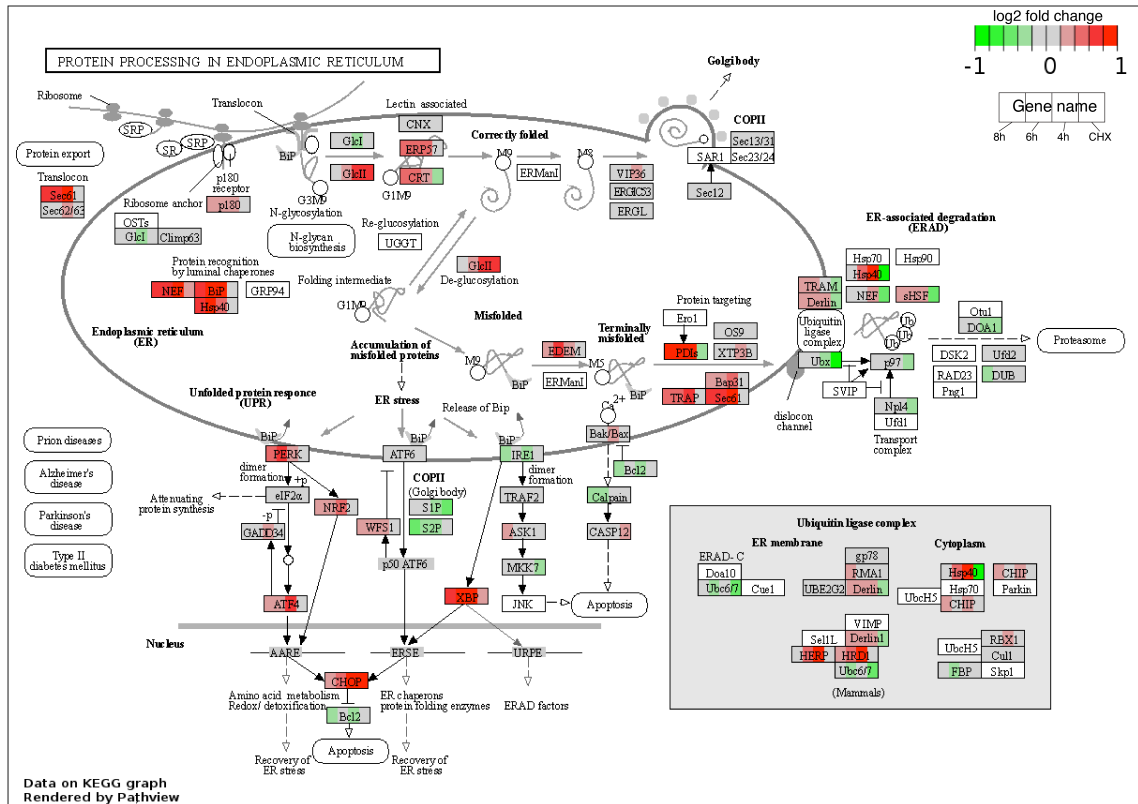


Figure S9 | Dynamics of cellular pathways during CHX release.

a, b, c, d, The expression profile of selected gene groups during CHX release. Log 2 fold change of all genes are normalized to the control. The red line in the boxplot is the expression level of the control. Heatmaps show the relative expression levels of individual genes, which are clustered according to their dynamics across conditions. For log 2 fold changes above 1 or belong -1, colours are set to the maximum or the minimal display range indicated by the colour bar. For **a**, test statistic: T-test. Means of replicates per condition were used for generating all the plots.

a



b

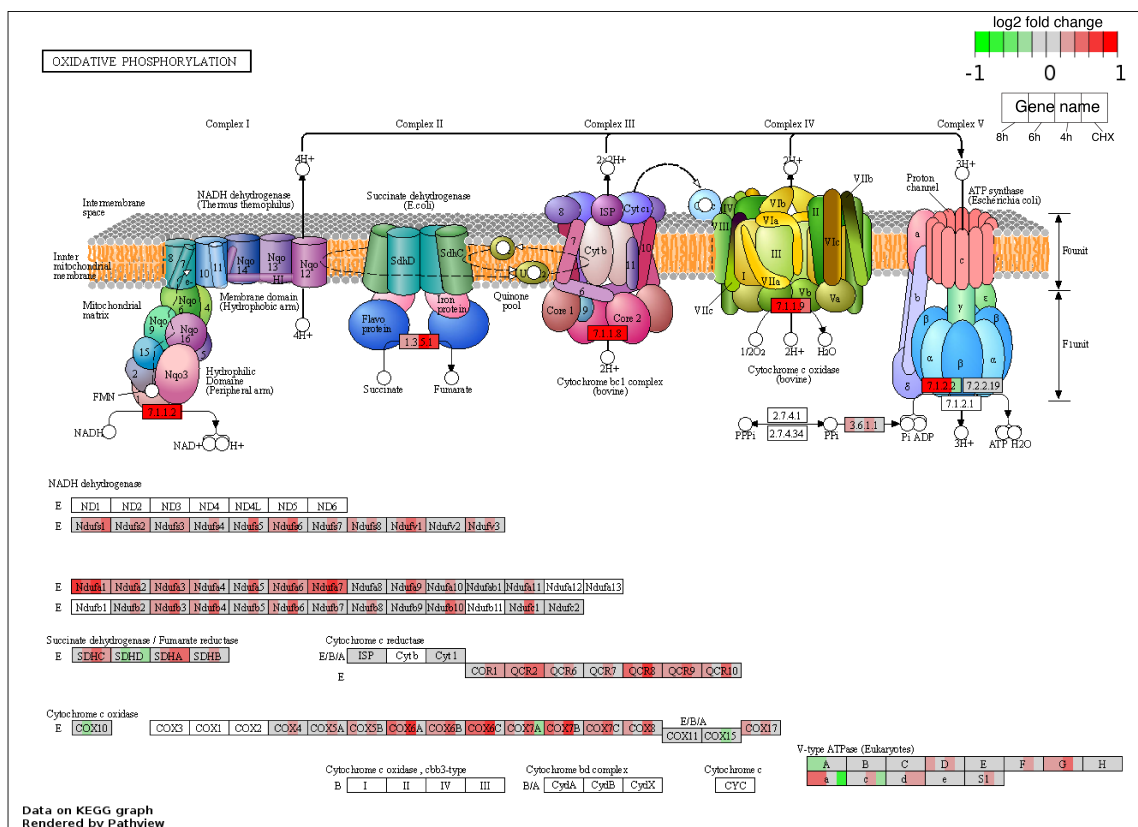
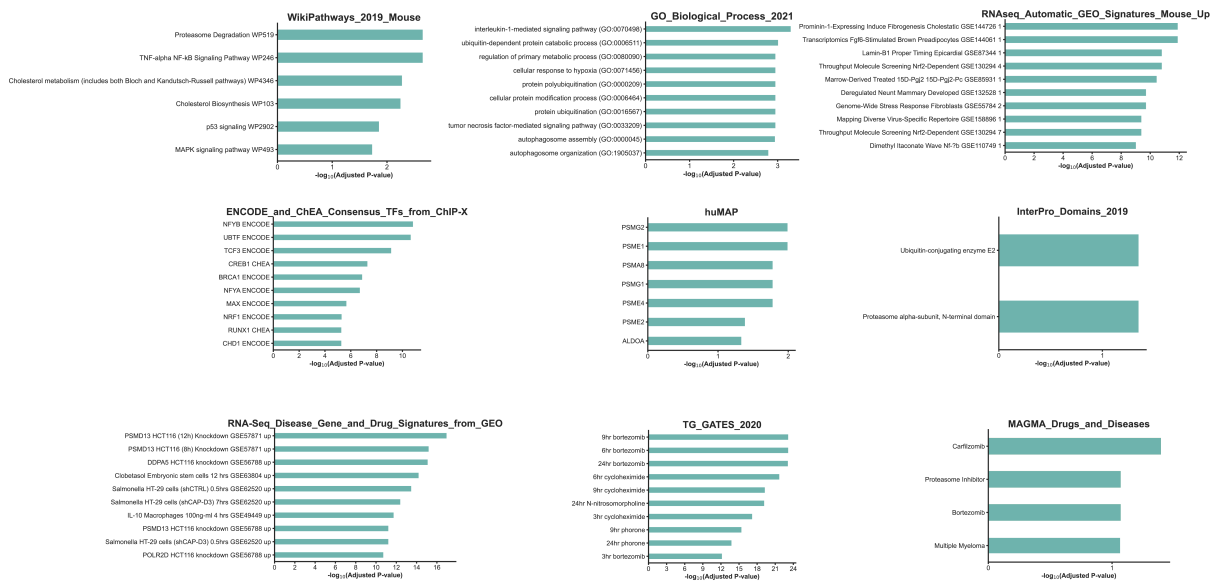


Figure S10 | Transcription dynamics for selected pathways during CHX release. Log 2 fold change (to Control) of genes mapped on a, 'protein processing in ER' and b, 'Oxidative phosphorylation' pathways. The symbol of each gene is divided into four boxes, from right to left, corresponding to CHX, 4 h, 6 h, and 8 h after CHX release. The colour of each box indicates log 2 fold change. Figures are generated by Pathview (Luo et al., 2017; Luo and Brouwer, 2013).

Cluster 1, 10 'Revival genes'



Cluster 5 'Induced genes'

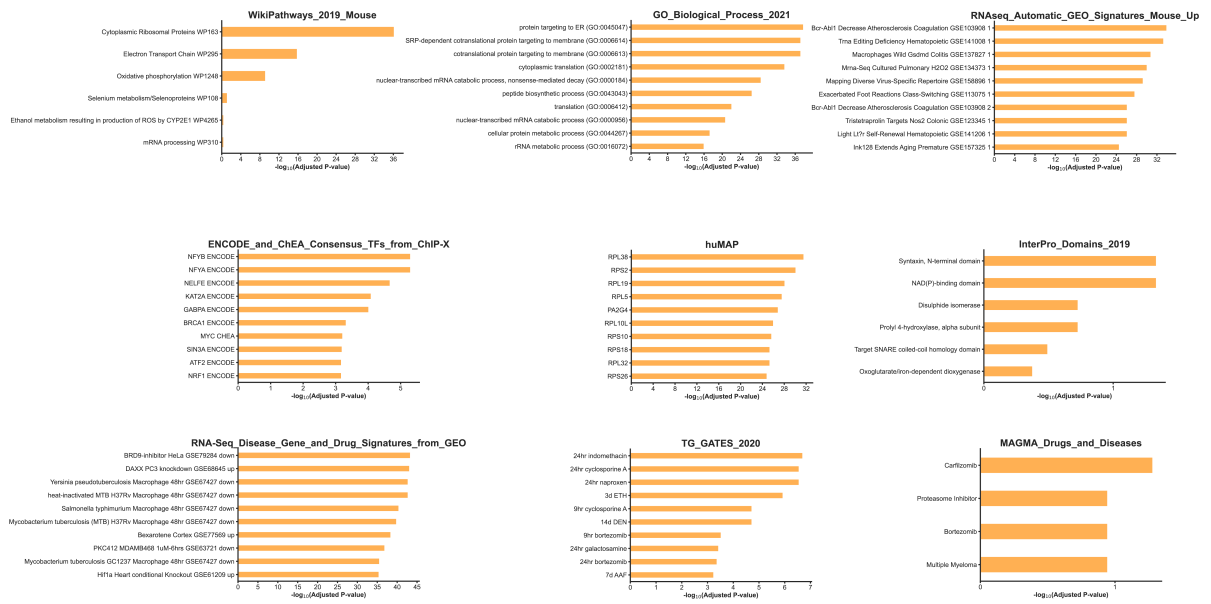


Figure S11 | Over-representation assay for clustered genes.

Gene sets from selected libraries were tested for over-representation within cluster 1, 10 and cluster 5, respectively.

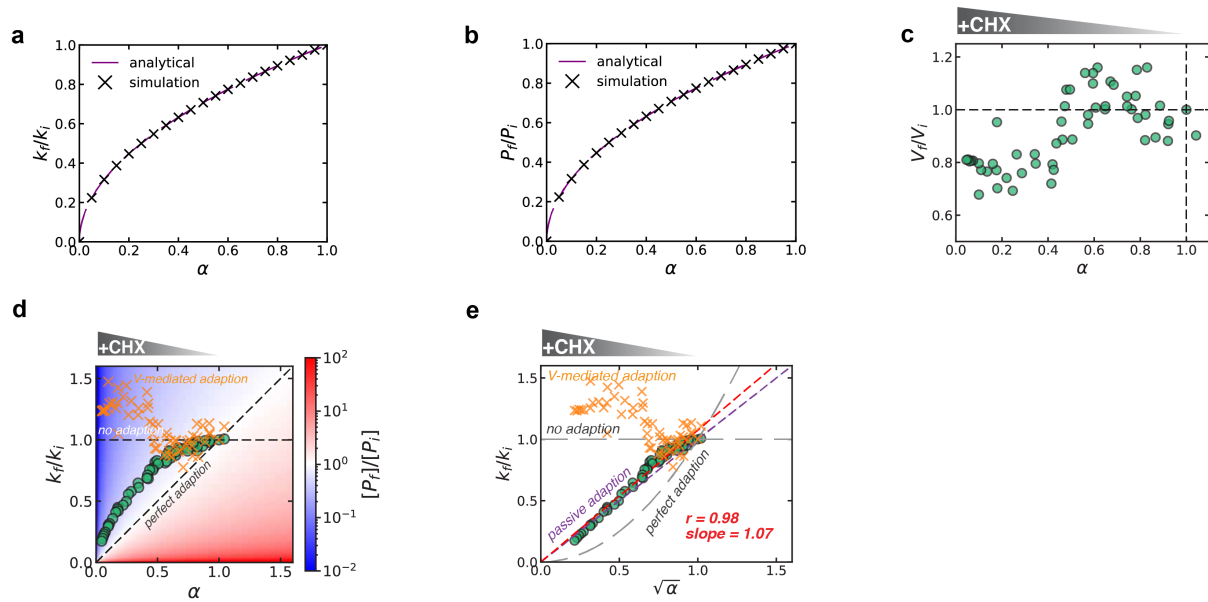


Figure S12 | The calculation of the proteostasis relations in the passive adaption model.

a, b, The result from the computer aided integration of differential equations (Eq. 19 and Eq. 20), which describe the concentration of the Timer and protein degradation machinery, is compared with the analytical solution (Eq. 21 to Eq. 28) at steady states. The fold change of **a**, k (k_f/k_i) and **b**, the Timer concentration (P_f/P_i) derived from both methods are plotted against the predetermined synthesis fold change α . **c,** The nuclear volume fold change (V_f/V_i) versus α for CHX prolonged treated-cells. Nuclear volume was inferred from the segmented nuclear area. The relation between k_f/k_i and **d**, α , or **e**, $\sqrt{\alpha}$ is plotted, while the change in volume caused by the CHX treatment is taking into account when calculating the “no adaption” model (referred to as the “V-mediated adaption”).

7. Reference

- Alber, A.B., Paquet, E.R., Biserni, M., Naef, F., Suter, D.M., 2018. Single Live Cell Monitoring of Protein Turnover Reveals Intercellular Variability and Cell-Cycle Dependence of Degradation Rates. *Mol Cell* 71, 1079-1091.e9. <https://doi.org/10.1016/J.MOLCEL.2018.07.023>
- Alber, A.B., Suter, D.M., 2018. Single-Cell Quantification of Protein Degradation Rates by Time-Lapse Fluorescence Microscopy in Adherent Cell Culture. *Journal of Visualized Experiments*. <https://doi.org/10.3791/56604>
- Amati, B., Alevizopoulos, K., Vlach, J., 1998. MYC AND THE CELL CYCLE, *Frontiers in Bioscience*.
- Babatz, F., Naffin, E., Klämbt, C., 2018. The Drosophila Blood-Brain Barrier Adapts to Cell Growth by Unfolding of Pre-existing Septate Junctions. *Dev Cell* 47, 697-710.e3. <https://doi.org/10.1016/J.DEVCEL.2018.10.002>
- Barry, J.D., Doná, E., Gilmour, D., Huber, W., 2016. TimerQuant: A modelling approach to tandem fluorescent timer design and data interpretation for measuring protein turnover in embryos. *Development (Cambridge)* 143, 174–179. <https://doi.org/10.1242/DEV.125971/256881/AM/TIMERQUANT-A-MODELLING-APPROACH-TO-TANDEM>
- Bertolotti, A., Zhang, Y., Hendershot, L.M., Harding, H.P., Ron, D., 2000. Dynamic interaction of BiP and ER stress transducers in the unfolded-protein response. *Nature Cell Biology* 2:6 2, 326–332. <https://doi.org/10.1038/35014014>
- Bojkowska, K., Santoni De Sio, F., Barde, I., Offner, S., Verp, S., Heinis, C., Johnsson, K., Trono, D., 2011. Measuring In Vivo Protein Half-Life. *Chem Biol* 18, 805–815. <https://doi.org/10.1016/J.CHEMBIOL.2011.03.014>
- Bonifacino, J.S., 2001. Biosynthetic Labeling of Proteins. *Curr Protoc Immunol* 41, 8.12.1-8.12.9. <https://doi.org/10.1002/0471142735.IM0812S41>
- Brown, G.C., 1991. Total cell protein concentration as an evolutionary constraint on the metabolic control distribution in cells. *J Theor Biol* 153, 195–203. [https://doi.org/10.1016/S0022-5193\(05\)80422-9](https://doi.org/10.1016/S0022-5193(05)80422-9)
- Brunner, A.-D., Thielert, M., Vasilopoulou, C., Ammar, C., Coscia, F., Mund, A., Hoerning, O.B., Bache, N., Apalategui, A., Lubeck, M., Richter, S., Fischer, D.S., Raether, O., Park, M.A., Meier, F., Theis, F.J., Mann, M., 2022. Ultra-high sensitivity mass spectrometry quantifies single-cell proteome changes upon perturbation. *Mol Syst Biol* 18, e10798. <https://doi.org/10.15252/MSB.202110798>
- Bukau, B., Weissman, J., Horwich, A., 2006. Molecular Chaperones and Protein Quality Control. *Cell* 125, 443–451. <https://doi.org/10.1016/j.cell.2006.04.014>
- Calabrese, L., Grilli, J., Osella, M., Kempes, C.P., Lagomarsino, M.C., Ciandrini, L., 2022. Protein degradation sets the fraction of active ribosomes at vanishing growth. *PLoS Comput Biol* 18, e1010059. <https://doi.org/10.1371/JOURNAL.PCBI.1010059>
- Calabrese, L., Grilli, J., Osella, M., Kempes, C.P., Lagomarsino, M.C., Ciandrini, L., 2021. Role of protein degradation in growth laws. *bioRxiv* 2021.03.25.436692. <https://doi.org/10.1101/2021.03.25.436692>
- Chen, E.Y., Tan, C.M., Kou, Y., Duan, Q., Wang, Z., Meirelles, G. v., Clark, N.R., Ma'ayan, A., 2013. Enrichr: Interactive and collaborative HTML5 gene list enrichment analysis

- tool. *BMC Bioinformatics* 14, 1–14. <https://doi.org/10.1186/1471-2105-14-128/FIGURES/3>
- Chen, L., Zhu, G., Johns, E.M., Yang, X., 2018. TRIM11 activates the proteasome and promotes overall protein degradation by regulating USP14. *Nature Communications* 2018 9:1 9, 1–14. <https://doi.org/10.1038/s41467-018-03499-z>
- Coligan, J.E., Gates, F.T., Kimball, E.S., Lee Maloy, W., 1983. [37] Radiochemical sequence analysis of biosynthetically labeled proteins. *Methods Enzymol* 91, 413–434. [https://doi.org/10.1016/S0076-6879\(83\)91039-X](https://doi.org/10.1016/S0076-6879(83)91039-X)
- Coux, O., Tanaka, K., Goldberg, A.L., 2003. STRUCTURE AND FUNCTIONS OF THE 20S AND 26S PROTEASOMES. <https://doi.org/10.1146/annurev.bi.65.070196.004101>
- 65, 801–847. <https://doi.org/10.1146/ANNUREV.BI.65.070196.004101>
- Cullinan, S.B., Diehl, J.A., 2004. PERK-dependent Activation of Nrf2 Contributes to Redox Homeostasis and Cell Survival following Endoplasmic Reticulum Stress. *Journal of Biological Chemistry* 279, 20108–20117. <https://doi.org/10.1074/jbc.M314219200>
- Cullinan, S.B., Zhang, D., Hannink, M., Arvisais, E., Kaufman, R.J., Diehl, J.A., 2003. Nrf2 Is a Direct PERK Substrate and Effector of PERK-Dependent Cell Survival. *Mol Cell Biol* 23, 7198. <https://doi.org/10.1128/MCB.23.20.7198-7209.2003>
- Dai, C.-L., Shi, J., Chen, Y., Iqbal, K., Liu, F., Gong, C.-X., 2013. Inhibition of Protein Synthesis Alters Protein Degradation through Activation of Protein Kinase B (AKT) *. <https://doi.org/10.1074/jbc.M112.445148>
- Das, S.K., Lewis, B.A., Levens, D., 2022. MYC: a complex problem. *Trends Cell Biol.* <https://doi.org/10.1016/J.TCB.2022.07.006>
- Dieterich, D.C., Hodas, J.J.L., Gouzer, G., Shadrin, I.Y., Ngo, J.T., Triller, A., Tirrell, D.A., Schuman, E.M., 2010. In situ visualization and dynamics of newly synthesized proteins in rat hippocampal neurons. *Nature Neuroscience* 2010 13:7 13, 897–905. <https://doi.org/10.1038/nn.2580>
- Dieterich, D.C., Link, A.J., Graumann, J., Tirrell, D.A., Schuman, E.M., 2006. Selective identification of newly synthesized proteins in mammalian cells using bioorthogonal noncanonical amino acid tagging (BONCAT). *Proc Natl Acad Sci U S A* 103, 9482–9487. https://doi.org/10.1073/PNAS.0601637103/SUPPL_FILE/01637FIG8.JPG
- Dirick, L., Nasmyth, K., 1991. Positive feedback in the activation of G1 cyclins in yeast. *Nature* 1991 351:6329 351, 754–757. <https://doi.org/10.1038/351754a0>
- Djakovic, S.N., Schwarz, L.A., Barylko, B., DeMartino, G.N., Patrick, G.N., 2009. Regulation of the proteasome by neuronal activity and calcium/calmodulin-dependent protein kinase II. *Journal of Biological Chemistry* 284, 26655–26665. <https://doi.org/10.1074/jbc.M109.021956>
- Doherty, M.K., Hammond, D.E., Clague, M.J., Gaskell, S.J., Beynon, R.J., 2009. Turnover of the human proteome: Determination of protein intracellular stability by dynamic SILAC. *J Proteome Res* 8, 104–112. https://doi.org/10.1021/PR800641V/SUPPL_FILE/PR800641V_SI_001.PDF
- Donà, E., Barry, J.D., Valentin, G., Quirin, C., Khmelinskii, A., Kunze, A., Durdu, S., Newton, L.R., Fernandez-Minan, A., Huber, W., Knop, M., Gilmour, D., 2013. Directional tissue migration through a self-generated chemokine gradient. *Nature* 2013 503:7475 503, 285–289. <https://doi.org/10.1038/nature12635>
- Duncan, R.R., Greaves, J., Wiegand, U.K., Matskevich, I., Bodammer, G., Apps, D.K., Shipston, M.J., Chow, R.H., 2003. Functional and spatial segregation of secretory vesicle pools according to vesicle age. *Nature* 2003 422:6928 422, 176–180. <https://doi.org/10.1038/nature01389>
- Durrieu, L., Kirrmaier, D., Schneidt, T., Kats, I., Raghavan, S., Hufnagel, L., Saunders, T.E., Knop, M., 2018. Bicoid gradient formation mechanism and dynamics revealed by

- protein lifetime analysis. *Mol Syst Biol* 14, e8355.
<https://doi.org/10.15252/MSB.20188355>
- Dvir, S., Velten, L., Sharon, E., Zeevi, D., Carey, L.B., Weinberger, A., Segal, E., 2013. Deciphering the rules by which 5'-UTR sequences affect protein expression in yeast. *Proc Natl Acad Sci U S A* 110, E2792–E2801.
https://doi.org/10.1073/PNAS.1222534110/SUPPL_FILE/SD01.XLSX
- Eden, E., Geva-Zatorsky, N., Issaeva, I., Cohen, A., Dekel, E., Danon, T., Cohen, L., Mayo, A., Alon, U., 2011. Proteome half-life dynamics in living human cells. *Science* (1979) 331, 764–768. <https://doi.org/10.1126/science.1199784>
- Eisenman, R.N., 2001. Deconstructing Myc. *Genes Dev.* <https://doi.org/10.1101/gad928101>
- Elkon, R., Loayza-Puch, F., Korkmaz, G., Lopes, R., van Breugel, P.C., Bleijerveld, O.B., Maarten Altelaar, A.F., Wolf, E., Lorenzin, F., Eilers, M., Agami, R., 2015. Myc coordinates transcription and translation to enhance transformation and suppress invasiveness. *EMBO Rep* 16, 1723–1736. <https://doi.org/10.15252/EMBR.201540717>
- Enam, S.U., Zinshteyn, B., Goldman, D.H., Cassani, M., Livingston, N.M., Seydoux, G., Green, R., 2020. Puromycin reactivity does not accurately localize translation at the subcellular level. *Elife* 9, 1–34. <https://doi.org/10.7554/ELIFE.60303>
- Ershov, D., Phan, M.S., Pylvänäinen, J.W., Rigaud, S.U., le Blanc, L., Charles-Orszag, A., Conway, J.R.W., Laine, R.F., Roy, N.H., Bonazzi, D., Duménil, G., Jacquemet, G., Tinevez, J.Y., 2022. TrackMate 7: integrating state-of-the-art segmentation algorithms into tracking pipelines. *Nature Methods* 2022 19:7 19, 829–832.
<https://doi.org/10.1038/s41592-022-01507-1>
- Flynn, G.C., Pohl, J., Flocco, M.T., Rothman, J.E., 1991. Peptide-binding specificity of the molecular chaperone BiP. *Nature* 353, 726–730. <https://doi.org/10.1038/353726A0>
- Fricke, B., Heink, S., Steffen, J., Kloetzel, P.M., Krüger, E., 2007. The proteasome maturation protein POMP facilitates major steps of 20S proteasome formation at the endoplasmic reticulum. *EMBO Rep* 8, 1170–1175.
<https://doi.org/10.1038/SJ.EMBOR.7401091>
- Fuchs, J., Böhme, S., Oswald, F., Hedde, P.N., Krause, M., Wiedenmann, J., Nienhaus, G.U., 2010. A photoactivatable marker protein for pulse-chase imaging with superresolution. *Nature Methods* 2010 7:8 7, 627–630. <https://doi.org/10.1038/nmeth.1477>
- Geva-Zatorsky, N., Issaeva, I., Mayo, A., Cohen, A., Dekel, E., Danon, T., Cohen, L., Liron, Y., Alon, U., Eden, E., 2012. Using bleach-chase to measure protein half-lives in living cells. *Nature Protocols* 2012 7:4 7, 801–811. <https://doi.org/10.1038/nprot.2012.028>
- Ghenim, L., Allier, C., Obeid, P., Hervé, L., Fortin, J.Y., Balakirev, M., Gidrol, X., 2021. A new ultradian rhythm in mammalian cell dry mass observed by holography. *Scientific Reports* 2021 11:1 11, 1–11. <https://doi.org/10.1038/s41598-020-79661-9>
- Ghoda, L., van Daalen Wetters, T., Macrae, M., Ascherman, D., Coffino, P., 1989. Prevention of Rapid Intracellular Degradation of ODC by a Carboxyl-Terminal Truncation. *Science* (1979) 243, 1493–1495. <https://doi.org/10.1126/SCIENCE.2928784>
- Glick, D., Barth, S., Macleod, K.F., 2010. Autophagy: cellular and molecular mechanisms. *J Pathol* 221, 3–12. <https://doi.org/10.1002/PATH.2697>
- Golan-Lavi, R., Giacomelli, C., Fuks, G., Zeisel, A., Sonntag, J., Sinha, S., Köstler, W., Wiemann, S., Korf, U., Yarden, Y., Domany, E., 2017. Coordinated Pulses of mRNA and of Protein Translation or Degradation Produce EGF-Induced Protein Bursts. *Cell Rep* 18, 3129–3142. <https://doi.org/10.1016/J.CELREP.2017.03.014>
- Gonen, N., Sabath, N., Burge, C.B., Shalgi, R., 2019. Widespread PERK-dependent repression of ER targets in response to ER stress. *Scientific Reports* 2019 9:1 9, 1–12. <https://doi.org/10.1038/s41598-019-38705-5>

- Groll, M., Ditzel, L., Löwe, J., Stock, D., Bochtler, M., Bartunik, H.D., Huber, R., 1997. Structure of 20S proteasome from yeast at 2.4Å resolution. *Nature* 1997 386:6624 386, 463–471. <https://doi.org/10.1038/386463a0>
- Guerra, P., Vuillemenot, L.A., Rae, B., Ladyhina, V., Miliás-Argeitis, A., 2022. Systematic in Vivo Characterization of Fluorescent Protein Maturation in Budding Yeast. *ACS Synth Biol* 11, 1129–1141. https://doi.org/10.1021/ACSSYNBIO.1C00387/SUPPL_FILE/SB1C00387_SI_002.ZIP
- Guo, X., Engel, J.L., Xiao, J., Tagliabracci, V.S., Wang, X., Huang, L., Dixon, J.E., 2011. UBLCP1 is a 26S proteasome phosphatase that regulates nuclear proteasome activity. *Proc Natl Acad Sci U S A* 108, 18649–18654. https://doi.org/10.1073/PNAS.1113170108/SUPPL_FILE/SD01.XLSX
- Guo, X., Wang, X., Wang, Z., Banerjee, S., Yang, J., Huang, L., Dixon, J.E., 2015. Site-specific proteasome phosphorylation controls cell proliferation and tumorigenesis. *Nature Cell Biology* 2016 18:2 18, 202–212. <https://doi.org/10.1038/ncb3289>
- Gurskaya, N.G., Verkhusha, V. v., Shcheglov, A.S., Staroverov, D.B., Chepurnykh, T. v., Fradkov, A.F., Lukyanov, S., Lukyanov, K.A., 2006. Engineering of a monomeric green-to-red photoactivatable fluorescent protein induced by blue light. *Nature Biotechnology* 2006 24:4 24, 461–465. <https://doi.org/10.1038/nbt1191>
- Hetz, C., 2012. The unfolded protein response: Controlling cell fate decisions under ER stress and beyond. *Nat Rev Mol Cell Biol.* <https://doi.org/10.1038/nrm3270>
- Hoyt, M., Zhang, M., enzymology, P.C.-M. in, 2005, undefined, n.d. Probing the ubiquitin/proteasome system with ornithine decarboxylase, a ubiquitin-independent substrate. Elsevier.
- Jackson, R.J., Hellen, C.U.T., Pestova, T. v., 2010. The mechanism of eukaryotic translation initiation and principles of its regulation. *Nature Reviews Molecular Cell Biology* 2010 11:2 11, 113–127. <https://doi.org/10.1038/nrm2838>
- Jones, A.R., Forero-Vargas, M., Withers, S.P., Smith, R.S., Traas, J., Dewitte, W., Murray, J.A.H., 2017. Cell-size dependent progression of the cell cycle creates homeostasis and flexibility of plant cell size. *Nature Communications* 2017 8:1 8, 1–13. <https://doi.org/10.1038/ncomms15060>
- Kafri, M., Metzl-Raz, E., Jonas, F., Barkai, N., 2016. Rethinking cell growth models. *FEMS Yeast Res* 16, 81. <https://doi.org/10.1093/FEMSYR/FOW081>
- Kamber Kaya, H.E., Radhakrishnan, S.K., 2021. Trash Talk: Mammalian Proteasome Regulation at the Transcriptional Level. *Trends in Genetics* 37, 160–173. <https://doi.org/10.1016/J.TIG.2020.09.005>
- Kats, I., Khmelinskii, A., Kschonsak, M., Huber, F., Knieß, R.A., Bartosik, A., Knop, M., 2018. Mapping Degradation Signals and Pathways in a Eukaryotic N-terminome. *Mol Cell* 70, 488-501.e5. <https://doi.org/10.1016/J.MOLCEL.2018.03.033>
- Keppler, A., Gendreizig, S., Gronemeyer, T., Pick, H., Vogel, H., Johnsson, K., 2002. A general method for the covalent labeling of fusion proteins with small molecules in vivo. *Nature Biotechnology* 2002 21:1 21, 86–89. <https://doi.org/10.1038/nbt765>
- Keppler, A., Gendreizig, S., Gronemeyer, T., Pick, H., Vogel, H., Johnsson, K., 2002. A general method for the covalent labeling of fusion proteins with small molecules in vivo. *Nature Biotechnology* 2002 21:1 21, 86–89. <https://doi.org/10.1038/nbt765>
- Keppler, A., Pick, H., Arrivoli, C., Vogel, H., Johnsson, K., 2004. Labeling of fusion proteins with synthetic fluorophores in live cells. *Proc Natl Acad Sci U S A* 101, 9955–9959. https://doi.org/10.1073/PNAS.0401923101/SUPPL_FILE/01923SUPPTXT.HTML
- Khmelinskii, A., Keller, P.J., Bartosik, A., Meurer, M., Barry, J.D., Mardin, B.R., Kaufmann, A., Trautmann, S., Wachsmuth, M., Pereira, G., Huber, W., Schiebel, E., Knop, M.,

2012. Tandem fluorescent protein timers for in vivo analysis of protein dynamics. *Nat Biotechnol* 30, 708–714. <https://doi.org/10.1038/NBT.2281>
- Khmelniskii, A., Meurer, M., Ho, C.T., Besenbeck, B., Füller, J., Lemberg, M.K., Bukau, B., Mogk, A., Knop, M., 2016. Incomplete proteasomal degradation of green fluorescent proteins in the context of tandem fluorescent protein timers. *Mol Biol Cell* 27, 360–370. <https://doi.org/10.1091/MBE.E15-07-0525/ASSET/IMAGES/LARGE/360FIG6.JPEG>
- Kikuchi, J., Iwafune, Y., Akiyama, T., Okayama, A., Nakamura, H., Arakawa, N., Kimura, Y., Hirano, H., 2010. Co- and post-translational modifications of the 26S proteasome in yeast. *Proteomics* 10, 2769–2779. <https://doi.org/10.1002/PMIC.200900283>
- Kim, D., Paggi, J.M., Park, C., Bennett, C., Salzberg, S.L., 2019. Graph-based genome alignment and genotyping with HISAT2 and HISAT-genotype. *Nature Biotechnology* 2019 37:8 37, 907–915. <https://doi.org/10.1038/s41587-019-0201-4>
- Knapp, B.D., Odermatt, P., Rojas, E.R., Cheng, W., He, X., Huang, K.C., Chang, F., 2019. Decoupling of Rates of Protein Synthesis from Cell Expansion Leads to Supergrowth. *Cell Syst* 9, 434-445.e6. <https://doi.org/10.1016/J.CELS.2019.10.001>
- Knop, M., Edgar, B.A., 2014. Tracking protein turnover and degradation by microscopy: photo-switchable versus time-encoded fluorescent proteins. *Open Biol* 4. <https://doi.org/10.1098/RSOB.140002>
- Kohanim, Y.K., Levi, D., Jona, G., Towbin, B.D., Bren, A., Correspondence, U.A., Alon, U., 2018. A Bacterial Growth Law out of Steady State. *CellReports* 23, 2891–2900. <https://doi.org/10.1016/j.celrep.2018.05.007>
- Kopp, M.C., Larburu, N., Durairaj, V., Adams, C.J., Ali, M.M.U., 2019. UPR proteins IRE1 and PERK switch BiP from chaperone to ER stress sensor. *Nature Structural & Molecular Biology* 2019 26:11 26, 1053–1062. <https://doi.org/10.1038/s41594-019-0324-9>
- Kors, S., 2019. Regulation of Proteasome Activity by (Post-)transcriptional Mechanisms. *Front Mol Biosci* 6, 48. <https://doi.org/10.3389/FMOLB.2019.00048/XML/NLM>
- Kristensen, A.R., Gsponer, J., Foster, L.J., 2013. Protein synthesis rate is the predominant regulator of protein expression during differentiation. *Mol Syst Biol* 9, 689. <https://doi.org/10.1038/MSB.2013.47>
- Kuleshov, M. v., Jones, M.R., Rouillard, A.D., Fernandez, N.F., Duan, Q., Wang, Z., Koplev, S., Jenkins, S.L., Jagodnik, K.M., Lachmann, A., McDermott, M.G., Monteiro, C.D., Gundersen, G.W., Maayan, A., 2016. Enrichr: a comprehensive gene set enrichment analysis web server 2016 update. *Nucleic Acids Res* 44, W90–W97. <https://doi.org/10.1093/NAR/GKW377>
- Lacerda, R., Menezes, J., Romão, L., 2016. More than just scanning: the importance of cap-independent mRNA translation initiation for cellular stress response and cancer. *Cellular and Molecular Life Sciences* 2016 74:9 74, 1659–1680. <https://doi.org/10.1007/S00018-016-2428-2>
- Lacsina, J.R., Marks, O.A., Liu, X., Reid, D.W., Jagannathan, S., Nicchitta, C. v., 2012. Premature Translational Termination Products Are Rapidly Degraded Substrates for MHC Class I Presentation. *PLoS One* 7, 51968. <https://doi.org/10.1371/JOURNAL.PONE.0051968>
- Lee, D., Goldberg, A.L., 2022. 26S proteasomes become stably activated upon heat shock when ubiquitination and protein degradation increase. *Proc Natl Acad Sci U S A* 119. <https://doi.org/10.1073/PNAS.2122482119/-/DCSUPPLEMENTAL>
- Lee, S.H., Park, Y., Yoon, S.K., Yoon, J.B., 2010. Osmotic stress inhibits proteasome by p38 MAPK-dependent phosphorylation. *J Biol Chem* 285, 41280–41289. <https://doi.org/10.1074/JBC.M110.182188>

- Leestemaker, Y., de Jong, A., Witting, K.F., Scheper, W., Berkers, C.R., Ovaas, H., Penning, R., Schuurman, K., Rodenko, B., Zaal, E.A., van de Kooij, B., Laufer, S., Heck, A.J.R., Borst, J., 2017. Proteasome Activation by Small Molecules Article Proteasome Activation by Small Molecules. *Cell Chem Biol* 24, 725–736. <https://doi.org/10.1016/j.chembiol.2017.05.010>
- Leppek, K., Das, R., Barna, M., 2017. Functional 5' UTR mRNA structures in eukaryotic translation regulation and how to find them. *Nature Reviews Molecular Cell Biology* 2017 19:3 19, 158–174. <https://doi.org/10.1038/nrm.2017.103>
- Lew, D.J., Dulić, V., Reed, S.I., 1991. Isolation of three novel human cyclins by rescue of G1 cyclin (cln) function in yeast. *Cell* 66, 1197–1206. [https://doi.org/10.1016/0092-8674\(91\)90042-W](https://doi.org/10.1016/0092-8674(91)90042-W)
- Li, W., Bengtson, M.H., Ulbrich, A., Matsuda, A., Reddy, V.A., Orth, A., Chanda, S.K., Batalov, S., Joazeiro, C.A.P., 2008. Genome-Wide and Functional Annotation of Human E3 Ubiquitin Ligases Identifies MULAN, a Mitochondrial E3 that Regulates the Organelle's Dynamics and Signaling. *PLoS One* 3, e1487. <https://doi.org/10.1371/JOURNAL.PONE.0001487>
- Li, X., Zhao, X., Fang, Y., Jiang, X., Duong, T., Fan, C., Huang, C.C., Kain, S.R., 1998. Generation of Destabilized Green Fluorescent Protein as a Transcription Reporter. *Journal of Biological Chemistry* 273, 34970–34975. <https://doi.org/10.1074/JBC.273.52.34970>
- Liao, Y., Smyth, G.K., Shi, W., 2014. featureCounts: an efficient general purpose program for assigning sequence reads to genomic features. *Bioinformatics* 30, 923–930. <https://doi.org/10.1093/BIOINFORMATICS/BTT656>
- Lin, C.Y., Lovén, J., Rahl, P.B., Paranal, R.M., Burge, C.B., Bradner, J.E., Lee, T.I., Young, R.A., 2012. Transcriptional Amplification in Tumor Cells with Elevated c-Myc. *Cell* 151, 56–67. <https://doi.org/10.1016/J.CELL.2012.08.026>
- Liu, G., Rogers, J., Murphy, C.T., Rongo, C., 2011. EGF signalling activates the ubiquitin proteasome system to modulate *C. elegans* lifespan. *EMBO J* 30, 2990–3003. <https://doi.org/10.1038/EMBOJ.2011.195>
- Liu, J., Xu, Y., Stoleru, D., Salic, A., 2012. Imaging protein synthesis in cells and tissues with an alkyne analog of puromycin. *Proc Natl Acad Sci U S A* 109, 413–418. https://doi.org/10.1073/PNAS.1111561108/SUPPL_FILE/PNAS.1111561108_SI.PDF
- Liu, S., Tan, C., Melo-Gavin, C., Mark, K.G., Ginzberg, M.B., Blutrach, R., Patel, N., Rape, M., Kafri, R., Affiliations, #, 2021. Large cells activate global protein degradation to maintain cell size homeostasis. *bioRxiv* 2021.11.09.467936. <https://doi.org/10.1101/2021.11.09.467936>
- Lokireddy, S., Kukushkin, N.V., Goldberg, A.L., 2015. cAMP-induced phosphorylation of 26S proteasomes on Rpn6/PSMD11 enhances their activity and the degradation of misfolded proteins. *Proc Natl Acad Sci U S A* 112, E7176–E7185. https://doi.org/10.1073/PNAS.1522332112/SUPPL_FILE/PNAS.1522332112.SD01.XL SX
- Lokireddy, S., Kukushkin, N.V., Goldberg, A.L., 2015. cAMP-induced phosphorylation of 26S proteasomes on Rpn6/PSMD11 enhances their activity and the degradation of misfolded proteins. *Proc Natl Acad Sci U S A* 112, E7176–E7185. <https://doi.org/10.1073/PNAS.1522332112/-/DCSUPPLEMENTAL>
- Lourenco, C., Resetca, D., Redel, C., Lin, P., MacDonald, A.S., Ciaccio, R., Kenney, T.M.G., Wei, Y., Andrews, D.W., Sunnerhagen, M., Arrowsmith, C.H., Raught, B., Penn, L.Z., 2021. MYC protein interactors in gene transcription and cancer. *Nature Reviews Cancer* 2021 21:9 21, 579–591. <https://doi.org/10.1038/s41568-021-00367-9>

- Love, M.I., Huber, W., Anders, S., 2014. Moderated estimation of fold change and dispersion for RNA-seq data with DESeq2. *Genome Biol* 15, 1–21. <https://doi.org/10.1186/S13059-014-0550-8/FIGURES/9>
- Löwe, J., Stock, D., Jap, B., Zwickl, P., Baumeister, W., Huber, R., 1995. Crystal Structure of the 20S Proteasome from the Archaeon *T. acidophilum* at 3.4 Å Resolution. *Science* (1979) 268, 533–539. <https://doi.org/10.1126/SCIENCE.7725097>
- Luo, W., Brouwer, C., 2013. Pathview: an R/Bioconductor package for pathway-based data integration and visualization. *Bioinformatics* 29, 1830–1831. <https://doi.org/10.1093/BIOINFORMATICS/BTT285>
- Luo, W., Pant, G., Bhavnasi, Y.K., Blanchard, S.G., Brouwer, C., 2017. Pathview Web: user friendly pathway visualization and data integration. *Nucleic Acids Res* 45, W501–W508. <https://doi.org/10.1093/NAR/GKX372>
- Mark, C., Metzner, C., Lautscham, L., Strissel, P.L., Strick, R., Fabry, B., 2018. Bayesian model selection for complex dynamic systems. *Nature Communications* 2018 9:1 9, 1–12. <https://doi.org/10.1038/s41467-018-04241-5>
- Medrano, E.E., Pardee, A.B., 1980. Prevalent deficiency in tumor cells of cycloheximide-induced cycle arrest. *Proc Natl Acad Sci U S A* 77, 4123–4126. <https://doi.org/10.1073/PNAS.77.7.4123>
- Meisenhelder, J., Hunter, T., 1988. Radioactive protein-labelling techniques. *Nature* 1988 335:6186 335, 120–120. <https://doi.org/10.1038/335120a0>
- Mellblom, L., Enerbäck, L., 1979. Protein content, dry mass and chemical composition of individual mast cells related to body growth. *Histochemistry* 1979 63:2 63, 129–143. <https://doi.org/10.1007/BF00644535>
- Metzl-Raz, E., Kafri, M., Yaakov, G., Soifer, I., Gurvich, Y., Barkai, N., 2017. Principles of cellular resource allocation revealed by condition-dependent proteome profiling. *Elife* 6. <https://doi.org/10.7554/ELIFE.28034>
- Metzner, C., Mark, C., Steinwachs, J., Lautscham, L., Stadler, F., Fabry, B., 2015. Superstatistical analysis and modelling of heterogeneous random walks. *Nature Communications* 2015 6:1 6, 1–8. <https://doi.org/10.1038/ncomms8516>
- Miettinen, T.P., Ly, K.S., Lam, A., Manalis, S.R., 2022. Single-cell monitoring of dry mass and dry mass density reveals exocytosis of cellular dry contents in mitosis. *Elife* 11. <https://doi.org/10.7554/ELIFE.76664>
- Milo, R., 2013. What is the total number of protein molecules per cell volume? A call to rethink some published values. *Bioessays* 35, 1050. <https://doi.org/10.1002/BIES.201300066>
- Mirabella, R., Franken, C., van der Krogt, G.N.M., Bisseling, T., Geurts, R., 2004. Use of the Fluorescent Timer DsRED-E5 as Reporter to Monitor Dynamics of Gene Activity in Plants. *Plant Physiol* 135, 1879–1887. <https://doi.org/10.1104/PP.103.038539>
- Moro, S.G., Hermans, C., Ruiz-Orera, J., Albà, M.M., 2021. Impact of uORFs in mediating regulation of translation in stress conditions. *BMC Mol Cell Biol* 22, 1–13. <https://doi.org/10.1186/S12860-021-00363-9/FIGURES/4>
- Mulas, C., Kalkan, T., von Meyenn, F., Leitch, H.G., Nichols, J., Smith, A., 2019. Defined conditions for propagation and manipulation of mouse embryonic stem cells. *Development* 146. <https://doi.org/10.1242/DEV.173146>
- Munkres, J., 1957. Algorithms for the Assignment and Transportation Problems. *Journal of the Society for Industrial and Applied Mathematics* 5, 32–38. <https://doi.org/10.1137/0105003>
- Murata, S., Yashiroda, H., Tanaka, K., 2009. Molecular mechanisms of proteasome assembly. *Nature Reviews Molecular Cell Biology* 2009 10:2 10, 104–115. <https://doi.org/10.1038/nrm2630>

- Neurohr, G.E., Terry, R.L., Lengefeld, J., Bonney, M., Brittingham, G.P., Moretto, F., Miettinen, T.P., Vaites, L.P., Soares, L.M., Paulo, J.A., Harper, J.W., Buratowski, S., Manalis, S., van Werven, F.J., Holt, L.J., Amon, A., 2019. Excessive Cell Growth Causes Cytoplasm Dilution And Contributes to Senescence. *Cell* 176, 1083-1097.e18. <https://doi.org/10.1016/J.CELL.2019.01.018>
- Nie, Z., Guo, C., Das, S.K., Chow, C.C., Batchelor, E., Simons Jnr, S.S., Levens, D., 2020. Dissecting transcriptional amplification by MYC. *Elife* 9, 1–32. <https://doi.org/10.7554/ELIFE.52483>
- Nie, Z., Guo, C., Das, S.K., Chow, C.C., Batchelor, E., Simons Jnr, S.S., Levens, D., 2020. Dissecting transcriptional amplification by MYC. *Elife* 9, 1–32. <https://doi.org/10.7554/ELIFE.52483>
- Nie, Z., Hu, G., Wei, G., Cui, K., Yamane, A., Resch, W., Wang, R., Green, D.R., Tessarollo, L., Casellas, R., Zhao, K., Levens, D., 2012. c-Myc Is a Universal Amplifier of Expressed Genes in Lymphocytes and Embryonic Stem Cells. *Cell* 151, 68–79. <https://doi.org/10.1016/j.cell.2012.08.033>
- Ong, S.E., Blagoev, B., Kratchmarova, I., Kristensen, D.B., Steen, H., Pandey, A., Mann, M., 2002. Stable isotope labeling by amino acids in cell culture, SILAC, as a simple and accurate approach to expression proteomics. *Mol Cell Proteomics* 1, 376–386. <https://doi.org/10.1074/mcp.M200025-MCP200>
- Org/Qrb, C., Review, M., Kepp, K.P., 2020. Survival of the cheapest: how proteome cost minimization drives evolution. *Q Rev Biophys* 53. <https://doi.org/10.1017/S0033583520000037>
- Patange, S., Ball, D.A., Wan, Y., Karpova, T.S., Girvan, M., Levens, D., Larson Correspondence, D.R., Larson, D.R., 2022. MYC amplifies gene expression through global changes in transcription factor dynamics In brief MYC amplifies gene expression through global changes in transcription factor dynamics. *CellReports* 38, 110292. <https://doi.org/10.1016/j.celrep.2021.110292>
- Pathare, G.R., Nagy, I., Bohn, S., Unverdorben, P., Hubert, A., Körner, R., Nickell, S., Lasker, K., Sali, A., Tamura, T., Nishioka, T., Förster, F., Baumeister, W., Bracher, A., 2012. The proteasomal subunit Rpn6 is a molecular clamp holding the core and regulatory subcomplexes together. *Proc Natl Acad Sci U S A* 109, 149–154. https://doi.org/10.1073/PNAS.1117648108/SUPPL_FILE/PNAS.1117648108_SI.PDF
- Pédelacq, J.-D., Cabantous, S., Tran, T., Terwilliger, T.C., Waldo, G.S., 2006. Engineering and characterization of a superfolder green fluorescent protein. <https://doi.org/10.1038/nbt1172>
- Pickering, A.M., Davies, K.J.A., 2012. Differential roles of proteasome and immunoproteasome regulators Pa28 $\alpha\beta$, Pa28 γ and Pa200 in the degradation of oxidized proteins. *Arch Biochem Biophys* 523, 181–190. <https://doi.org/10.1016/J.ABB.2012.04.018>
- Pincus, D., Chevalier, M.W., Aragón, T., van Anken, E., Vidal, S.E., El-Samad, H., Walter, P., 2010. BiP Binding to the ER-Stress Sensor Ire1 Tunes the Homeostatic Behavior of the Unfolded Protein Response. *PLoS Biol* 8, e1000415. <https://doi.org/10.1371/JOURNAL.PBIO.1000415>
- Polymenis, M., Schmidt, E. v., 1997. Coupling of cell division to cell growth by translational control of the G1 cyclin CLN3 in yeast. *Genes Dev* 11, 2522–2531. <https://doi.org/10.1101/GAD.11.19.2522>
- Pratt, J.M., Petty, J., Riba-Garcia, I., Robertson, D.H.L., Gaskell, S.J., Oliver, S.G., Beynon, R.J., 2002. Dynamics of protein turnover, a missing dimension in proteomics. *Mol Cell Proteomics* 1, 579–591. <https://doi.org/10.1074/mcp.M200046-MCP200>

- Rackauckas, C., Nie, Q., 2017. DifferentialEquations.jl – A Performant and Feature-Rich Ecosystem for Solving Differential Equations in Julia. *J Open Res Softw* 5, 15. <https://doi.org/10.5334/JORS.151>
- Radhakrishnan, S.K., Lee, C.S., Young, P., Beskow, A., Chan, J.Y., Deshaies, R.J., 2010. Transcription Factor Nrf1 Mediates the Proteasome Recovery Pathway after Proteasome Inhibition in Mammalian Cells. *Mol Cell* 38, 17–28. <https://doi.org/10.1016/J.MOLCEL.2010.02.029>
- Ranek, M.J., Kost, C.K., Hu, C., Martin, D.S., Wang, X., 2014. Muscarinic 2 receptors modulate cardiac proteasome function in a protein kinase G-dependent manner. *J Mol Cell Cardiol* 69, 43–51. <https://doi.org/10.1016/J.YJMCC.2014.01.017>
- Rock, K.L., Gramm, C., Rothstein, L., Clark, K., Stein, R., Dick, L., Hwang, D., Goldberg, A.L., 1994. Inhibitors of the proteasome block the degradation of most cell proteins and the generation of peptides presented on MHC class I molecules. *Cell* 78, 761–771. [https://doi.org/10.1016/S0092-8674\(94\)90462-6](https://doi.org/10.1016/S0092-8674(94)90462-6)
- Rock, K.L., Gramm, C., Rothstein, L., Clark, K., Stein, R., Dick, L., Hwang, D., Goldberg, A.L., 1994. Inhibitors of the proteasome block the degradation of most cell proteins and the generation of peptides presented on MHC class I molecules. *Cell* 78, 761–771. [https://doi.org/10.1016/S0092-8674\(94\)90462-6](https://doi.org/10.1016/S0092-8674(94)90462-6)
- Rolfe, D.F.S., Brown, G.C., 1997. Cellular energy utilization and molecular origin of standard metabolic rate in mammals. *Physiol Rev* 77, 731–758. <https://doi.org/10.1152/PHYSREV.1997.77.3.731>
- Rolfs, Z., Frey, B.L., Shi, X., Kawai, Y., Smith, L.M., Welham, N. v., 2021. An atlas of protein turnover rates in mouse tissues. *Nature Communications* 2021 12:1 12, 1–9. <https://doi.org/10.1038/s41467-021-26842-3>
- Rothman, S., 2010. How is the balance between protein synthesis and degradation achieved? *Theor Biol Med Model* 7, 25. <https://doi.org/10.1186/1742-4682-7-25>
- Sakellari, M., Chondrogianni, N., Gonos, E.S., 2019. Protein synthesis inhibition induces proteasome assembly and function. *Biochem Biophys Res Commun* 514, 224–230. <https://doi.org/10.1016/J.BBRC.2019.04.114>
- Savitzky, A., Golay, M.J.E., 1964. Smoothing and Differentiation of Data by Simplified Least Squares Procedures. *Anal Chem* 36, 1627–1639. https://doi.org/10.1021/AC60214A047/ASSET/AC60214A047.FP.PNG_V03
- Schmidt, R.M., Schessner, J.P., Borner, G.H.H., Schuck, S., 2019. The proteasome biogenesis regulator Rpn4 cooperates with the unfolded protein response to promote ER stress resistance. *Elife* 8. <https://doi.org/10.7554/ELIFE.43244>
- Schmidt, U., Weigert, M., Broaddus, C., Myers, G., 2018. Cell detection with star-convex polygons. *Lecture Notes in Computer Science (including subseries Lecture Notes in Artificial Intelligence and Lecture Notes in Bioinformatics)* 11071 LNCS, 265–273. https://doi.org/10.1007/978-3-030-00934-2_30/TABLES/1
- Scognamiglio, R., Cabezas-Wallscheid, N., Thier, M.C., Altamura, S., Reyes, A., Prendergast, Á.M., Baumgärtner, D., Carnevalli, L.S., Atzberger, A., Haas, S., von Paleske, L., Boroviak, T., Wörsdörfer, P., Essers, M.A.G., Kloz, U., Eisenman, R.N., Edenhofer, F., Bertone, P., Huber, W., van der Hoeven, F., Smith, A., Trumpp, A., 2016. Myc Depletion Induces a Pluripotent Dormant State Mimicking Diapause. *Cell* 164, 668–680. <https://doi.org/10.1016/j.cell.2015.12.033>
- Scott, M., Gunderson, C.W., Mateescu, E.M., Zhang, Z., Hwa, T., 2010. Interdependence of cell growth and gene expression: Origins and consequences. *Science* (1979) 330, 1099–1102. https://doi.org/10.1126/SCIENCE.1192588/SUPPL_FILE/SCOTT.SOM.PDF
- Scott, M., Hwa, T., 2011. Bacterial growth laws and their applications. *Curr Opin Biotechnol* 22, 559–565. <https://doi.org/10.1016/J.COPBIO.2011.04.014>

- Sha, Z., Goldberg, A.L., 2014. Proteasome-mediated processing of Nrf1 is essential for coordinate induction of all proteasome subunits and p97. *Current Biology* 24, 1573–1583. <https://doi.org/10.1016/j.cub.2014.06.004>
- Shah, P., Ding, Y., Niemczyk, M., Kudla, G., Plotkin, J.B., 2013. Rate-Limiting Steps in Yeast Protein Translation. *Cell* 153, 1589–1601. <https://doi.org/10.1016/J.CELL.2013.05.049>
- Shatsky, I.N., Terenin, I.M., Smirnova, V. v., Andreev, D.E., 2018. Cap-Independent Translation: What's in a Name? *Trends Biochem Sci* 43, 882–895. <https://doi.org/10.1016/J.TIBS.2018.04.011>
- Steffen, J., Seeger, M., Koch, A., Krüger, E., 2010. Proteasomal Degradation Is Transcriptionally Controlled by TCF11 via an ERAD-Dependent Feedback Loop. *Mol Cell* 40, 147–158. <https://doi.org/10.1016/J.MOLCEL.2010.09.012>
- Stringer, C., Michaelos, M., Pachitariu, M., 2020. Cellpose: a generalist algorithm for cellular segmentation. *bioRxiv* 2020.02.02.931238. <https://doi.org/10.1101/2020.02.02.931238>
- Subach, F. v., Subach, O.M., Gundorov, I.S., Morozova, K.S., Piatkevich, K.D., Cuervo, A.M., Verkhusha, V. v., 2009. Monomeric fluorescent timers that change color from blue to red report on cellular trafficking. *Nature Chemical Biology* 2009 5:2 5, 118–126. <https://doi.org/10.1038/nchembio.138>
- Subramanian, A., Tamayo, P., Mootha, V.K., Mukherjee, S., Ebert, B.L., Gillette, M.A., Paulovich, A., Pomeroy, S.L., Golub, T.R., Lander, E.S., Mesirov, J.P., 2005. Gene set enrichment analysis: A knowledge-based approach for interpreting genome-wide expression profiles. *Proc Natl Acad Sci U S A* 102, 15545–15550. https://doi.org/10.1073/PNAS.0506580102/SUPPL_FILE/06580FIG7.JPG
- Sun, S., Liu, S., Zhang, Z., Zeng, W., Sun, T., Tao, T., Lin, X., Feng, X.H., 2017. Phosphatase UBLCP1 controls proteasome assembly. *Open Biol* 7. <https://doi.org/10.1098/RSOB.170042>
- Swovick, K., Firsanov, D., Welle, K.A., Hryhorenko, J.R., Wise, J.P., George, C., Sformo, T.L., Seluanov, A., Gorbunova, V., Ghaemmaghami, S., 2021. Interspecies Differences in Proteome Turnover Kinetics Are Correlated With Life Spans and Energetic Demands. *Molecular & Cellular Proteomics* 20, 100041. <https://doi.org/10.1074/MCP.RA120.002301>
- Takeuchi, J., Chen, H., Hoyt, M.A., Coffino, P., 2008. Structural elements of the ubiquitin-independent proteasome degron of ornithine decarboxylase. *Biochemical Journal* 410, 401–407. <https://doi.org/10.1042/BJ20071239>
- Terenin, I.M., Smirnova, V. v., Andreev, D.E., Dmitriev, S.E., Shatsky, I.N., 2016. A researcher's guide to the galaxy of IRESSs. *Cellular and Molecular Life Sciences* 2016 74:8 74, 1431–1455. <https://doi.org/10.1007/S00018-016-2409-5>
- Tornøe, C.W., Christensen, C., Meldal, M., 2002. Peptidotriazoles on solid phase: [1,2,3]-Triazoles by regioselective copper(I)-catalyzed 1,3-dipolar cycloadditions of terminal alkynes to azides. *Journal of Organic Chemistry* 67, 3057–3064. https://doi.org/10.1021/JO011148J/SUPPL_FILE/JO011148J_S.PDF
- Tsuboi, T., Kitaguchi, T., Karasawa, S., Fukuda, M., Miyawaki, A., 2010. Age-dependent preferential dense-core vesicle exocytosis in neuroendocrine cells revealed by newly developed monomeric fluorescent timer protein. *Mol Biol Cell* 21, 87–94. <https://doi.org/10.1091/MBC.E09-08-0722/ASSET/IMAGES/LARGE/ZMK0011093140006.JPEG>
- Tyers, M., Tokiwa, G., Nash, R., Fitcher, B., 1992. The Cln3-Cdc28 kinase complex of *S. cerevisiae* is regulated by proteolysis and phosphorylation. *EMBO J* 11, 1773–1784. <https://doi.org/10.1002/J.1460-2075.1992.TB05229.X>

- VerPlank, J.J.S., Goldberg, A.L., 2017. Regulating protein breakdown through proteasome phosphorylation. *Biochemical Journal* 474, 3355–3371. <https://doi.org/10.1042/BCJ20160809>
- VerPlank, J.J.S., Tyrkalska, S.D., Fleming, A., Rubinsztein, D.C., Goldberg, A.L., 2020. cGMP via PKG activates 26S proteasomes and enhances degradation of proteins, including ones that cause neurodegenerative diseases. *Proceedings of the National Academy of Sciences* 117, 14220–14230. <https://doi.org/10.1073/PNAS.2003277117>
- Wang, H., Carey, L.B., Cai, Y., Wijnen, H., Futcher, B., 2009. Recruitment of Cln3 Cyclin to Promoters Controls Cell Cycle Entry via Histone Deacetylase and Other Targets. *PLoS Biol* 7, e1000189. <https://doi.org/10.1371/JOURNAL.PBIO.1000189>
- Waterlow, J., Garlick, P., Millward, D., 1978. Protein turnover in mammalian tissues and in the whole body.
- Welle, K.A., Zhang, T., Hryhorenko, J.R., Shen, S., Qu, J., Ghaemmaghmi, S., 2016. Time-resolved analysis of proteome dynamics by tandem mass tags and stable isotope labeling in cell culture (TMT-SILAC) Hyperplexing. *Molecular and Cellular Proteomics* 15, 3551–3563. <https://doi.org/10.1074/mcp.M116.063230>
- Wheatley, D.N., 1984. Intracellular protein degradation: Basis of a self-regulating mechanism for the proteolysis of endogenous proteins. *J Theor Biol* 107, 127–149. [https://doi.org/10.1016/S0022-5193\(84\)80125-3](https://doi.org/10.1016/S0022-5193(84)80125-3)
- Wu, B., Piatkevich, K.D., Lionnet, T., Singer, R.H., Verkhusha, V. v., 2011. Modern fluorescent proteins and imaging technologies to study gene expression, nuclear localization, and dynamics. *Curr Opin Cell Biol* 23, 310–317. <https://doi.org/10.1016/J.CEB.2010.12.004>
- Xie, Z., Bailey, A., Kuleshov, M. v., Clarke, D.J.B., Evangelista, J.E., Jenkins, S.L., Lachmann, A., Wojciechowicz, M.L., Kropiwnicki, E., Jagodnik, K.M., Jeon, M., Ma'ayan, A., 2021. Gene Set Knowledge Discovery with Enrichr. *Curr Protoc* 1, e90. <https://doi.org/10.1002/CPZ1.90>
- Yazgili, A.S., Meul, T., Welk, V., Semren, N., Kammerl, I.E., Meiners, S., 2021. In-gel proteasome assay to determine the activity, amount, and composition of proteasome complexes from mammalian cells or tissues. *STAR Protoc* 2. <https://doi.org/10.1016/J.XPRO.2021.100526>
- Yin, X., Giap, C., Lazo, J.S., Prochownik, E. v., 2003. Low molecular weight inhibitors of Myc–Max interaction and function. *Oncogene* 22:40, 6151–6159. <https://doi.org/10.1038/sj.onc.1206641>
- Zhang, F., Hu, Y., Huang, P., Toleman, C.A., Paterson, A.J., Kudlow, J.E., 2007. Proteasome function is regulated by cyclic AMP-dependent protein kinase through phosphorylation of Rpt6. *Journal of Biological Chemistry* 282, 22460–22471. <https://doi.org/10.1074/jbc.M702439200>
- Zhang, L., Gurskaya, N.G., Merzlyak, E.M., Staroverov, D.B., Mudrik, N.N., Samarkina, O.N., Vinokurov, L.M., Lukyanov, S., Lukyanov, K.A., 2007. Method for real-time monitoring of protein degradation at the single cell level. *Biotechniques* 42, 446–450. <https://doi.org/10.2144/000112453/ASSET/IMAGES/LARGE/FIGURE2.JPEG>
- Zhang, M., Pickart, C.M., Coffino, P., 2003. Determinants of proteasome recognition of ornithine decarboxylase, a ubiquitin-independent substrate. *EMBO J* 22, 1488–1496. <https://doi.org/10.1093/EMBOJ/CDG158>
- Zhang, T., Shen, S., Qu, J., Ghaemmaghmi, S., 2016. Global Analysis of Cellular Protein Flux Quantifies the Selectivity of Basal Autophagy. *Cell Rep* 14, 2426–2439. <https://doi.org/10.1016/J.CELREP.2016.02.040/ATTACHMENT/75499DC9-4F35-4904-8262-C7295D8AFCBC/MMC6.XLSX>

- Zhang, T., Wolfe, C., Pierle, A., Welle, K.A., Hryhorenko, J.R., Ghaemmaghami, S., 2017. Proteome-wide modulation of degradation dynamics in response to growth arrest. *Proceedings of the National Academy of Sciences* 114, E10329–E10338. <https://doi.org/10.1073/PNAS.1710238114>
- Zhao, J., Zhai, B., Gygi, S.P., Goldberg, A.L., 2015. MTOR inhibition activates overall protein degradation by the ubiquitin proteasome system as well as by autophagy. *Proc Natl Acad Sci U S A* 112, 15790–15797. https://doi.org/10.1073/PNAS.1521919112/SUPPL_FILE/PNAS.1521919112.SAPP.PDF
- Zielke, N., Kim, K.J., Tran, V., Shibutani, S.T., Bravo, M.J., Nagarajan, S., van Straaten, M., Woods, B., von Dassow, G., Rottig, C., Lehner, C.F., Grewal, S.S., Duronio, R.J., Edgar, B.A., 2011. Control of *Drosophila* endocycles by E2F and CRL4CDT2. *Nature* 2011 480:7375 480, 123–127. <https://doi.org/10.1038/nature10579>

8. Curriculum vitae

MICHAEL SHOUJIE SUN 孙绶杰

(First name) (Family name)

Email: michael.sunjk@gmail.com

Phone: +41 (0)766835221

Address: rue Louis-Auguste Curtat 25, 1005, Lausanne

Education

Doctoral Program in Molecular Life Sciences

EPFL

School of life sciences, EPFL

Nov. 2018 – Dec. 2022

Master Program Molecular and Cellular Biology

Universität Zürich

Institute of Molecular Life Science

Sep. 2016 - Aug. 2018

Bachelor of Biological Engineering

Tianjin University

School of Chemical Engineering and Technology

Sep. 2012 - Jun. 2016

Research Experience

PhD thesis in Prof. David Suter's lab (UPSUTER)

Institute of Bioengineering, EPFL

Nov. 2018 – Dec. 2022

Research assistant in Prof. Christian Lehner's lab

Institute of Molecular Life Science, Universität Zürich

Jun. 2018 – Nov. 2018

Master thesis in Prof. Christian Lehner's lab

Institute of Molecular Life Science, Universität Zürich

Nov. 2016 – Jun. 2017

Bachelor thesis in Prof. Hao Qi's Lab

Key Laboratory of System Bioengineering of the Ministry of Education, Tianjin University

Dec. 2014 – Jun. 2016

Professional Skills

Biological laboratory: molecular biology (PCR, cloning, DNA/RNA/protein extraction and purification, etc); mammalian cell culture; creating transgenic mammalian cells; fruit fly husbandry; creating transgenic fruit flies; microscopy (wild-field, laser-scanning confocal, and spinning disc *in vivo* imaging); immunofluorescence; FISH; Western blot; biochemistry assays.

Computational: Advanced imaging processing (Stardist, Cellpose, Trackmate, Scikit-image, ImageJ, Cellprofiler); Python (Pandas, SciPy, Scikit-learn, etc.); RNA-seq analysis; Galaxy; R (basic).

Publications

Sun, M. S., Weber, J., Blattner, A. C., Chaurasia, S., & Lehner, C. F. (2019). MNM and SNM maintain but do not establish achiasmate homolog conjunction during *Drosophila* male meiosis. *PLoS genetics*, 15(5), e1008162.

Kabakci, Z., Yamada, H., Vernizzi, L., Gupta, S., Weber, J., **Sun, M. S.**, & Lehner, C. F. (2022). Teflon promotes chromosomal recruitment of homolog conjunction proteins during *Drosophila* male meiosis. *PLoS Genetics*, 18(10), e1010469.

Competitions

iGEM competition 2013, Gold Medal (With awards of the Second Runner Up in Asia, the Final List of Asia, and the Best Poster)

iGEM competition 2014, Bronze Medal

iGEM is a competition for undergraduate students in the field of synthetic biology. Each the team works on a project containing wet lab experiments, modelling, and social outreach, which lasts a semester, and showcases the achievements at an event in Boston, the United States.

Personal Skills

Chinese: Mother tongue **English:** C1-C2 **French:** A2 **German:** A1 (Basic)

Other skills: Drawing (sketching, watercolour); pottery; Illustrator; Photoshop